OBSERVATIONAL AND NUMERICAL MODELING STUDIES OF TURBULENCE ON THE TEXAS-LOUISIANA CONTINENTAL SHELF

A Dissertation

by

ZHENG ZHANG

Submitted to the Office of Graduate Studies of
Texas A&M University
in partial fulfillment of the requirements for the degree of

DOCTOR OF PHILOSOPHY

Chair of Committee,	Ayal Anis
Co-Chair of Committee,	Dongliang Zhao
Committee Members,	Douglas J. Klein
	Achim Stöessel
Head of Department,	Piers Chapman

August 2013

Major Subject: Oceanography

ABSTRACT

Turbulent dynamics at two sites (C and D) in a hypoxic zone on the Texas-Louisiana continental shelf were studied by investigating turbulence quantities i.e. turbulence kinetic energy (TKE), dissipation rate of TKE (ϵ), Reynolds stress (τ), dissipation rate of temperature variance (χ), eddy diffusivity of temperature (ν_t'), and eddy diffusivity of density (ν_ρ'). Numerical models were also applied to test their capability of simulating these turbulence quantities.

At site D, TKE, ϵ, and τ were calculated from velocity measurements in the bottom boundary layer (BBL), using the Kolmogorov's -5/3 law in the inertial subrange of energy spectra of vertical velocity fluctuations in each burst measurement. Four second-moment turbulence closure models were applied for turbulence simulations, and modeled turbulence quantities were found to be consistent with those observed. It was found from inter-model comparisons that models with the stability functions of Schumann and Gerz predicted higher values of turbulence quantities than those of Cheng in the mid layer, which might be due to that the former stability functions are not sensitive to buoyancy.

At site C, χ, ϵ, ν_t', and ν_ρ' were calculated from profile measurements throughout the water column, and showed high turbulence level in the surface boundary layer and BBL, as well as in the mid layer where shear stress was induced by advected non-local water above a hypoxic layer. The relatively high dissolved oxygen in the non-local water resulted in upward and downward turbulent oxygen fluxes, and the bottom hypoxia will deform due to turbulence in 7.11 days. Two of the four models in the study at site D were implemented, and results showed that turbulence energy resulting from the non-local water was not well reproduced. We attribute this to the

lack of high-resolution velocity measurements for simulations. Model results agreed with observations only for χ and ϵ simulated from the model with the stability function of Cheng in the BBL. Discrepancies between model and observational results lead to the following conclusions: 1) the stability functions of Schumann and Gerz are too simple to represent the turbulent dynamics in stratified mid layers; 2) detailed velocity profiles measurements are required for models to accurately predict turbulence quantities. Missing such observations would result in underestimation, especially in the mid layer.

DEDICATION

To my LORD, Jesus Christ.

The LORD is my strength and my shield; my heart trusts in him, and he helps me. My heart leaps for joy, and with my song I praise him. (Psalm 28:7)

ACKNOWLEDGEMENTS

First and foremost, I would like to appreciate my committee chair, Dr. Ayal Anis, for his expert guidance, patience, encouragement, generosity, and love throughout my research and my life here. I would like to thank my co-chair Dr. Zhao Dongliang, and committee members, Dr. Robert D. Hetland, Dr. Douglas J. Klein, and Dr. Achim Stöessel, for their advices and guidance throughout the course of this research. Thanks also go to Dr. Alejandro Orsi who were so kind to help me out as the substitute for Dr. Achim Stöessel, even though the request was sent to him at a very late time before my defense.

I express my gratitude to Fahad Al Senafi as my comrade everyday, Josh R. Williams and Dr. Guan-hong Lee for manuscript reviews, Zhang Zhaoru for model simulations, Li Bo for explanations of hypoxia, Dr. Lars Umlauf and the GOTM user group for model parameterizations, Edmund Tedford from University of California, Santa Barbara for SCAMP toolbox and data analysis, Zhao Yan and Dr. Jiang Yuelu for biology-related discussions, Dr. Xu Chen, Dr. Zhang Saijin, Dr. Hsiu-Ping Li, Sherry Parker, and Herminia Sandoval for their constant care and encouragement, my friends Arjun Adhikari, Joseph A. Carlin, Mohammad Al-Mukaimi, Jessica DiGiulio, Michael Evans, Qu Fangyuan, Yang Chunxue, Li Xinxin, and Xu Zhao for having wonderful times with them, and Mrs. Ruthy Anis for her lovely baking over the years.

I would like to thank the NOAA Center for Sponsored Coastal Ocean Research (NA03NOS4780039 and NA06NOS4780198) for funding this research, Texas A&M University at Galveston for financial support as Teaching Assistantship, and the China Scholarship Council for 4-year stipend.

I am greatly indebted to my mother Ji Chunhua, my father Zhang Yongjun, my grandmother Yang Shuying, my aunt Zhang Yongjie, my uncle-in-law Han Shuzong, and my "brother" Khoi.

Finally, special thanks are given to all the people at the Galveston Chinese Church. I love you all, and God bless you all.

NOMENCLATURE

ADCP	Acoustic Doppler Current Profiler
ADV	Acoustic Doppler Velocimeter
BBL	Bottom Boundary Layer
CH	the $k-\epsilon$ turbulence closure with the stability functions of *Cheng et al.* (2002)
CHx	the $k-kL$ turbulence closure with the stability functions of *Cheng et al.* (2002)
CTD	Conductivity, Temperature, Depth sensor
DO	Dissolved Oxygen
DO_c	critical Dissolved Oxygen
GOTM	General Ocean Turbulence Model
HOBO	Onset® U22-001 water temperature logger
NCEP	National Centers for Environmental Prediction/Department of Energy Reanalysis 2
McFaddin	US Forest Service weather station
MCH	Mechanisms Controlling Hypoxia
NDBC 42035	National Data Buoy Center station 42035
NDBC LUML1	National Data Buoy Center station LUML1
NOAA	National Oceanic and Atmospheric Administration
PIV	Particle Image Velocimetry
SBL	Surface Boundary Layer
SCAMP	Self Contained Autonomous MicroProfiler
SG	the $k-kL$ turbulence closure with the stability functions of *Schumann and Gerz* (1995)

SGx	the $k-\epsilon$ turbulence closure with the stability functions of *Schumann and Gerz* (1995)
SST	Sea Surface Temperature
TKE	Turbulence Kinetic Energy
B	buoyancy production
C_D	drag coefficient
c_p	heat capacity of water
c_μ, c'_μ	stability functions
d_b	distance from the bottom
d_s	distance from the sea surface
D_{ij}	anisotropic shear production
E	energy spectrum
E_n	instrumental noise spectrum
E_{obs}	observed spectrum
f	frequency
F	wall function
g	gravitational acceleration
h	water depth
h_{O_2}	layer thickness
H_s	significant wave height
I	solar radiation
J_q^0	net surface heat flux
J_q^l	latent heat flux
J_q^{lw}	net longwave radiation
J_q^s	sensible heat flux
J_q^{sw}	net shortwave radiation
k	turbulence kinetic energy

k_B	Batchelor cutoff wavenumber
k_{wn}	radian wavenumber
$\hat{k}_{wn}$	cyclic wavenumber
L	length scale
l_0	height of the ADV's sampling volume above the bottom
M	shear frequency
N	buoyancy frequency
p	pressure
P	shear production
Pr_t	turbulent Prandtl number
R_i	gradient Richardson number
R_i^c	critical gradient Richardson number
R_{MAX}	maximal vertical range of valid ADCP measurement
S	salinity
S_{ij}	mean shear
t	wave period
t_{O_2}	time required to remove bottom hypoxia
T	temperature
u	velocity in the X direction
U	mean horizontal current speed
$\overline{u}_\infty$	free-stream mean velocity
U_r	mean wind speed at a reference height
v	velocity in the Y direction
V	horizontal mean current
V_{ij}	mean vorticity
w	velocity in the Z direction
W	falling speed of profiler

z	vertical distance
α	Kolmogorov constant
β_V	Ratios of σ to burst-averaged current speed
Γ	sum of the viscous and turbulent transport terms
δ	mean wave direction
δ_{ij}	Kronecker symbol
δ_z	thickness of the BBL
ϵ	dissipation rate of turbulence kinetic energy
ϵ_{ijl}	alternating tensor
θ	potential temperature
κ	von Kármán constant,
μ	dynamic viscosity
ν	kinematic viscosity
ν_S	haline diffusivity
ν_t	eddy viscosity
ν_T	thermal diffusivity
ν'_t	eddy diffusivity of temperature
ν'_ρ	eddy diffusivity of density
Π_{ij}	pressure-velocity correlator
Π_{iT}	pressure-temperature correlator
ρ	potential density
ρ_0	mean density
ρ_a	air density
σ	surface-wave-induced orbital velocity
τ	Reynold stress
τ_R	relaxation time
τ_{wind}	wind stress

χ	dissipation rate of temperature variance
ϕ	angle between wave and current
Ω	rotation rate of the earth

TABLE OF CONTENTS

LIST OF FIGURES

FIGURE Page

LIST OF TABLES

1. INTRODUCTION

1.1 Background

Turbulence is a random process. It transfers kinetic energy from larger to smaller scales, eventually dissipating this energy to heat through viscous processes. Turbulent processes tend to homogenize the fluid, enhance mixing, and increase transport rates of momentum, mass, and energy. These processes happen everywhere and are crucial in controlling flow dynamics and exchanges of momentum and water properties. However, turbulence is a research area in classical physics that is not yet fully understood. One of the reasons is due to its characteristics of chaos and randomness. The non-linear instability of turbulent flows makes the prediction of turbulence only possible in statistical ways.

Turbulence energy is supplied from different sources in different layers of the water column. In general, the latter is divided into surface boundary layer (SBL), mid layer, and bottom boundary layer (BBL).

In the SBL, turbulence energy is chiefly provided by surface forcing, e.g. momentum flux (τ_{wind}) and heat flux (J_q^0), and mixes tracers, e.g. temperature (T), salinity (S), and dissolved oxygen (DO). τ_{wind} is transferred by wind from the atmospheric surface layer to the SBL, and is commonly calculated using bulk parameterization of air-sea fluxes (*Fairall et al.*, 1996, 2003):

$$\tau_{wind} = \rho_a C_D U_r^2, \tag{1.1}$$

where ρ_a is the air density, C_D is the drag coefficient, and U_r is the mean wind speed at a reference height (typically 10 m) above the sea level (*Large and Pond*, 1981).

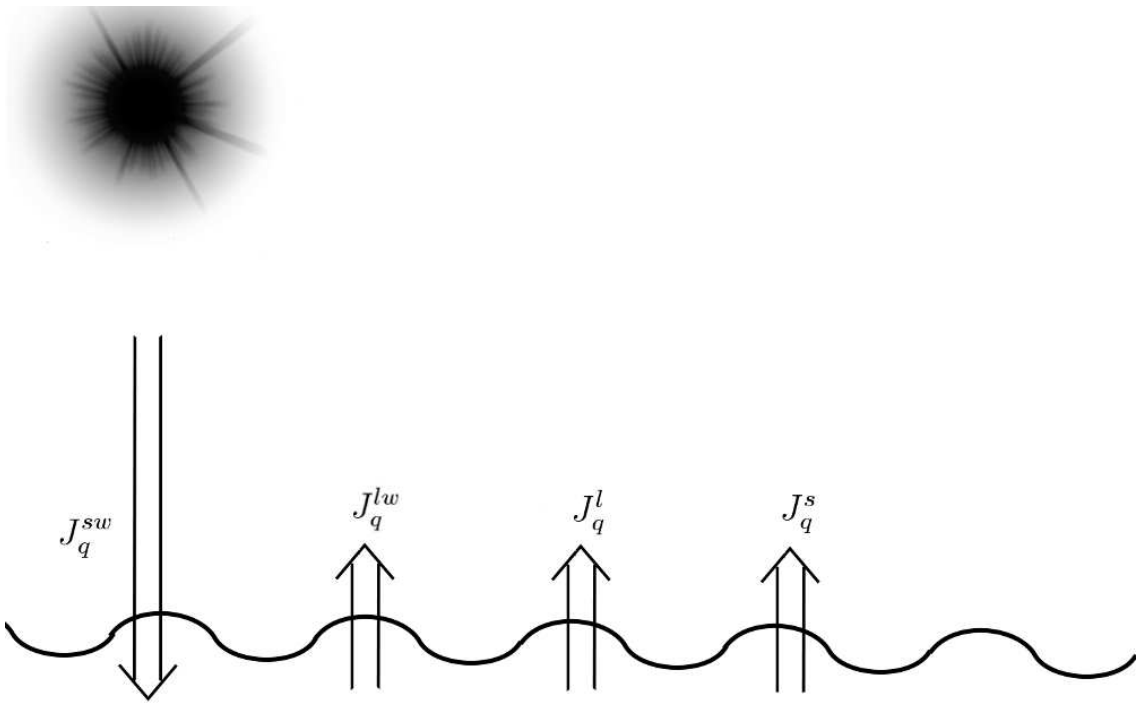

Figure 1.1: Net surface heat flux (J_q^0) consists of net flux of solar energy into the sea (J_q^{sw}), net flux of infrared radiation from the sea (J_q^{lw}), net latent heat flux due to evaporation or condensation (J_q^l), and net sensible heat flux due to conduction (J_q^s). Gain of heat in the ocean is considered positive, and loss is negative.

J_q^0 is the net surface heat flux. It changes the density of surface waters, thus the buoyancy. The net heat flux budget can be expressed as the sum of four individual components (Figure 1.1):

$$J_q^0 = J_q^{sw} + J_q^{lw} + J_q^l + J_q^s, \tag{1.2}$$

where J_q^{sw} is the net flux of solar energy into the sea, $-J_q^{lw}$ is the net flux of infrared radiation from the sea, J_q^l is the net latent heat flux due to evaporation or condensation, and J_q^s is the net sensible heat flux due to conduction. Gain of heat in the ocean, i.e. downward heat flux, is considered positive.

In the mid layer, internal wave breaking is the major source of turbulence energy. Internal waves are generated where stratification occurs, and although turbulence may be damped by stable stratification, when internal waves break, vertical mixing will take place. Another source of turbulence energy in the mid layer is the horizontal advection of water, the inflow would lead to intensified shear stress for vertical mixing.

In the BBL, turbulence energy is provided through shear stress induced by friction from the seabed. BBL turbulence may affect the distribution of sediments, and transport of particles and nutrients. The BBL generally is divided into three layers, a bed layer, a logarithmic layer and an outer layer (Figure 1.2, *Kundu and Cohen*, 2008). The bed layer is viscous and velocity fluctuations are minimal. The thickness of the bed layer is a few centimeters close to the bottom, in which shear stress is considered uniform and is equal to the stress (τ_0) at the bottom. The mean velocity ($\overline{u}$) is linearly distributed with distance (z) to the bottom:

$$\mu \frac{d\overline{u}}{dz} = \tau_0, \tag{1.3}$$

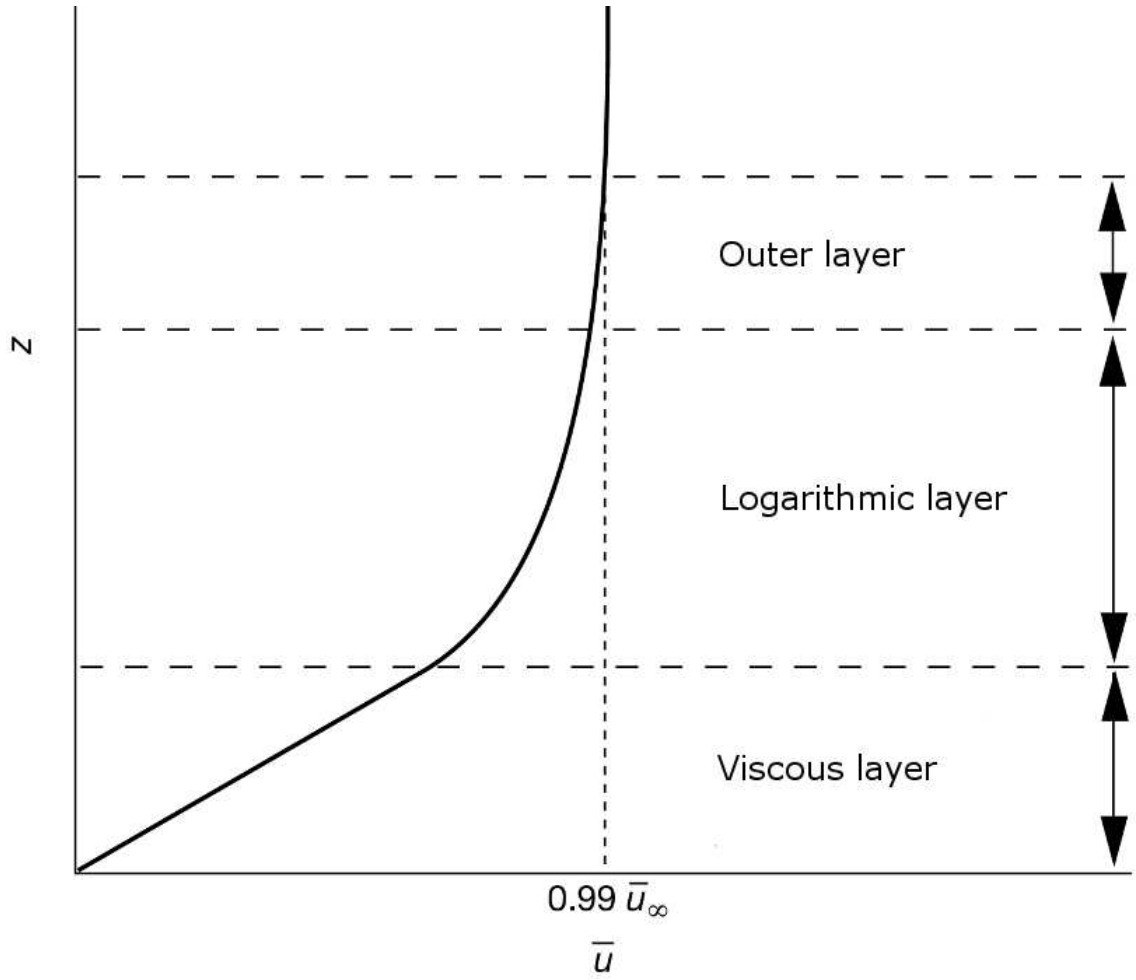

Figure 1.2: The BBL is divided into a viscous layer, a logarithmic layer, and an outer layer. $\overline{u}_\infty$ is the free-stream mean velocity. Heights of the three layers are sketched for clear identification and are not drawn to scale proportionally.

where μ is the dynamic viscosity. The logarithmic layer is a few meters thick. It has the general velocity profile

$$\frac{\overline{u}}{u_*} = \frac{1}{\kappa}\ln z + \text{const}, \tag{1.4}$$

where $\kappa \approx 0.41$ is the von Kármán constant, and u_* is the friction velocity given by:

$$u_* = \sqrt{\frac{\tau_0}{\rho}}, \tag{1.5}$$

where ρ is the water density. Equation (1.4) is called the law of the wall, and is valid only in the relatively thin layer in which z is greater than about $50\nu/u$, but less than about $0.2h$ (*Trowbridge et al.*, 1989), where $\nu = 1 \times 10^{-6}$ m^2 s^{-1} is the kinematic viscosity, and h is the water depth. For a hydrodynamically rough surface, it becomes

$$\frac{\overline{u}}{u_*} = \frac{1}{\kappa} ln \frac{z}{z_0}, \tag{1.6}$$

where z_0 is the height at which $\overline{u} = 0$ near the bottom. The outer layer is above the logarithmic layer with $\overline{u} = 0.99\overline{u}_\infty$ on top, where $\overline{u}_\infty$ is the free-stream mean velocity. The velocity distribution is given by the velocity defect law:

$$\frac{\overline{u} - \overline{u}_\infty}{u_*} = f\left(\frac{z}{\delta_z}\right), \tag{1.7}$$

where δ_z is the thickness of the BBL. Turbulence in the outer layer mainly depends on wall-free currents.

1.2 Objectives

Research on turbulence may help to understand dynamics in water columns under specific circumstances e.g., in our case, hypoxia. The Texas-Louisiana continental shelf, where our studies are located, has one of the biggest hypoxic zones around the

world (*Dale et al.*, 2010). The hypoxia is mainly caused by fresh water discharge and nutrient input from the Mississippi and Atchafalaya rivers (*Rabalais et al.*, 2002). Hypoxic zones usually form in the BBL (*Dagg et al.*, 2007), and the benthic ecosystem, as a result, is harmed by the depletion of DO near the bottom. Thus, it is critical to investigate water dynamics in the hypoxic zone so that plans for hypoxia management could be designed (*Walker et al.*, 2005). Here we examine the dynamics on the shelf focusing on turbulence.

Turbulence dynamics are described through turbulent fluxes, e.g. momentum flux ($\overline{u'w'}$ and $\overline{v'w'}$), heat flux ($\overline{T'w'}$), and salinity flux ($\overline{S'w'}$). However, it is difficult to observe those turbulent fluxes directly, thus studies usually are carried out using statistical analyses of turbulence quantities, e.g. turbulence kinetic energy (TKE), dissipation rate of TKE (ϵ), dissipation rate of temperature variance (χ), Reynolds stress (τ), eddy diffusivity of temperature (ν_t'), and eddy diffusivity of density (ν_ρ'). On one hand, high sampling rate instruments were developed for measuring currents (*Adrian*, 1991; *Voulgaris and Trowbridge*, 1998; *Nystrom et al.*, 2002), temperature and salinity (*MacIntyre et al.*, 1999; *Bourgault et al.*, 2008), oxygen (*Berg et al.*, 2003) etc.; on the other hand, numerical turbulence models have been developed using strategies such as direct numerical simulation (DNS, *Moin and Mahesh*, 1998), large eddy simulation (LES, *Mason*, 1994; *Meneveau and Katz*, 2000), and statistical turbulence closure models (*Burchard et al.*, 2008). It is advantageous to understand turbulence dynamics through a combination of observations of turbulence quantities and numerical model simulations.

The present research consists of two studies. In the first study, measured high-resolution velocities at one point in the BBL are used for observational schemes. The other measured parameters, e.g. profiles of velocity, temperature, and salinity, and surface heat and momentum fluxes, are used to force numerical turbulence models.

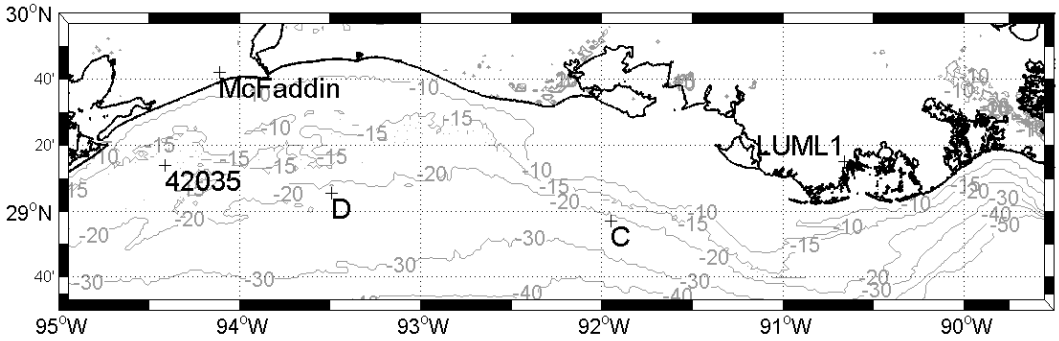

Figure 1.3: Measurements for the two studies were conducted, respectively, at sites C and D on the Texas - Louisiana continental shelf. Distance between the two sites is 150 km. Downward shortwave radiation was obtained from the weather station McFaddin. Wind speed, air temperature, relative humidity, and air pressure were measured at NDBC stations LUML1 and 42035, and were used for calculations of momentum flux, and sensible and latent heat fluxes for sites C and D, respectively. Depth contours are in m.

The turbulence quantities estimated from observations and model simulations are compared, and differences between the models are investigated. In the second study, χ, ϵ, ν_t', and ν_ρ' are estimated from high-resolution measurements of temperature throughout the water column at a nearby site, and the same models as in the first study are used to compare numerical simulation results to observations.

1.3 Study sites

A field campaign as part of the NOAA Mechanisms Controlling Hypoxia (MCH) project was conducted on the continental shelf of the Gulf of Mexico in Aug., 2005 during hypoxic conditions (*Rabalais et al.*, 2007). The MCH aimed to study hypoxia and its relation to physical and biogeochemical processes (for details see

http://hypoxia.tamu.edu). Measurements for the first study were carried out at site D (29°5′45″N 93°29′44″W, Figure 1.3) 73 km off the coast from Aug. 18 to 24, and those for the second study were carried out at site C (28°56′55″N 91°57′5″W, Figure 1.3) 58 km off the coast from Aug. 22 20:00 to Aug. 23 20:00. Both sites have water depths $\sim$ 21 m. Time is given in UTC (CDT + 5 h).

1.4 Instrumentation

General types of instruments for turbulence measurements are introduced in Section 1.4.1, and the instruments used in our studies and the parameters they measure are presented in Section 1.4.2.

1.4.1 General types of instruments for turbulence measurements

The first measurements of oceanic turbulence were made by *Grant et al.* (1962) using a hot film anemometer in a tidal channel. From then on, many measuring devices were designed and implemented (*Lueck et al.*, 2002; *Burchard et al.*, 2008). Hot-film anemometers and cold-film thermometers were employed in early studies, and were later replaced by shear probes and micro-thermistors (*Lueck et al.*, 2002). Shear probes use piezoceramic beams which are sensitive to the cross-stream components of the flow, and the consequent lifting force is converted to a proportional voltage. *Lueck et al.* (2002) gave a review of shear probes, and *Prandke et al.* (2000) detailed the processing of probe data. Application examples of shear probes are: *Lueck and Huang* (1999) deployed multiple shear probes 15 m above the sea floor at the mid depth of a channel; *Rippeth et al.* (2003) measured the current microstructure from $\sim$ 5 m beneath the surface to 0.15 m above the seabed by a Fast Light Yo-yo (FLY) shear probe (*Dewey et al.*, 1987); *Wolk et al.* (2002) assembled a shear probe with other sensors to a profiler called TurboMAP. The TurboMAP resolved ϵ values as low as 5×10^{-10} m^2 s^{-3} in an off-shelf region.

Another type of instruments is designed to use the Doppler effect. The pulse is reflected back from moving particles advected by the flow with different frequencies of sound waves, and the speed of the particles is calculated from the change of the reflected sound frequency due to the current (*Voulgaris and Trowbridge*, 1998). Those instruments include acoustic Doppler current profilers (ADCPs) and acoustic Doppler velocimeters (ADVs). The ADCP measures currents in vertical profiles with different bin sizes. High-frequency ADCPs have been employed in many shelf and estuarine studies for turbulence measurements (e.g., *Stacey et al.*, 1999a,b; *Rippeth et al.*, 2002), assuming the homogeneity of statistics along beams and large-scale anisotropy (*Nystrom et al.*, 2007). *Stacey et al.* (1999a) and *Rippeth et al.* (2002) calculated TKE and τ in tidal flows from ADCPs. *Stacey et al.* (1999b) estimated ϵ and τ in a partially stratified estuary from an ADCP. *Lu et al.* (2000) deployed an ADCP in a swift tidal channel with weak stratifications for τ estimation. The ADV measures currents at high sampling rate in a small sampling water volume (*Kraus et al.*, 1994; *Lane et al.*, 1998; *Voulgaris and Trowbridge*, 1998; *Lopez and Garcia*, 2001). For a detailed evaluation of ADV for turbulence measurements, see *Voulgaris and Trowbridge* (1998). Application examples of ADVs are : *Voulgaris and Trowbridge* (1998) measured ϵ 3.1 cm above the bottom of a laboratory flume; *Richards et al.* (2013) investigated the effect of shoaling internal wave on turbulence in an estuary; *Inoue et al.* (2008) used an ADV attached to an elevation system to measure vertical profiles of flow from 0.1 - 27 cm above the sediment surface.

Particle image velocimetry (PIV) systems have been used in oceanic turbulence measurements (*Liu et al.*, 1994; *Bertuccioli et al.*, 1999; *Doron et al.*, 2001; *Smith et al.*, 2002, 2005). The PIV illuminates the fluid with a laser sheet and takes snapshots of the microscopic tracer particles. The displacements of particles represent the currents, thus 2-dimensional velocity distributions are captured. PIV has been

Parameter	Site C			Site D			
	CTD	SCAMP	ADCP	ADCP	HOBO	CTD	ADV
velocity			profile	profile			bottom
conductivity	profile	profile				profile	
temperature	profile	profile		bottom	surface bottom	profile	bottom
pressure	profile	profile	profile	bottom		profile	bottom
PAR	profile	profile					
DO	profile						

Table 1.1: Types of data measured from our instruments. The CTD at site C was ship deployed, and the CTD at site D was mounted on the WireWalker. The ADCP at site C was ship-hull mounted, and the ADCP at site D was bottom mounted.

widely deployed for BBL turbulence studies.

Vertical turbulence structures can be examined using temperature and conductivity profiles measured from high sampling rate thermistors and conductivity sensors (*Imberger and Ivey*, 1991; *Kocsis et al.*, 1999; *Sharples et al.*, 2001; *Jurado et al.*, 2012). Such sensors include e.g. the FP07 thermistor (GE Measurement & Control) and the Micro-conductivity sensors SBE7 (Sea Bird Electronics) and 5346 (Precision Measurement Engineering). FP07 is carried on the Self-Contained Autonomous Microstructure Profiler (SCAMP, Precision Measurement Engineering) and the Vertical Microstructure Profiler (VMP, Rockland Scientific Instruments). SBE7 and 5346 are equipped on VMP (*Bourgault et al.*, 2008) and SCAMP (SCAMP manual), respectively. Applications of these sensors for temperature and conductivity microstructure measurements can be found in *Ruddick et al.* (2000); *Anis* (2006); *Anis and Singhal* (2006); *Beaird et al.* (2012).

1.4.2 Instruments used in this research

At site D, a bottom-mount pod, 0.6 m in height, was set up on the sea floor (Figure 1.4). The instruments installed on the pod include an upward looking ADCP (1 MHz,

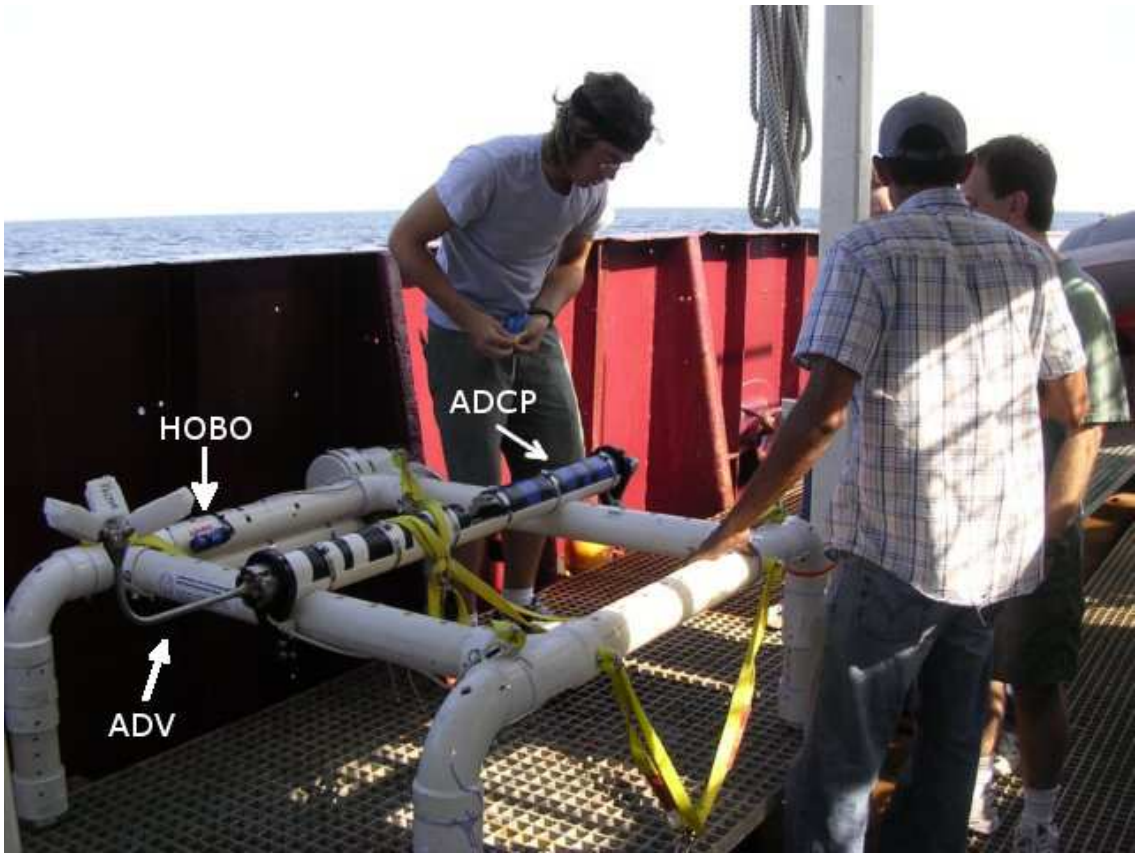

Figure 1.4: The ADV with upward looking transducers, the ADCP and the HOBO were attached on the bottom-mount pod (photograph courtesy Dr. Ayal Anis).

Figure 1.5: The CTD attached at the center of the WireWalker was ready to be lowered into the sea for autonomous profiling powered by surface wave energy (photograph courtesy Dr. Ayal Anis).

Nortek Aquadopp), an ADV (1–64 Hz, Nortek Vector) and a temperature logger (up to 1 Hz, Onset HOBO). The Conductivity, Temperature, and Depth instrument (up to 6 Hz, RBR CTD) was mounted on a WireWalker, a surface-wave powered vehicle (*Rainville and Pinkel*, 2001), and profiled along a vertical wire autonomously (Figure 1.5). Another HOBO was attached beneath the surface buoy to record sea surface temperature (SST).

At site C, another ADCP (150 kHz, Teledyne RD Instruments) was mounted on the hull of the research vessel Gyre. Free-falling casts of the SCAMP (profile rate 100 Hz) were conducted. The SCAMP includes two fast thermistors, a fast conductivity sensor, an accurate conductivity-temperature sensor, a depth transducer, and a photosynthetically active radiation (PAR) sensor. The CTD (24 Hz, Sea-Bird Electronics SBE 911) on the R/V Gyre measured temperature, conductivity, pressure, fluorescence, DO, and PAR. A summary of the instruments and measured parameters is given in Table 1.1.

Measurements from the ADV were used for estimation of ϵ, TKE, and τ in the BBL at site D, and those of the SCAMP were used for estimations of χ, ϵ, ν_t', and ν_ρ' throughout the water column at site C. Observational data (e.g. hydrographic data and surface meteorology) were used for turbulence simulations by numerical modeling methods.

1.5 Observational analytical methods

Next, the methods used to calculate the turbulence quantities, ϵ, TKE, τ, χ, ν_t', and ν_ρ' are introduced.

ϵ in isotropic turbulence can be calculated from the microstructure velocity shear $\frac{\partial u}{\partial z}$ or $\frac{\partial u}{\partial x}$:

$$\epsilon = \frac{15}{2}\nu\overline{\left(\frac{\partial u}{\partial z}\right)^2} = 15\nu\overline{\left(\frac{\partial u}{\partial x}\right)^2}, \tag{1.8}$$

$\frac{\partial u}{\partial z}$ can be converted from the measured temporal gradient $\frac{\partial u}{\partial t}$ using Taylor's frozen turbulence hypothesis (*Taylor*, 1938; *Oakey*, 1982):

$$\frac{\partial u}{\partial z} = \frac{1}{W}\frac{\partial u}{\partial t}, \tag{1.9}$$

where W is the free-falling speed of the profiler.

ϵ can also be estimated using Kolmogorov's -5/3 hypothesis (*Kolmogorov*, 1941) and the energy spectrum of velocity fluctuations. In the inertial subrange, between the energy-containing range and the dissipation range, the energy spectrum is given by:

$$E(k_{wn}) = \alpha\epsilon^{\frac{2}{3}}k_{wn}^{-\frac{5}{3}}, \tag{1.10}$$

where α is the Kolmogorov constant, and k_{wn} is the radian wavenumber. This equation describes that $E(k_{wn})$ decays with a $-\frac{5}{3}$ slope in logarithmic scale. Since velocities are measured in the time domain, Taylor's frozen turbulence hypothesis can be applied to convert the energy spectrum from frequency (f) space to wavenumber space as follows:

$$E(k_{wn}) = \frac{E(f)U}{2\pi}, \tag{1.11}$$

where U is the mean horizotal current velocity. ϵ can then be estimated from

$$E(f) = (2\pi)^{-\frac{2}{3}}U^{-\frac{8}{3}}\alpha\epsilon^{\frac{2}{3}}f^{-\frac{5}{3}} \tag{1.12}$$

by fitting a -5/3 line to the spectrum in the inertial subrange. This method has been applied to measurements from different types of instruments, e.g. ADV (*Gross and Nowell*, 1985; *McPhee*, 1998), PIV (*Bertuccioli et al.*, 1999), and ADCP (*Jonas et al.*, 2003).

TKE is a function of the variances of u, v, and w in an isotropic flow and is given by

$$k = \frac{1}{2}\left(\overline{u'^2} + \overline{v'^2} + \overline{w'^2}\right). \tag{1.13}$$

In general, τ is given by

$$\tau = \rho\overline{u'w'} \text{ or } \tau = \rho\overline{v'w'}, \tag{1.14}$$

while in the bed layer where the flow is steady and homogeneous (*Perlin et al.*, 2005; *Arneborg et al.*, 2007),

$$\epsilon = -\overline{u'w'}\frac{dU}{dz}, \tag{1.15}$$

where

$$\overline{u'w'} = u_*^2, \tag{1.16}$$

and

$$\frac{dU}{dz} = \frac{u_*}{l}, \tag{1.17}$$

$$l = \kappa z, \tag{1.18}$$

such that

$$\epsilon = \frac{u_*^3}{\kappa z}, \tag{1.19}$$

and according to equation (1.5), τ can be expressed by

$$\tau = \rho(\epsilon\kappa z)^{\frac{2}{3}}. \tag{1.20}$$

χ is calculated from the integral of the spectrum of the vertical gradient of tem-

perature fluctuations $\partial_z T'$:

$$\chi = 6\nu' \overline{(\partial_z T')^2} = 6\nu' \int_t^\infty \left(S_{obs}(\hat{k}_{wn}) - S_n(\hat{k}_{wn}) \right) d\hat{k}_{wn}, \tag{1.21}$$

where ν' is the thermal diffusivity , $\hat{k}_{wn} = k_{wn}/2\pi$ is the cyclic wavenumber, S_{obs} is the observed spectrum, and S_n is the instrument's noise spectrum.

ϵ can be estimated by fitting the spectrum of $\partial_z T'$ to the theoretical Batchelor spectrum (*Dillon and Caldwell*, 1980; *Oakey*, 1982), and is expressed as:

$$\epsilon = k_B^4 \nu \nu'^2, \tag{1.22}$$

where k_B is the Batchelor cutoff wavenumber estimated from the Batchelor spectrum:

$$S(\hat{k}_{wn}) = \left(\frac{q}{2}\right)^{\frac{1}{2}} \frac{\chi}{k_B \nu'} g(q, \hat{k}_{wn}/k_B), \tag{1.23}$$

where q is between 3.4 and 4.1 (*Dillon and Caldwell*, 1980; *Oakey*, 1982), and

$$g(q, \hat{k}_{wn}/k_B) = 2\pi \left(e^{-\alpha^2/2} - \alpha \int_\alpha^\infty e^{-x^2/2} dx \right), \tag{1.24}$$

where

$$\alpha = (2q)^{\frac{1}{2}} \frac{2\pi \hat{k}_{wn}}{k_B}. \tag{1.25}$$

ν'_t and ν'_ρ are functions of χ and ϵ, respectively, and are given by

$$\nu'_t = \frac{\chi}{2} \left(\frac{\partial T}{\partial z} \right)^{-2}, \tag{1.26}$$

and

$$\nu'_\rho = \Gamma \frac{\epsilon}{N^2}, \tag{1.27}$$

where Γ is the mixing efficiency, it varies between 0.04 and 0.4 (*Peters et al.*, 1995) and is commonly chosen as 0.2 (*Osborn*, 1980; *Moum*, 1996; *Nash et al.*, 2007).

1.6 Turbulence numerical models

1.6.1 Types of numerical models

The development of turbulence models has a history for decades. All models are based on the Navier-Stokes equations with the Boussinesq approximation (*Boussinesq*, 1903; *Spiegel and Veronis*, 1960):

$$\partial_t v_i + v_j \partial_j v_i - \nu \partial_{jj} v_i + 2\epsilon_{ijl}\Omega_j v_l = -\frac{\partial_i p}{\rho_0} - \frac{g_i}{\rho_0}\rho, \tag{1.28}$$

and the continuity equation:

$$\partial_j v_j = 0, \tag{1.29}$$

where the subscripts i,j,l denote axes in a Cartesian coordinate system, v is the current velocity, Ω is the rotation rate of the earth, p is the pressure, ρ_0 is a constant reference density, g is the gravitational acceleration, ρ is the potential density, and ϵ_{ijl} is the alternating tensor (*Kundu and Cohen*, 2008). The tracer equations for T and S are required for ρ calculation, and can be derived by approaches similar to the Navier-Stokes equations. The equation for T is

$$\partial_t T + v_j \partial_j T - \nu_T \partial_{jj} T = \frac{\partial_z I}{c_p \rho_0}, \tag{1.30}$$

where ν_T is the thermal diffusivity, I is the local solar radiation in the water, and c_p is the heat capacity of water. S is expressed by

$$\partial_t S + v_j \partial_j S - \nu_S \partial_{jj} S = 0, \tag{1.31}$$

where ν_S is the haline diffusivity. ρ can be calculated as a function of T, S, and p through a state equation:

$$\rho = \rho(T, S, p). \tag{1.32}$$

The numerical solutions for hydrodynamical processes can be found from the set of Eq. (1.28) - (1.32), and the methods include DNS (e.g. *Smyth et al.*, 2001), LES (e.g. *Skyllingstad et al.*, 1999), and one-point closure models (e.g. *Umlauf and Burchard*, 2005).

DNS resolves viscous scales, thus computational limits restrict its applications to small-scale eddies with low Reynolds number $R_e = vL/\nu$ up to 10^4. In the oceanic mixed layer, a typical velocity scale of $v = 0.1\text{ms}^{-1}$, a length scale of $L = 1$ m, and $\nu = 10^{-6}\text{m}^2\text{s}^{-1}$ for water at 20°C result in $R_e = 10^5$; in the open ocean, $L = 10^6$ m, $R_e = 10^{11}$, thus DNS is incapable of resolving large (i.e. energy-containing) eddies. One attempt to solve the shortcoming of DNS is LES. LES applies to convective turbulence in which the size of eddies is relatively large with respect to the relevant mean flow scale (e.g. the mixed layer depth) processes. LES, in constrast, is computationally costly for resolving small size energy-containing eddies.

One-point closure models use parameterizations to simulate turbulence in a statistical sense. Velocity, temperature, pressure and salinity are commonly investigated by decomposing these variables into mean and fluctuating components (Reynolds decomposition, *Reynolds*, 1895; *Lesieur*, 2008). For instance, the velocity is given by:

$$v_i = \overline{v}_i + v_i', \tag{1.33}$$

Equations (1.28) - (1.31) are then given by:

$$\partial_t \overline{v}_i + \overline{v}_j \partial_j \overline{v}_i - \partial_j \left(\nu \partial_j \overline{v}_i - \overline{v_j' v_i'} \right) + 2\epsilon_{ijl}\Omega_j \overline{v}_l = -\frac{\partial_i \overline{p}}{\rho_0} - g_i \frac{\overline{\rho}}{\rho_0}, \tag{1.34}$$

$$\partial_j \overline{v}_j = 0, \tag{1.35}$$

$$\partial_t \overline{T} + v_j \partial_j \overline{T} - \partial_j \left(\nu_T \partial_j \overline{T} - \overline{v_j' T'} \right) = \frac{\partial_z I}{c_p \rho_0}, \tag{1.36}$$

$$\partial_t \overline{S} + v_j \partial_j \overline{S} - \partial_j \left(\nu_S \partial_j \overline{S} - \overline{v_j' S'} \right) = 0. \tag{1.37}$$

There are unknown second-moment turbulent fluxes in the equations, i.e. Reynolds stress $\overline{v_j' v_i'}$, turbulent heat flux $\overline{v_j' T'}$, and turbulent salt flux $\overline{v_j' S'}$, which need to be resolved by the transport equations at the next higher order:

$$\begin{aligned}
&\partial_t \overline{v_i' v_j'} + \partial_l \left(\overline{v}_l \overline{v_i' v_j'} + \overline{v_l' v_i' v_j'} - \nu \partial_l \overline{v_i' v_j'} \right) \\
&\quad = -\partial_l \overline{v}_i \overline{v_l' v_j'} - \partial_l \overline{v}_j \overline{v_l' v_i'} - 2\Omega_l \left(\epsilon_{ilm} \overline{v_j' v_m'} + \epsilon_{jlm} \overline{v_i' v_m'} \right) \\
&\quad - \frac{1}{\rho_0} \left(g_i \overline{v_j' \rho'} + g_j \overline{v_i' \rho'} \right) - \frac{1}{\rho_0} \overline{v_i' \partial_j p' + v_j' \partial_i p'} \\
&\quad - 2\nu \overline{\partial_l v_j' \partial_l v_i'},
\end{aligned} \tag{1.38}$$

$$\begin{aligned}
&\partial_t \overline{v_i' T'} + \partial_j \left(\overline{v}_j \overline{v_i' T'} + \overline{v_i' v_j' T'} - (\nu + \nu') \partial_j \overline{v_i' T'} \right) \\
&\quad + \nu' \overline{T' \partial_{jj} v_i'} + \nu \overline{v_i' \partial_{jj} T'} \\
&\quad = -\overline{v_i' v_j'} \partial_j \overline{T} - \partial_j \overline{v}_i \overline{v_j' T'} - 2\epsilon_{ijl} \Omega_j \overline{v_l' T'} \\
&\quad - \frac{g_i}{\rho_0} \overline{T' \rho'} - \frac{1}{\rho_0} \overline{T' \partial_i p'} + v_j' \partial_i p' - 2(\nu + \nu') \overline{\partial_j v_i' \partial_j T'},
\end{aligned} \tag{1.39}$$

$$\begin{aligned}
&\partial_t \overline{T'^2} + \partial_j \left(\overline{v}_j \overline{T'^2} + \overline{v_j' T'^2} + \nu' \partial_j \overline{T'^2} \right) = \\
&\quad - 2\overline{v_j' T'} \partial_j \overline{T} - 2\nu' \overline{(\partial_j T')^2},
\end{aligned} \tag{1.40}$$

$$\partial_t\overline{T'S'} + \partial_j\left(\overline{v}_j\overline{T'S'} + \overline{v'_jT'S'} + (\nu' + \nu'')\partial_j\overline{T'S'}\right) =$$
$$-\overline{v'_jS'}\partial_j\overline{T} - \overline{v'_jT'}\partial_j\overline{S} - 2(\nu' + \nu'')\overline{\partial_jT'\partial_jS'} \tag{1.41}$$
$$-\nu'\overline{T'\partial_{jj}S'} - \nu''\overline{S'\partial_{jj}T'}.$$

The undetermined third moments ($\overline{v'_iv'_jk'_k}$, $\overline{v'_iv'_jT'}$, $\overline{v'_iT'^2}$, $\overline{v'_iT'S'}$) and pressure-strain correlators $\prod_{ij} = \frac{1}{\rho_0}\overline{v'_i\partial_jp' + v'_j\partial_ip'}$ and $\prod_{iT} = \frac{1}{\rho_0}\overline{T'\partial_ip'}$ need to be resolved by transport equations at the next higher order, and so on. The infinite repetition of this procedure prevents turbulence equations from being closed, referred to as the closure problem (*Haltiner and Williams*, 1980; *Vallis*, 2006). To close the turbulence transport equations, the third moments in Eqs. (1.38) - (1.41) may be neglected assuming local equilibrium, and parameterizations for $\prod_{ij}$ and $\prod_{iT}$ to the known second moments and mean flow quantities can be derived in several ways (*Burchard*, 2002). For example, $\prod_{ij}$ and $\prod_{iT}$ have the following general expressions in *Kantha and Clayson* (1994), *Burchard and Baumert* (1995), and *Canuto et al.* (2001):

$$\begin{aligned}\prod_{ij} =& c_1\frac{\epsilon}{k}\left(\overline{v'_iv'_j} - \frac{2}{3}\delta_{ij}k\right) + c_2\left(P_{ij} - \frac{2}{3}\delta_{ij}P\right) + \\ & c_3\left(B_{ij} - \frac{2}{3}\delta_{ij}B\right) + c_4\left(D_{ij} - \frac{2}{3}\delta_{ij}P\right) + \\ & c_5kS_{ij},\end{aligned} \tag{1.42}$$

where δ_{ij} is the Kronecker symbol, P_{ij} is the shear production:

$$P_{ij} = -\partial_l\overline{v}_i\overline{v'_lv'_j} - \partial_l\overline{v}_j\overline{v'_lv'_i}, \tag{1.43}$$

B_{ij} is the buoyancy production:

$$B_{ij} = -\frac{1}{\rho_0}\left(g_i\overline{v_j'\rho'} + g_j\overline{v_i'\rho}\right), \tag{1.44}$$

S_{ij} is the mean shear:

$$S_{ij} = \frac{1}{2}\left(\partial_i\overline{v}_j + \partial_j\overline{v}_i\right), \tag{1.45}$$

D_{ij} is the anisotropic shear production:

$$D_{ij} = -\overline{v_i'v_l'}\partial_j\overline{v}_l - \overline{v_j'v_l'}\partial_i\overline{v}_l, \tag{1.46}$$

P is the shear production:

$$P = -\partial_i\overline{v}_j\overline{v_i'v_j'}, \tag{1.47}$$

and B is the buoyancy production:

$$B = -\frac{g}{\rho_0}\overline{v_3'\rho'}; \tag{1.48}$$

$$\begin{aligned}\prod_{iT} =& c_{1T}\frac{\epsilon}{k}\overline{v_i'T'} + c_{2T}\overline{v_j'T'}\partial_j\overline{u}_i - \\ & c_{3T}\frac{g_i}{\rho_0}\partial_T\rho\overline{T'^2} - c_{4T}\overline{v_i'T'}V_{ij},\end{aligned} \tag{1.49}$$

where V_{ij} is the mean vorticity:

$$V_{ij} = \frac{1}{2}\left(\partial_j\overline{v}_i - \partial_i\overline{v}_j\right). \tag{1.50}$$

Assumptions for turbulence closures are (*Burchard*, 2002):

- boundary layer approximation
- neglect or simplification of second-moment transports

- neglect of rotational terms in the second-moment equations
- neglect of tracer cross-correlations
- parameterization of pressure-strain correlators
- parameterization of dissipation terms

The models applied in the present study are one-point statistical closure models, which meet the requirements below (*Umlauf and Burchard*, 2005):

- comprehensive physical meaning
- computational economy
- numerical robustness
- applicability in three-dimensional models

Predicted turbulence quantities, e.g. TKE, ϵ, τ, and χ, from one-point statistical closure models can be compared to those estimated from measurements. A large number of comparative studies for these quantities have been reported in the literature (e.g. *Clayson and Kantha*, 1999; *Burchard et al.*, 2002; *Simpson et al.*, 2002; *Stips et al.*, 2002; *Anis and Singhal*, 2006).

Second-moment two-equation turbulence models, as one type of one-point statistical closure models, have proven to be a good compromise between complexity and simplification (*Stips et al.*, 2002). Those models close equations (1.34) - (1.37) at second moments, and use two transport equations for the second-moment turbulent fluxes. One transport equation is of TKE (denoted as k in models) and the other is of L or a L related quantity (e.g. ϵ, ω, or τ, *Umlauf and Burchard*, 2003).

The turbulent fluxes are functions of a turbulent diffusivity and a mean flow gradient:

$$\overline{u'w'} = -\nu_t \frac{\partial \overline{u}}{\partial z}, \tag{1.51}$$

$$\overline{v'w'} = -\nu_t \frac{\partial \overline{v}}{\partial z}, \tag{1.52}$$

$$\overline{T'w'} = -\nu'_t \frac{\partial \overline{T}}{\partial z}, \tag{1.53}$$

$$\overline{S'w'} = -\nu'_t \frac{\partial \overline{S}}{\partial z}, \tag{1.54}$$

where ν_t is the eddy viscosity. In the $k-\epsilon$ turbulence closure,

$$\nu_t = (c^0_\mu)^3 c_\mu \frac{k^2}{\epsilon}, \tag{1.55}$$

$$\nu'_t = (c^0_\mu)^3 c'_\mu \frac{k^2}{\epsilon}, \tag{1.56}$$

and in the $k-kL$ turbulence closure,

$$\nu_t = c_\mu k^{\frac{1}{2}} L, \tag{1.57}$$

$$\nu'_t = c'_\mu k^{\frac{1}{2}} L, \tag{1.58}$$

where c^0_μ is a constant, and c_μ and c'_μ are non-dimensional stability functions that describe the influence of shear and buoyancy on turbulent mixing. c_μ and c'_μ can be constants, empirical functions, or functions of non-dimensional flow parameters resulting from a higher-order turbulence model (*Burchard*, 2002).

In the $k-\epsilon$ turbulence closure, the transport equation for k is:

$$\partial_t k - \partial_z \left(\left(\nu + \frac{\nu_t}{\sigma_k} \right) \partial_z k \right) = P + B - \epsilon, \tag{1.59}$$

where σ_k is the turbulent Schmidt number for vertical flux of TKE; the other transport equation for the L related quantity is:

$$\partial_t \epsilon - \partial_z \left(\left(\nu + \frac{\nu_t}{\sigma_\epsilon} \right) \partial_z \epsilon \right) = \frac{\epsilon}{k} \left(c_{1\epsilon} P + c_{3\epsilon} B - c_{2\epsilon} \epsilon \right), \tag{1.60}$$

where σ_ϵ is the turbulent Schmidt number for vertical flux of ϵ, $c_{1\epsilon} = 1.44$, $c_{2\epsilon} = 1.92$, and $c_{3\epsilon} = 1$.

In the $k - kL$ turbulence closure, the transport equation for k is:

$$\partial_t k - \partial_z \left(S_q \sqrt{2k} L \partial_z k \right) = P + B - \epsilon, \tag{1.61}$$

where $S_q = 0.2$ (*Simpson et al.*, 1996); the other transport equation for L related quantity is:

$$\partial_t (kL) - \partial_z \left(S_l \sqrt{2k} L \partial_z (kL) \right) = \frac{L}{2} \left(E_1 P + E_3 B - \left(1 + E_2 \left(\frac{L}{L_z} \right)^2 \right) \epsilon \right), \tag{1.62}$$

where $S_l \approx 0.2$, $E_1 = 1.8$, $E_2 = 1.33$, and E_3 is a function of the gradient Richardson number (R_i) and stability functions (*Mellor and Yamada*, 1982).

1.6.2 The general ocean turbulence model

The one-dimensional General Ocean Turbulence Model (GOTM; *Burchard* 2002) is used for the numerical simulations in the present study. The GOTM is a program that implements different turbulence models, e.g. empirical models, two-equation models, algebraic stress models, K-profile parameterizations (KPP), etc. The GOTM is widely used due to less complexity and prominent contribution in saving computational time compared to three-dimensional models. Applications of the GOTM are made for model-observation comparisons for ϵ (*Bolding et al.*, 2002), χ (*Anis*

and Singhal, 2006), and depth of mixed layer (*He and Chen*, 2011), as well as inter-model comparisons (*Burchard and Bolding*, 2001; *Burchard et al.*, 2002). Several processes (e.g. horizontal variability, shear instability, and internal waves) treated prognostically in three-dimensional models have to be either prescribed or neglected, depending on their relevance for the processes under investigation (*Burchard et al.*, 1999; *Simpson et al.*, 2002; *Baumert et al.*, 2005). Observational data can be used as external forcing and validation. Setting of relaxation time allows for nudging simulated hydrographic variables, e.g. temperature, salinity and current velocity, to observed profiles, by which the horizontal gradients are provided for one-dimensional models in the GOTM. Among the diverse second-moment two-equation turbulence closure models, the $k - kL$ turbulence closure models (*Mellor and Yamada*, 1982; *Burchard et al.*, 1999) and the $k - \epsilon$ turbulence closure models (*Launder and Spalding*, 1972; *Rodi*, 1987; *Burchard et al.*, 1998; *Canuto et al.*, 2001) are commonly used, and are applied in the following studies.

2. OBSERVATIONS AND MODEL SIMULATIONS OF TURBULENCE IN THE BOTTOM BOUNDARY LAYER OF THE TEXAS-LOUISIANA CONTINENTAL SHELF

2.1 Introduction

The northern Gulf of Mexico has one of the largest hypoxic regions in the world (16,500 km^2 on average; *Dale et al.*, 2010). The formation of hypoxia is believed to be caused primarily by excess anthropogenic nitrogen inputs to the coastal sea and seasonal vertical stratification (*Bianchi et al.*, 2010; *Liu et al.*, 2010). Nitrogen inputs elevate primary production in the surface boundary layer (SBL), and the increased organic matter sinks to the bottom boundary layer (BBL), causing high respiration rate. Stratification is induced by fresh water discharge and surface heating, and suppresses vertical transport of dissolved oxygen from the surface to the bottom through the pycnocline. These two effects result in a hypoxic bottom-water zone (*Dagg et al.*, 2007). Thus it is important to understand the physical processes in the BBL where turbulence is a key parameter in the micro-scale dynamics.

Turbulence is a major driving mechanism of mixing processes and fluxes of various waterborne substances ranging from dissolved matter to sediments. In the BBL turbulence activity is enhanced by shear stress near the bed, and contributes to destruction of stratification and an increase in the vertical transport of oxygen and nutrients. Since direct measurements of turbulence fluxes in the ocean pose significant technical difficulties, studies typically examine turbulence quantities such as turbulence kinetic energy (TKE, denoted as k in numerical models), TKE dissipation rate (ϵ), and Reynolds stress (τ), from which fluxes may then be estimated (*Tennekes and Lumley*, 1972).

Methods to study such turbulence quantities may include observations and model simulations. Here, high-frequency measurements of current velocities from an acoustic Doppler velocimeter (ADV) in the BBL were used to estimate ϵ, using Kolmogorov's -5/3 hypothesis for energy spectra in the inertial subrange (*Kolmogorov*, 1941). In a shallow water environment, orbital motions due to surface waves may affect turbulence in the BBL (*Lumley and Terray*, 1983; *Grant and Madsen*, 1986). To remove the effects of surface-wave-induced orbital velocities (σ) in the BBL, we applied a modified equation of energy spectrum in the inertial subrange introduced by *Trowbridge and Elgar* (2001). TKE was estimated from the integration of the energy spectrum under the -5/3 logarithmic fitting line extended from the demarcation of energy-containing range and inertial subrange (*Pope*, 2000) to a high frequency end above the noise level. τ was calculated from ϵ according to the law of the wall (*Lee*, 2003; *Thorpe*, 2005).

Numerical model simulations were carried out to evaluate their performance in reproducing ϵ, TKE, and τ. Turbulence models have been developed and implemented to simulate physical dynamics in the BBL, and a recent review by *Burchard et al.* (2008) summarises details of models used to quantify turbulence in coastal oceans. Among these models, second-moment two-equation statistical turbulence closure models are most widely used, and are integrated in the general ocean turbulence model (GOTM; *Burchard et al.*, 1999; *Burchard*, 2002) used in the present study. Models applied in our study consist of two turbulence closures, $k-\epsilon$ and $k-kL$ (L is the macro length scale), and the stability functions of *Cheng et al.* (2002) and *Schumann and Gerz* (1995). The turbulence closures $k-\epsilon$ and $k-kL$ have been extensively applied and found to be successful in simulating turbulence in aquatic surface and bottom boundary layers (e.g., *Burchard and Bolding*, 2001; *Warner et al.*, 2005; *Anis and Singhal*, 2006). The stability functions of *Schumann*

and Gerz (1995) are empirical, and those of *Cheng et al.* (2002) are parameterized for second order models. *Cheng et al.* (2002) improved the Mellor-Yamada model (*Mellor and Yamada*, 1974, 1982) using more complete expressions for pressure-velocity and pressure-temperature correlations. Both sets of stability functions have been successfully applied for reproducing observations (e.g. *Burchard et al.*, 2002; *Simpson et al.*, 2002; *Burchard et al.*, 2009; *Hofmeister et al.*, 2009; *Verspecht et al.*, 2009). The two types of stability functions were integrated with the $k-\epsilon$ and $k-kL$ closures, and their effects on the simulation results were compared.

The study site and instruments are described in Section 2.2. A quality control test is applied to current data from a bottom mounted ADV, and turbulence quantities (ϵ, TKE, and τ) are then calculated from the data (Section 2.3). Meteorological and hydrographic data used to force turbulence models are described in Sections 2.4.1 and 2.4.2, respectively. Four models are implemented for turbulence simulations and their fundamental equations are introduced in Section 2.4.3. Two of the models, one combining the $k-\epsilon$ turbulence closure and the stability functions of *Cheng et al.* (2002), and the other combining the $k-kL$ turbulence closure and the stability functions of *Schumann and Gerz* (1995), are compared to estimates of ϵ, TKE, τ, and gradient Richardson number (R_i) from observations in the BBL. This is followed by statistics of the other two models with reversed combinations of turbulence closures and stability functions (Section 2.5.1). Inter-model comparisons for the four models are examined throughout the water column (Section 2.5.2), and the influence of surface fluxes on turbulence simulations in the BBL is investigated for these models (Section 2.5.3). Differences between the turbulence closures and the stability functions due to their physical assumptions are discussed in Section 2.6, and conclusions are given in Section 2.7.

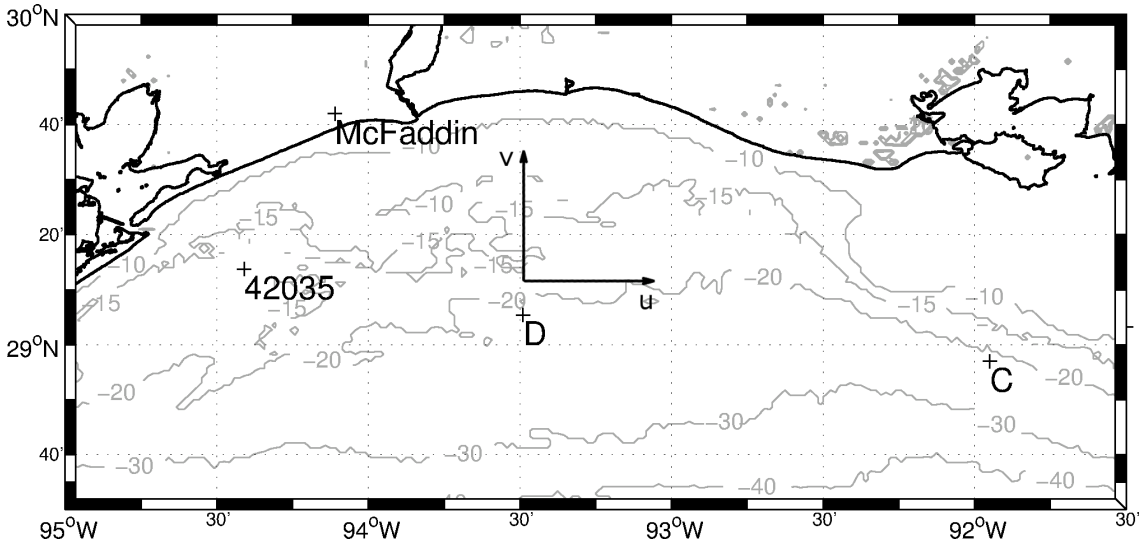

Figure 2.1: Measurements were conducted at site D on the Texas-Louisiana continental shelf. Downward shortwave radiation was observed at the weather station McFaddin. NDBC station 42035 measured wind speed, air temperature, relative humidity and air pressure, which were used for calculations of surface momentum flux, and sensible and latent fluxes. Horizontal velocities were rotated to across (u) and along (v) the principal axis of currents. Depth contours are in m.

2.2 Study site and instrumentation

A field campaign was conducted as part of the NOAA Mechanisms Controlling Hypoxia (MCH) project from August 18 to 22, 2005 (for details see http://hypoxia.tamu.edu). Time is given in UTC (CDT + 5 h) in this study. A multi-instrumented pod was deployed on the sea floor at site D at a depth of 21.7 m (29°5′45″N 93°29′44″W, Figure 2.1). Instruments included an upward-looking Nortek 1 MHz Aquadopp acoustic Doppler current profiler (ADCP), a Nortek Vector ADV and an Onset® U22-001 water temperature logger (HOBO, response time 5 minutes, sampling every 30 s, Figure 2.2b). The ADCP was set to sample current profiles every 6 minutes with vertical cell size of 0.4 m starting at 1.24 m above the bottom. The ADV measured three-dimensional velocities 0.93 m above the bottom in burst mode,

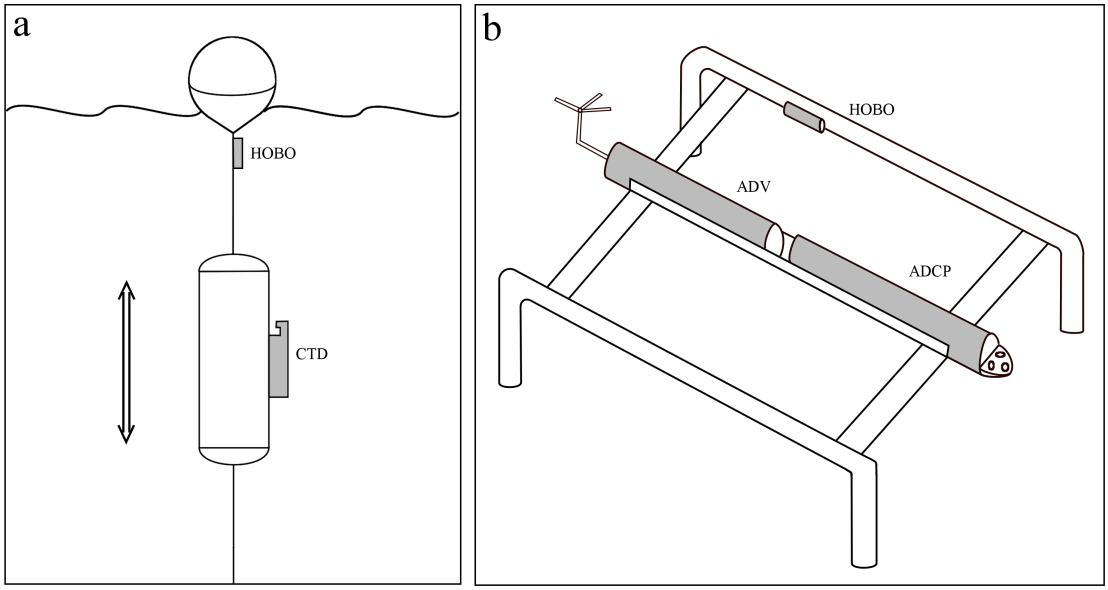

Figure 2.2: (a) a CTD was attached to the WireWalker, and a HOBO temperature logger was attached to the mooring wire beneath the surface buoy; (b) a bottom mount was instrumented with an ADV, an ADCP, and a HOBO temperature logger.

with 2048 samples per burst taken every 180 s at a sampling rate of 32 Hz (thus, the duration of each burst was 64 s). Velocity measurements were orientated to along (v) and across (u) the principal axis of ADV measured currents (Figure 2.3; *Emery and Thomson*, 2001) that was 4° counter-clockwise from North(Figure 2.1). Temperature measurements from the bottom HOBO were compared to those from the ADV's thermistor (response time 10 minutes, sampling rate 1 Hz), and were found to be in good agreement. Temperature and salinity profiles were measured by a RBR XR-620 conductivity, temperature, and depth instrument (CTD) at 1 Hz. The CTD sensor was mounted at the center of a surface-wave powered profiling vehicle (WireWalker; Figure 2.2a; *Rainville and Pinkel* 2001).

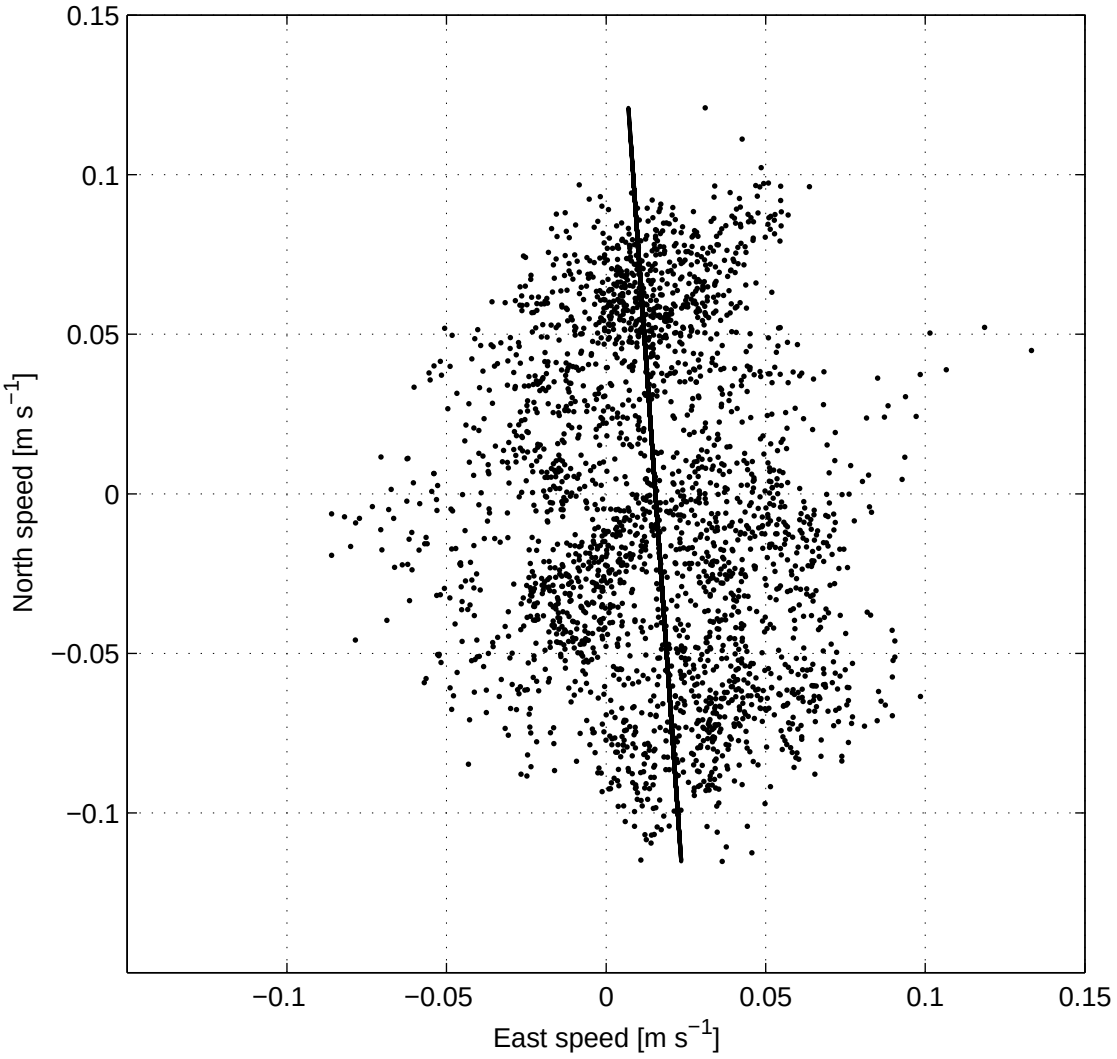

Figure 2.3: Scatter plot of ADV mean velocities. The linear fit was 4° from the North.

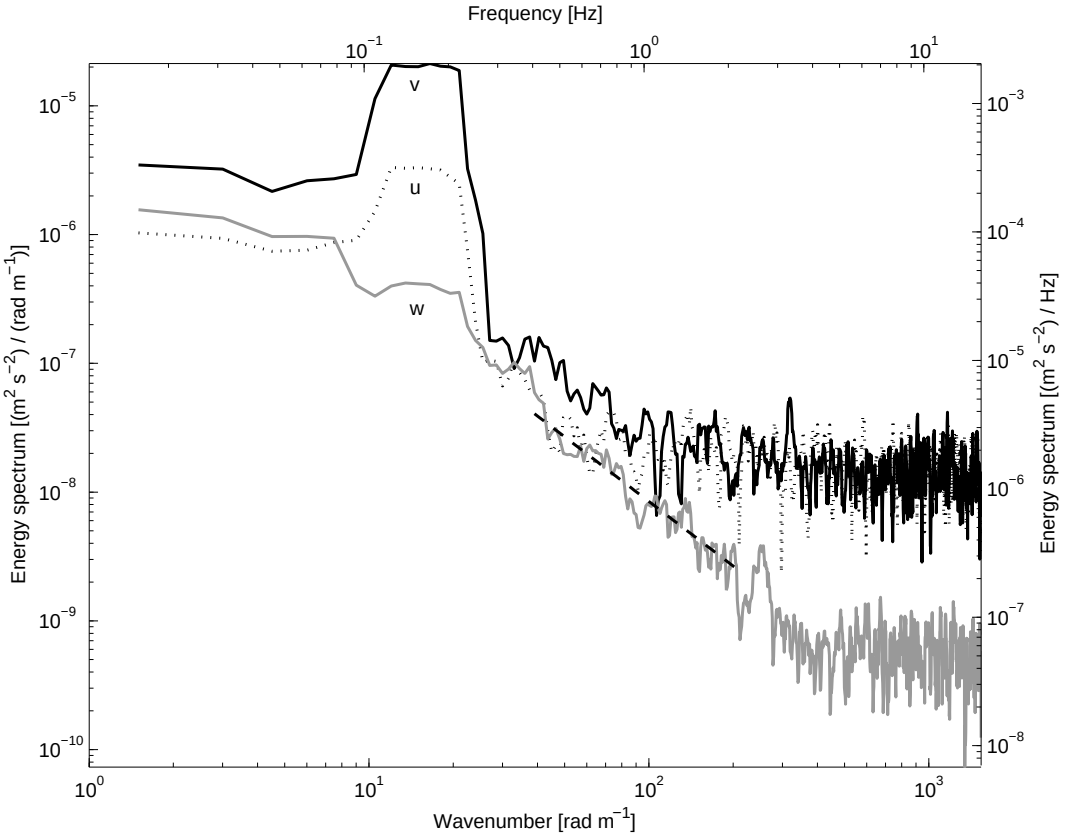

Figure 2.4: Energy spectra of an ADV burst measurement (2048 samples) of u (dotted), v (black), and w (gray) velocity components as a function of wavenumber (left and bottom axes) and frequency (right and top axes). A -5/3 slope (dashed) is drawn in the inertial subrange for reference. The mean horizontal current speed was 0.07 m s^{-1} and the measurements were taken on Aug. 21 9:18.

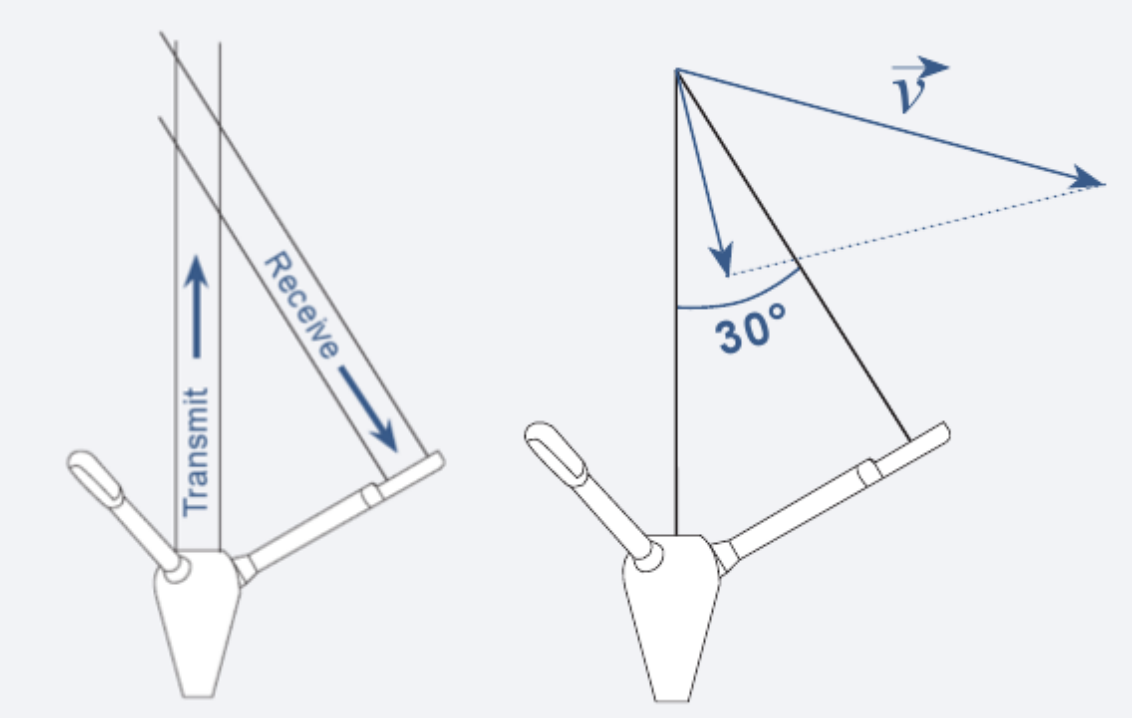

Figure 2.5: The ADV velocity is measured in the direction (15 ° from the transmitting beam) of the angular bisector between transmitting and receiving beams. The vertical component of velocity is closer to the transmitter than the horizontal components, so that the vertical velocity has less uncertainty (Vector Current Meter User Manual, Nortek).

2.3 Observational approach

High sampling rate velocity measurements from the ADV were used for estimation of turbulence quantities. ϵ was calculated from the vertical current velocity fluctuations, w', after applying the Reynolds decomposition (*Tennekes and Lumley*, 1972; *Kundu and Cohen*, 2008). Quality control of the ADV measurements was performed as follows: bursts were rejected if beam velocity correlations $\leq 70\%$ (Vector Current Meter User Manual, Nortek); burst-averaged vertical velocities were required to be < 0.01m s^{-1} such that w was close to the true vertical direction (*Davis and Monismith*, 2011). Estimates of observed ϵ were based on Kolmogorov's -5/3 law (*Kolmogorov*, 1941) and a fit to the energy spectrum of velocity fluctuations in the inertial subrange (*Jonas et al.*, 2003; *Lorke and Wüest*, 2005). In the inertial subrange, the energy spectrum is expected to be a function only of ϵ and the wavenumber, k_{wn} (or frequency f), and follow a -5/3 slope in logarithmic scale:

$$E(k_{wn}) = \alpha \epsilon^{\frac{2}{3}} k_{wn}^{-\frac{5}{3}}, \tag{2.1}$$

where $E(k_{wn})$ is the energy spectrum, and $\alpha = 1.5$ is the Kolmogorov constant (*Sreenivasan*, 1995; *Pope*, 2000). An example of an energy spectrum with mean horizontal current speed 0.07 m s^{-1} is shown in Figure 2.4. White spectral noise is visible at the high k_{wn} (or f) end. Noise of the vertical component (5.23×10^{-8}m^2 s^{-2} Hz^{-1} on average) is lower than that of the horizontal components (1.44×10^{-6}m^2 s^{-2} Hz^{-1} on average). The lower noise in the vertical component is due to the geometry of the ADV transducers (Figure 2.5), with the transmitting and receiving beam pair being more sensitive to velocities in the direction of the angular bisector between the beams. Thus, with the transmitter configured in the vertical direction, the vertical velocities have a lower noise level and were used for the present work.

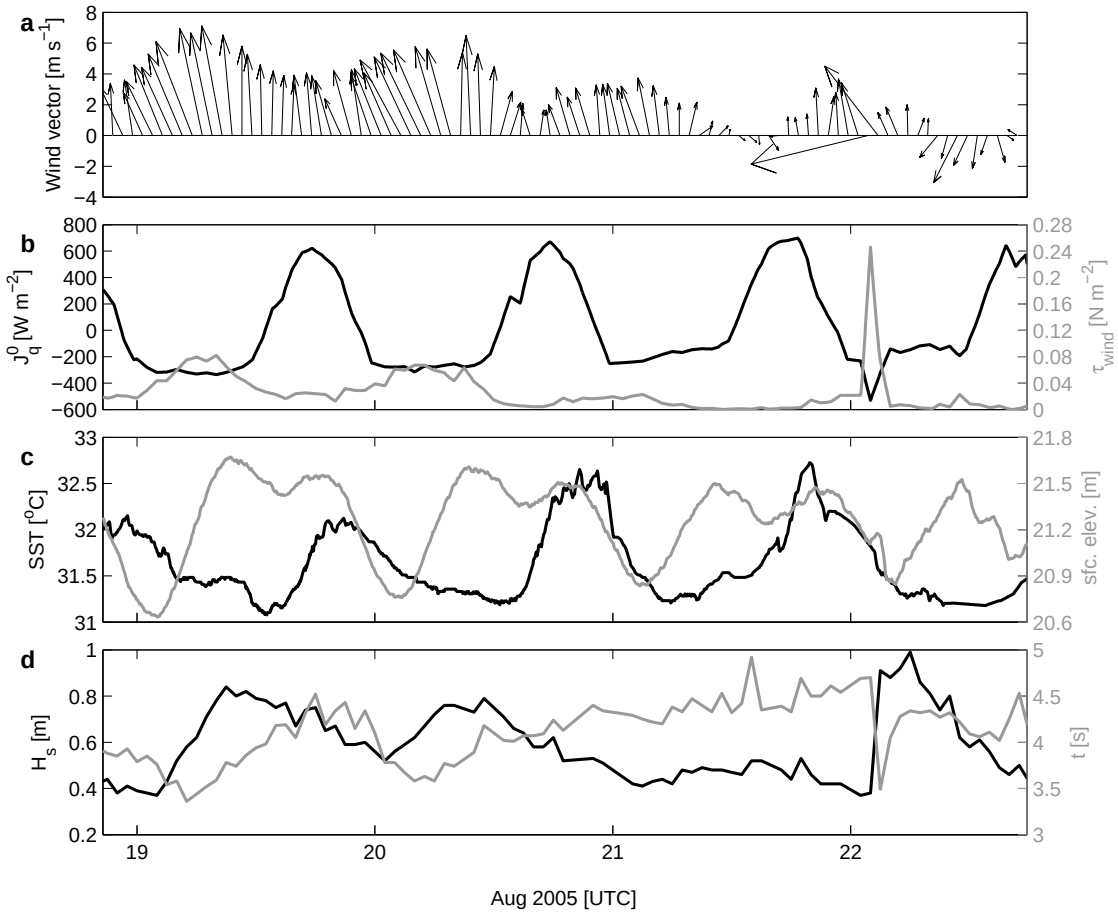

Figure 2.6: Surface meteorology: (a) hourly wind vectors; (b) net heat flux, J_q^o (black), and momentum flux, τ_{wind} (gray); (c) sea surface temperature (black), and sea-surface elevation (gray); (d) significant wave height, H_s (black), and average wave period, t (gray).

In shallow coastal waters, surface waves may create σ in the near bed region, the depth (z) in which effects of surface waves will be important is $z \leq 0.16gt^2$ (*Baumert et al.*, 2005), where t is the wave period, and g is the gravitational acceleration. Thus, surface waves with $t > 3.6$ s may have an effect in the BBL at site D (water depth of 21 m). t was primarily longer than 3.6 s at site D (for details see Section 2.4.1 and Figure 2.6d), thus, the BBL at site D was affected by surface waves (*Davis and Monismith*, 2011), and a removal of turbulence induced by σ was carried out. The surface wave energy can be noted between 0.1 and 0.3 Hz in the energy spectra (Figure 2.4), also most likely elevated the spectra in the inertial subrange. To apply the Kolmogorov's hypothesis to the energy produced by turbulence but not by surface wave, ϵ was estimated from the equation for vertical velocity components in *Trowbridge and Elgar* (2001):

$$E_{ww}(f) = \frac{12}{55}\alpha\epsilon^{\frac{2}{3}}V^{\frac{2}{3}}f^{-\frac{5}{3}}I(\frac{\sigma}{V}, \phi) \tag{2.2}$$

where $E_{ww}(f)$ is the energy spectrum of vertical velocity fluctuations, V is the horizontal mean current, and I is the function of σ, the angle between wave and current (ϕ), and V (for the expression of I see *Trowbridge and Elgar* 2001).

Kolmogorov (1941) hypothesized that an inertial subrange in the energy spectrum exists only when energy is transferred by inertial forces while viscous forces are negligible. The existence of an inertial subrange was first examined for each burst. For instance, the energy spectra of vertical velocity fluctuations (Figure 2.4) showed an intermediate range with a slope close to -5/3. The f range was chosen from 0.3 Hz (to exclude wave domains) to a f before noise became dominant (the range represented by the dashed line). A robust regression algorithm (RR; *Chatterjee and Hadi*, 1986; *DuMouchel and O'Brien*, 1991; *Wager et al.*, 2005) was applied to

compute the slope and the 95% confidence interval. The RR minimizes the sum

$$s = \sum_{i=1}^{N} W_i (y_i - \widehat{y}_i)^2, \tag{2.3}$$

where y_i is the ordinate of the observed data point, $\widehat{y}_i$ is the ordinate of the corresponding point on the fitting line, and W_i is the weight calculated by a bi-square weighting function, assigning less weight to outliers. If -5/3 falls within the 95% confidence interval of the fitted line's slope (here [-1.73 -1.63]), an inertial subrange was considered to exist, and ϵ was estimated by applying equation (2.2). 768 out of 2356 bursts (32.6%) were found to exhibit acceptable inertial subranges, with estimated values of ϵ above 5×10^{-9} $\mathrm{m^2 s^{-3}}$.

Observed ϵ values (Figure 2.7a) were significantly affected by the current speeds in the BBL and followed their pattern consistently (Figure 2.7b). Magnitudes of the currents were mainly a function of v, given that this velocity component (0.04 m $\mathrm{s^{-1}}$ on average) generally was larger than the u component (0.02 m $\mathrm{s^{-1}}$ on average, Figure 2.7c). Ratios of σ to burst-averaged current speed, β_V, were mostly <0.5 (Figure 2.7d), indicating that surface waves had an impact near the seabed but not as significant as reported in other shallower water experiments (*Davis and Monismith*, 2011; *Hackett et al.*, 2011). To quantitatively investigate the effect of surface waves, ϵ was also estimated from equation (2.1). The regression coefficient of ϵ values calculated from equations (2.2) and (2.1) was 0.44 (Figure 2.8).

TKE is defined as

$$k = \frac{1}{2}\left(\overline{u'^2} + \overline{v'^2} + \overline{w'^2}\right), \tag{2.4}$$

where overbars denote time averages. Turbulence was assumed locally isotropic, thus

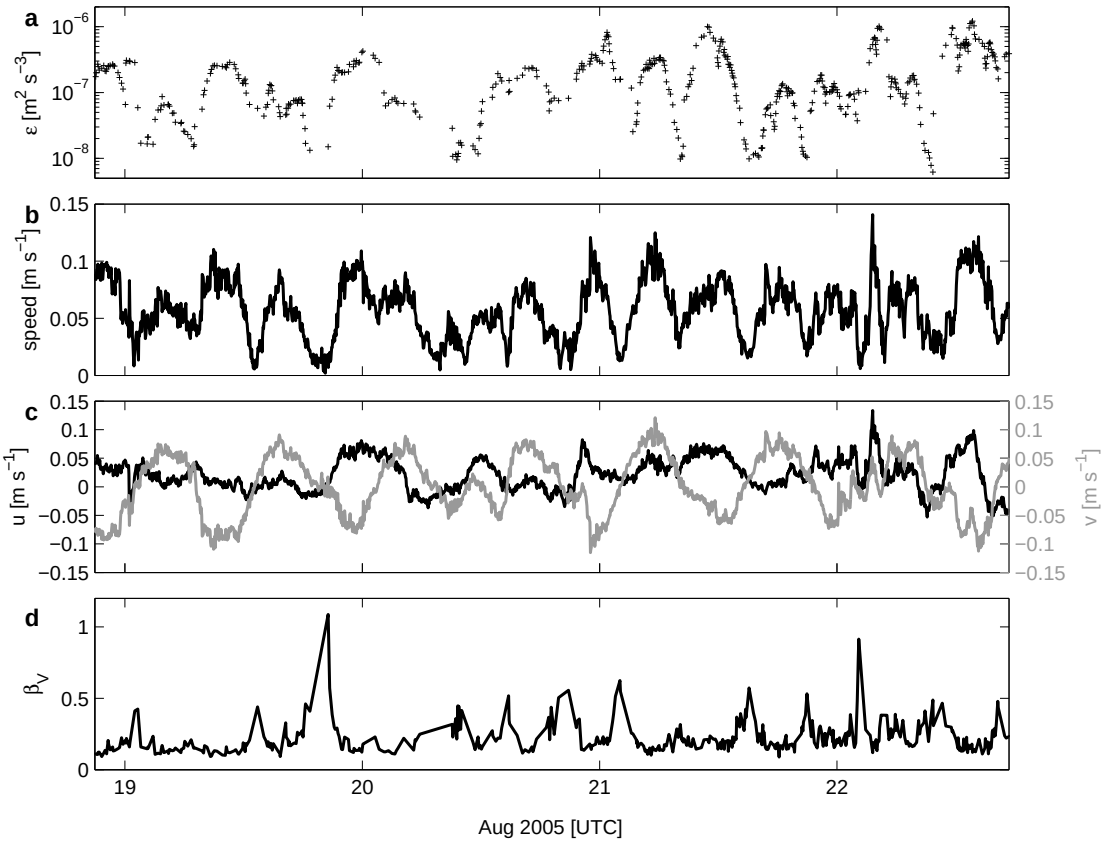

Figure 2.7: (a) ϵ estimated from observations and equation (2.2); (b) ADV measured current speed; (c) u (black), and v (gray); (d) ratio of σ to burst-averaged current speeds, β_V, in the BBL.

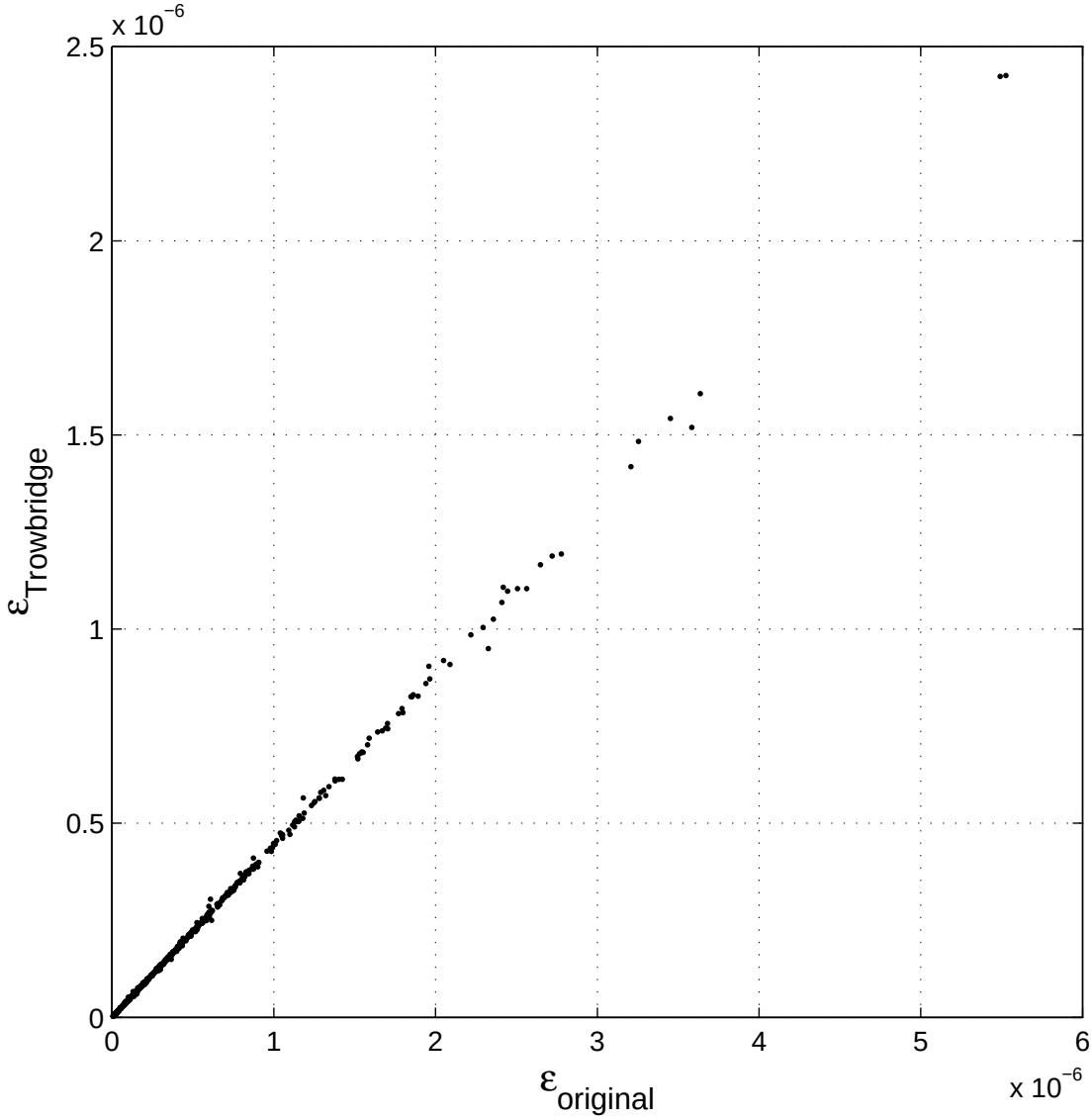

Figure 2.8: Scatter plot of ϵ values calculated from vertical velocities following the *Trowbridge and Elgar* (2001) method (equation 2.2) and the original method (equation 2.1). The slope of the linear fit is 0.44.

$\overline{u'^2}$ and $\overline{v'^2}$ were replaced by $\overline{w'^2}$:

$$k = \frac{3}{2}\overline{w'^2}. \tag{2.5}$$

$\overline{w'^2}$ was the spectral integral in the inertial subrange above the noise level. The low end of the frequency range was chosen as $1/k_{wn} = l_0/10$ ($l_0 = 0.93$ m is the height of the ADV's sampling volume above the bottom), demarcating between anisotropic large eddies and isotropic small eddies (*Pope*, 2000; *Bluteau et al.*, 2011). The high end of the frequency range was chosen where the spectrum decreased to the instrument's noise level.

Reynolds stress was estimated from the law of the wall which assumes uniform stress near the seabed (*Perlin*, 2005; *Arneborg et al.*, 2007):

$$\tau = \rho(\epsilon\kappa l_0)^{\frac{2}{3}}, \tag{2.6}$$

where $\kappa = 0.41$ is the von Kármán constant. Results of estimated ϵ, TKE and τ from the observations are further discussed in Section 2.5.

2.4 Numerical modeling approach

Models were forced with meteorological and hydrographic measurements. We describe the surface meteorology and hydrography first, and then the formulation of models is explained.

2.4.1 Surface meteorology

Meteorological data were obtained from the stations shown in Figure 2.1. Wind conditions were recorded at the National Data Buoy Center (NDBC) station 42035 (29°13′54″ N 94°24′46″ W). South winds prevailed during most of the experiment, diminishing during nighttime and increasing during daytime (Figure 2.6a). A single strong wind event was recorded at NDBC 42035 around 04:00 on Aug. 22, with wind

speeds reaching up to 14.4 m s^{-1}. This event was registered at site D as a sharp decrease of SST measured from the surface HOBO and a water pressure anomaly (reverse temporal gradient) measured from the ADV (for details see Appendix A). The momentum flux (τ_{wind}, Figure 2.6b) was calculated from wind speed and air density collected at NDBC 42035 using bulk formulae (*Large and Pond*, 1981).

The net surface heat flux, J_q^0, was computed as the sum of four components:

$$J_q^0 = J_q^{sw} + J_q^{lw} + J_q^l + J_q^s, \tag{2.7}$$

where J_q^{sw} is the net shortwave radiation, J_q^{lw} is the net longwave radiation, J_q^l is the latent heat flux due to evaporation, and J_q^s is the sensible heat flux. J_q^{sw} was calculated from measurement of incoming solar radiation at the US Forest Service weather station McFaddin (29°42′0″N 94°7′0″W; Figure 2.1), the nearest available station, using the formula in *Payne* (1972) for albedo. J_q^{lw} was computed from sea surface temperature (SST) and downward longwave radiation following *Dickey et al.* (1994). The SST measurements were from NDBC 42035 (Figure 2.6c) and were compared to those from a HOBO attached beneath a surface buoy at site D (Figure 2.2a). The average difference was 1.1%. The downward longwave radiation

	day				night			
date	19	20	21	22	19	20	21	22
τ_{wind} [Nm^{-2}]	0.027	0.012	0.006	0.005	0.057	0.053	0.011	0.034
J_q^0 [Wm^{-2}]	210.9	260.9	306.1	310.9	-306.6	-272.1	-188.8	-203.9
H_s [m]	0.70	0.58	0.46	0.53	0.56	0.66	0.45	0.75
t [s]	4.15	4.16	4.52	4.17	3.65	3.81	4.33	4.27
δ [°]	171	158	155	132	168	155	162	106

Table 2.1: Daytime and nighttime averages of momentum flux, τ_{wind}, net heat flux, J_q^0, significant wave height, H_s, average wave period, t, and mean wave direction, δ (from where waves are coming clockwise from North).

was retrieved from the National Centers for Environmental Prediction/Department of Energy Reanalysis 2 (NCEP; *Sun et al.*, 2003; *Kubota et al.*, 2008) database, and was interpolated to site D using the nearest grid points. J_q^l and J_q^s were calculated using wind speed, air temperature, relative humidity, and air pressure from the NDBC 42035 and the SST (*Fairall et al.*, 1996). J_q^0 followed a diurnal pattern (Figure 2.6b), and daytime and nighttime averages of τ_{wind} and J_q^0 are given in Table 2.1.

The sea-surface elevation (Figure 2.6c) indicates a dominant semi-diurnal tide with a range of up to 1 m during the study period. Significant wave height (H_s), t, and mean wave direction (δ) were retrieved from NDBC 42035 wave measurements (Figure 2.6d, Table 2.1). H_s ranged from 0.37 to 0.99 m, t from 3.36 to 4.92 s, and δ from 77° to 198° (from where waves are coming clockwise from North), primarily following wind directions. Daytime and nighttime averages of H_s, t, and δ are given in Table 2.1.

2.4.2 Hydrography

Hydrographic measurements are shown in Figure 2.9. Potential temperature (θ) profiles included data from the CTD, surface HOBO, and ADV measurements (Figure 2.9a). The CTD measured from near the bottom (18 m) to near the surface (1 m), but did not profile down to the seabed due to the inherent limitation of the WireWalker (Figure 2.10). To avoid data contamination from the vehicle's wake, only upward profilings were considered. BBL temperatures were measured from the bottom HOBO, ADV, and ADCP. Measurements from the bottom HOBO and ADV were similar, while those from the ADCP were 1°C higher on average (Figure 2.11). ADV's measurements were chosen because of the ADV's higher sampling rate (1 Hz) than the HOBO's (1/30 Hz) and its more robust temperature sensor than the HOBO. Salinity (S, Figure 2.9b) was measured from the CTD, and values at the

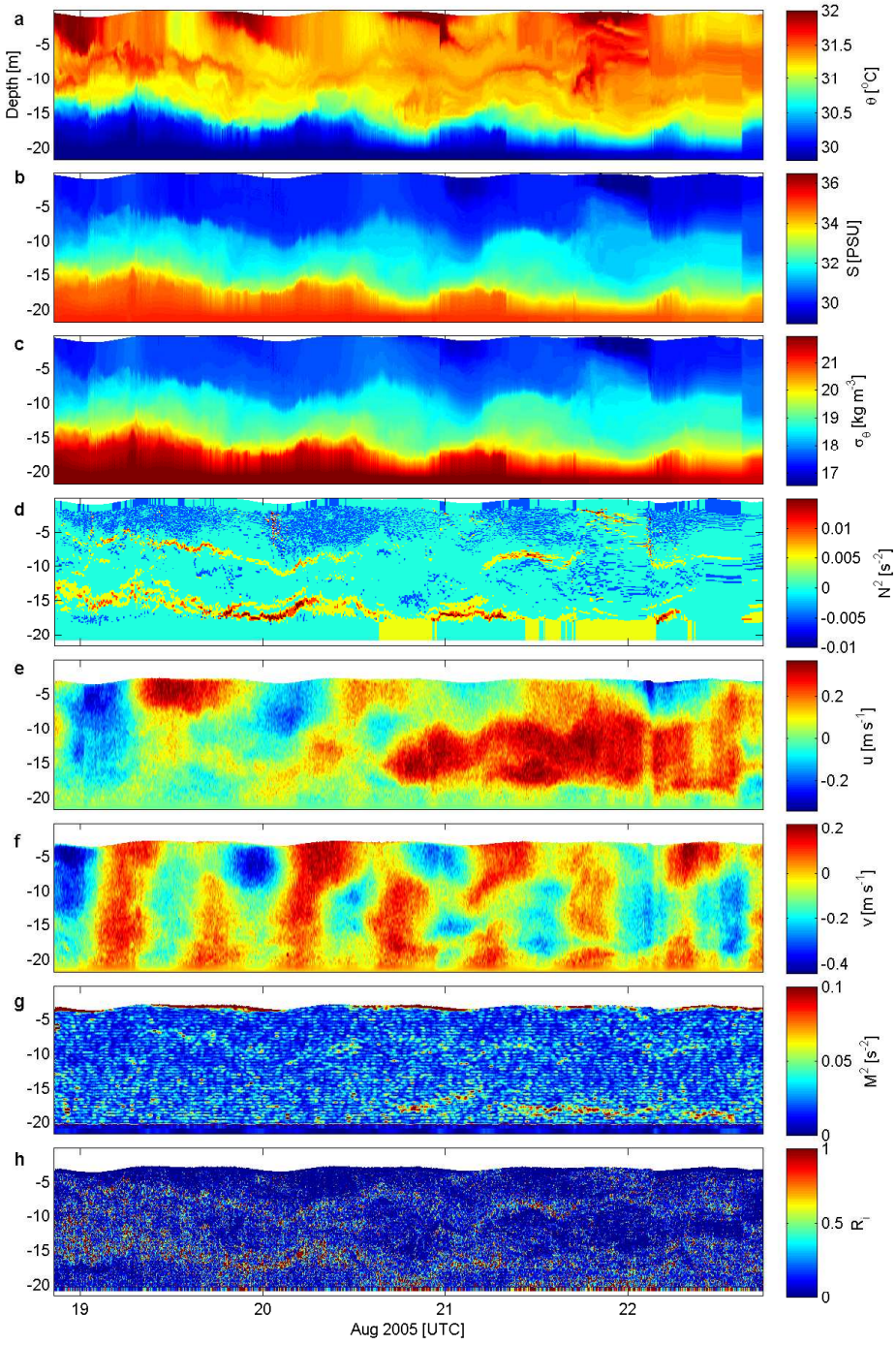

Figure 2.9: Hydrographic observations: (a) potential temperature, θ; (b) salinity, S; (c) σ_θ; (d) squared buoyancy frequency, N^2; (e) u and (f) v profiles measured by the ADCP; (g) squared shear frequency, M^2; (h) gradient Richardson number, R_i.

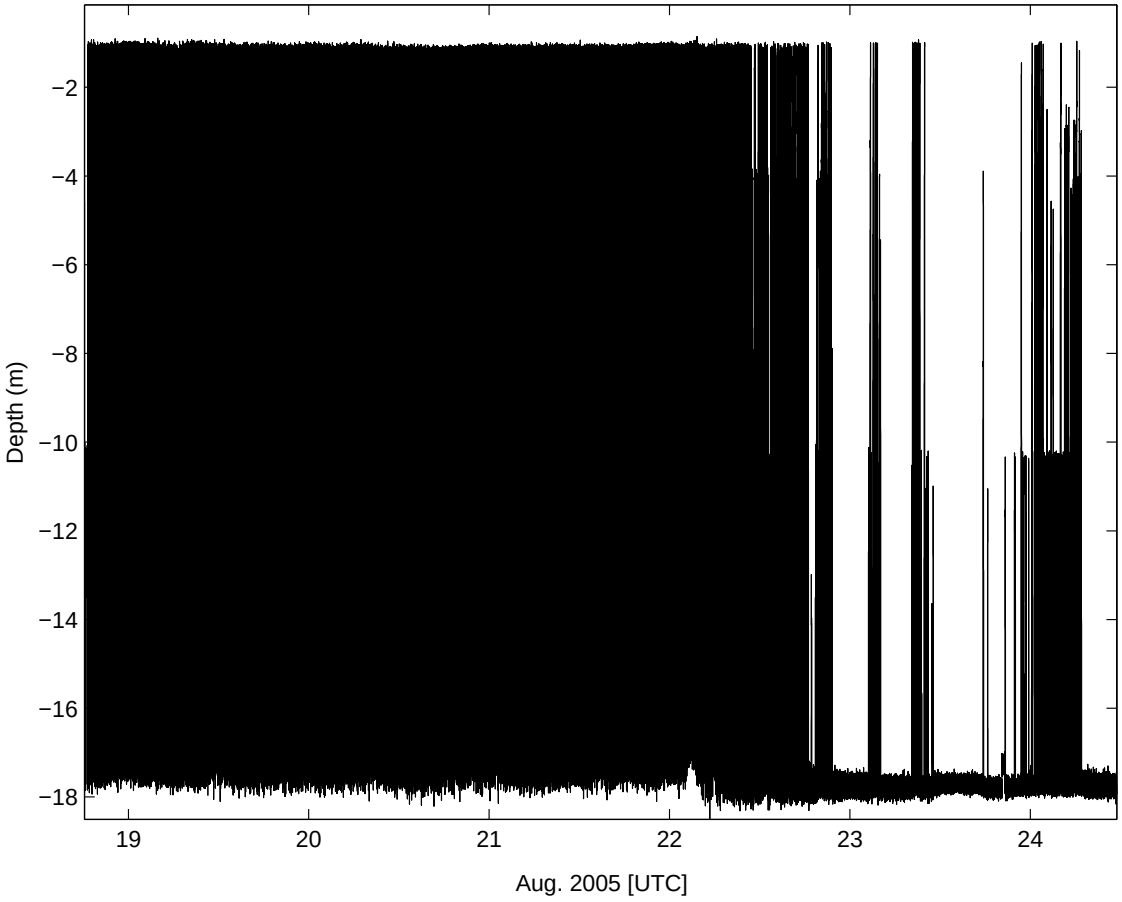

Figure 2.10: Depths of the RBR CTD. Due to calm conditions from late Aug. 22 at site D, the WireWalker suspended at certain depths.

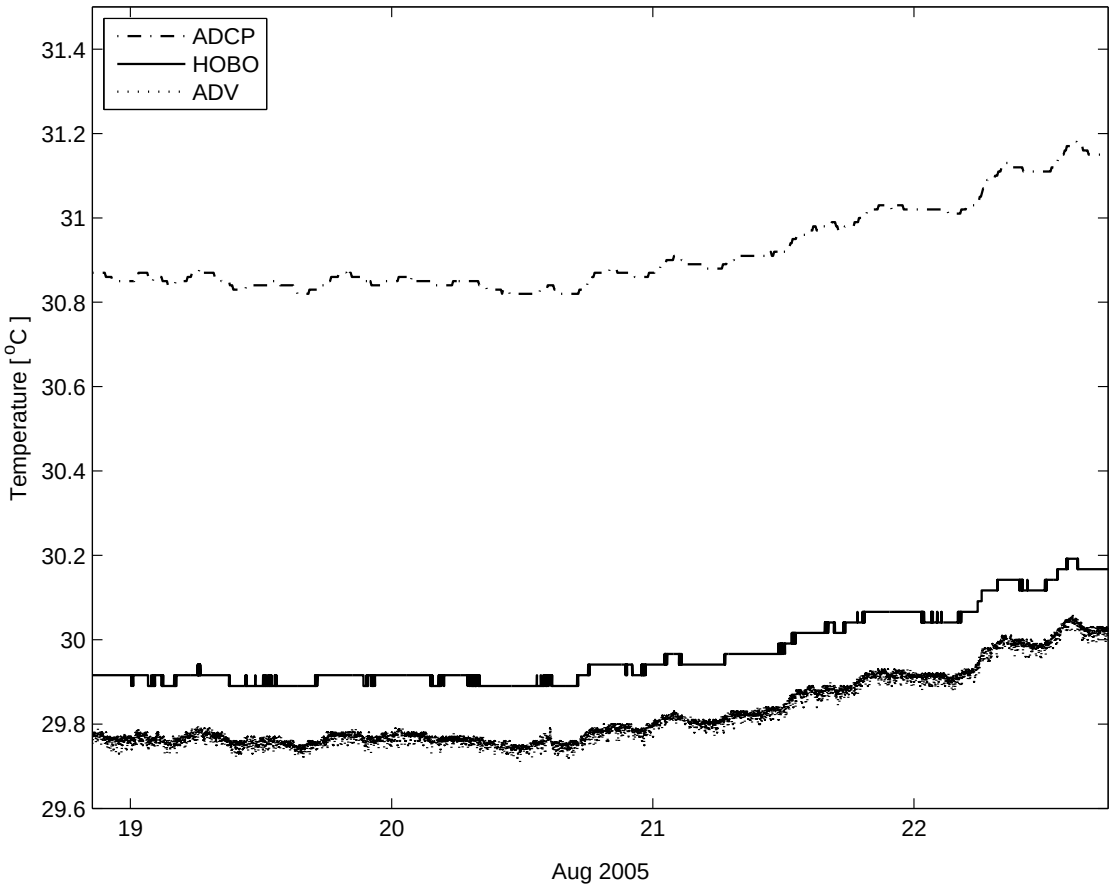

Figure 2.11: Temperature measurements from the ADCP, bottom HOBO, and ADV on the pod.

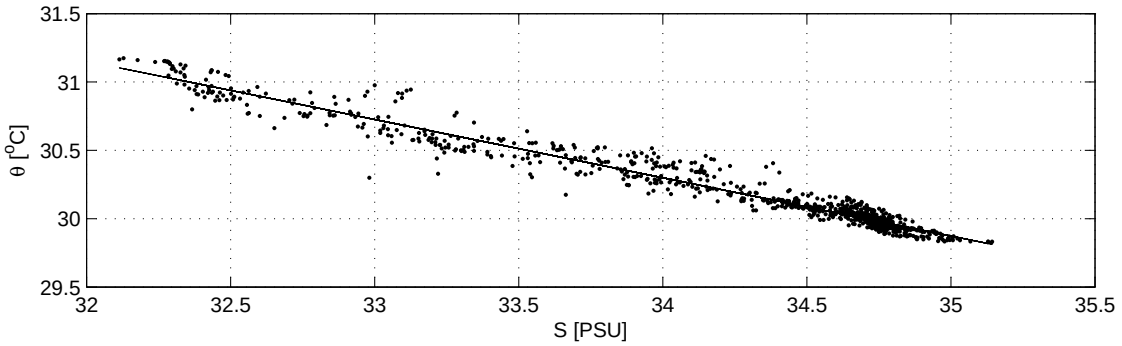

Figure 2.12: θ-S diagram of CTD measurements at the lower end of each profile. The linear fit (solid line) has a slope -0.43.

depth of the ADV were estimated according to the linear fit of the θ-S digram of CTD measurements at each lower end of the profile (Figure 2.12):

$$\theta = 44.79 - 0.43S. \tag{2.8}$$

σ_θ was then calculated throughout the water column (Figure 2.9c). Values of squared buoyancy frequency, $N^2 = -g/\rho_0 \partial_z \rho$ (ρ_0 is the mean density, and ρ is the density), indicated the presence of strongly stratified layers within the pycnocline at depths about 8 and 18 m (Figure 2.9d).

Current velocities were measured from the ADCP, from the surface to 1.24 m above the bottom, and from the ADV 0.93 m above the bottom. ADCP measurements at the lowest cell were found to be consistent in trend with those from the ADV (Figure 2.13). Near-surface measurements of the ADCP were contaminated due to sidelobe interference near the surface (Figure 2.14, *Appell et al.*, 1991; *Muste et al.*, 2004) and the upper 10% of velocity profiles were, therefore, removed from the analysis (Figure 2.9e,f). Currents changed directions concurrent with the semi-diurnal tidal cycles in the v component throughout the water column. Currents in the SBL (depths above 8 m), mid layer (8 to 19 m) and BBL (19 to 21 m) are described as follows in two periods: from late Aug. 18 to late Aug. 20 (period 1) and from late Aug. 20 to late Aug. 22 (period 2). In the SBL, the mean values of current speeds decreased from 0.17 m s^{-1} in period 1 to 0.11 m s^{-1} in period 2 for both u and v components. In the mid layer between the strongly stratified layers, the mean of u was 0.07 m s^{-1}, and the u component dominated, and the mean current speed increased to 0.2 m s^{-1}. The magnitude of mean v values remained 0.1 m s^{-1} during periods 1 and 2. In the BBL, both u and v components were low in magnitude with mean values of 0.04 m s^{-1} over the experiment, although the u component showed

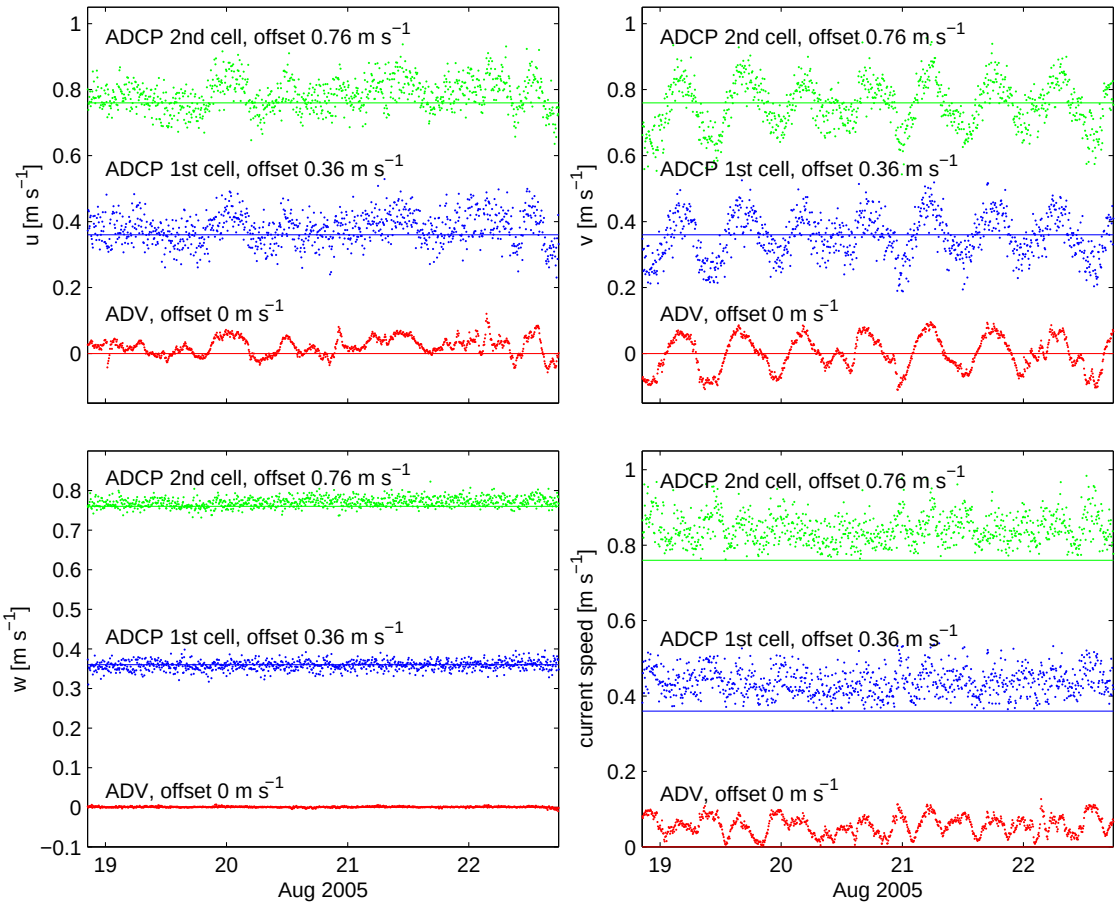

Figure 2.13: Velocity measurements from the ADV and the lowest two cells of ADCP. For clarity, the ADCP measurements were offset by 0.36 and 0.76 m s^{-1} for cells 1 and 2, respectively.

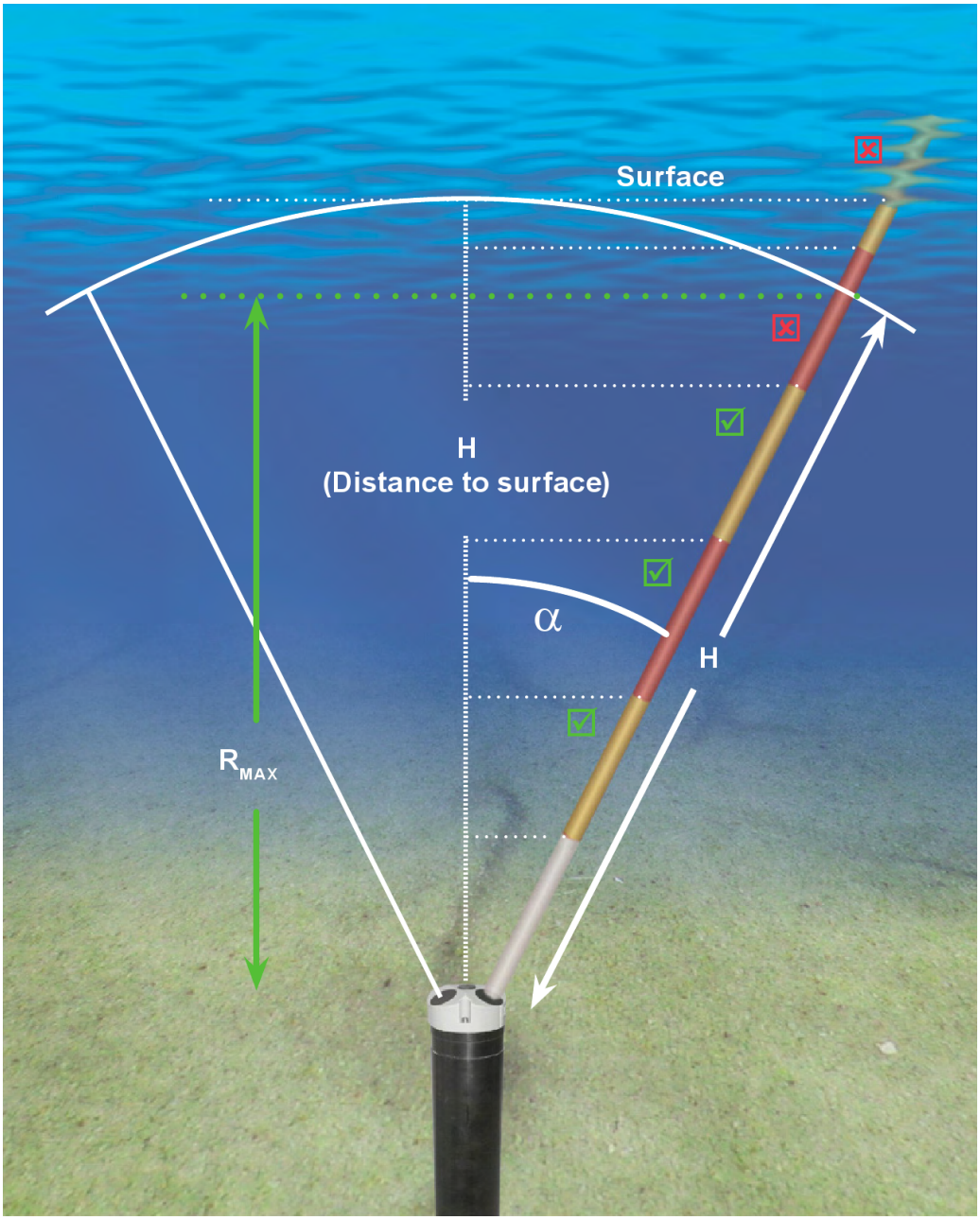

Figure 2.14: The geometry of ADCP sidelobe interference. $R_{\mathrm{MAX}} = Hcos\alpha$ is the maximum range of good data, $\alpha = 25°$ is the angle from the beam to vertical direction, hence $R_{\mathrm{MAX}} = 0.9H$. The sidelobe acoustic energy reflected by the surface contaminates the near-surface measurements. The green check marks indicate good cells, while measurements in the cells of red cross marks off R_{MAX} is rejected (Aquadopp Current Profiler User Guide, Nortek).

little temporal variability compared to the v component. Squared shear frequency, $M^2 = (\partial_z \overline{u})^2 + (\partial_z \overline{v})^2$, presented relatively high values (> 0.05 s^{-2}) where strong u currents showed high vertical gradients in period 2 (Figure 2.9g). $R_i = N^2/M^2$ primarily corresponded to N^2 (Figure 2.9h), indicating stability in the pycnocline.

2.4.3 Model formulation

Four models were applied for turbulence simulations:

- CH: the $k - \epsilon$ turbulence closure with the stability functions of *Cheng et al.* (2002)
- SG: the $k - kL$ turbulence closure with the stability functions of *Schumann and Gerz* (1995)
- CHx: the $k - kL$ turbulence closure with the stability functions of *Cheng et al.* (2002)
- SGx: the $k - \epsilon$ turbulence closure with the stability functions of *Schumann and Gerz* (1995)

Formulations of the stability functions of *Cheng et al.* (2002) and *Schumann and Gerz* (1995) are presented in Appendix B.

In the $k - \epsilon$ turbulence closure, ϵ is derived from the transport equation

$$\frac{D\epsilon}{Dt} = \Gamma_\epsilon + \frac{\epsilon}{k}\left(c_{1\epsilon}P + c_{3\epsilon}B - c_{2\epsilon}\epsilon\right), \tag{2.9}$$

where $\frac{D}{Dt}$ denotes the material derivative, Γ is the sum of the viscous and turbulent transport terms, P is the shear production, B is the buoyancy production/destruction, $c_{1\epsilon} = 1.44$, $c_{2\epsilon} = 1.92$, and $c_{3\epsilon} = 1$.

In the $k-kL$ turbulence closure, ϵ is given by

$$\epsilon = \left(c_\mu^0\right)^3 \frac{k^{\frac{3}{2}}}{L}, \tag{2.10}$$

where $c_\mu^0 = 0.5477$, and L is derived from

$$\frac{D\left(q^2 L\right)}{Dt} = \Gamma_L + L\left(E_1 P + E_3 B - E_2 F \epsilon\right), \tag{2.11}$$

where $E_1 = 1.8$, $E_2 = 1.33$, and E_3 is a function of R_i and stability functions (*Mellor and Yamada*, 1982). The wall function, F, is used to reproduce the logarithmic part of the law of the wall (*Umlauf and Burchard*, 2003), and is given by

$$F = 1 + E_2 \left(\frac{L(d_s + d_b)}{\kappa d_s d_b}\right)^2, \tag{2.12}$$

where d_s is the distance from the sea surface, and d_b is the distance from the bottom. The typical velocity scale of turbulence, q, is defined by

$$k = \frac{q^2}{2}, \tag{2.13}$$

and the transport equation for q is given by

$$\frac{D(\frac{q^2}{2})}{Dt} = \Gamma_q + P + B - \epsilon. \tag{2.14}$$

To correspond to the observed TKE calculated from equation (2.5), the modeled TKE was calculated from $\overline{w'^2}$, which is derived from

$$\frac{\overline{w'^2}}{k} = \frac{2}{3} + \frac{1}{\Psi_\epsilon}\left(\left(\frac{a_2}{3} - a_3\right) P + \frac{8}{3} a_5 B\right), \tag{2.15}$$

where $\Psi_\epsilon = 2.5\epsilon$, $a_2 = 0.016$, $a_3 = 0.432$, and $a_5 = 0.25$ for stability functions of *Cheng et al.* (2002), while the second term on the right hand side of the equation is absent for stability functions of *Schumann and Gerz* (1995), i.e. it simplifies to equation (2.5). Values of TKE were calculated from equations (2.13) and (2.14) for the $k - kL$ turbulence closure and from the transport equation

$$\frac{Dk}{Dt} = \Gamma_k + P + B - \epsilon \tag{2.16}$$

for the $k - \epsilon$ turbulence closure.

The simulated τ for the four models is given by

$$\tau = \rho\nu_t|M|, \tag{2.17}$$

where ν_t is the eddy viscosity. In the $k - \epsilon$ turbulence closure, ν_t is given by

$$\nu_t = c_\mu \frac{k^2}{\epsilon}, \tag{2.18}$$

where c_μ is the stability function in Appendix B; in the $k - kL$ turbulence closure, ν_t is given by

$$\nu_t = c_\mu k^{\frac{1}{2}} L. \tag{2.19}$$

Since one-dimensional models are generally unable to account for advective effects (*Bolding et al.*, 2002), a mechanism of "relaxing" has been implemented in which modeled values are adjusted according to the observations (*Burchard*, 1999; *Anis and Singhal*, 2006; *Burchard et al.*, 2006; *Peters and Baumert*, 2007; *Cabrillo et al.*, 2011). In our simulations, models were relaxed to observed u and v profiles every 4000 s, and θ and S profiles every 360 s. Examinations of several relaxation times and

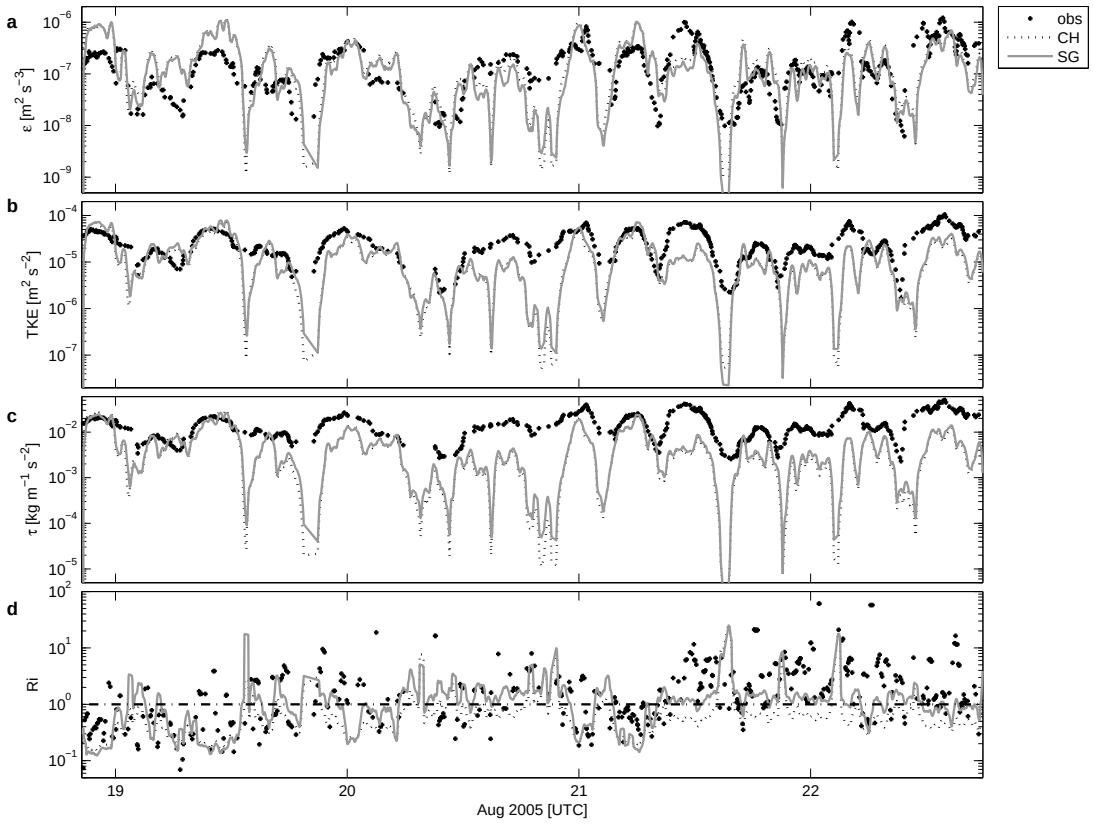

Figure 2.15: Comparisons of turbulence quantities computed from observations to those from the CH and SG models in the BBL: (a) ϵ, (b) TKE, (c) τ, and (d) R_i ($R_i^c = 1$ is indicated by a horizontal dash-dot line).

the relationship between mean simulated ϵ values and relaxation times are further discussed in Appendix C.

2.5 Analysis

ϵ, TKE, τ, and R_i from observations and models in the BBL are compared in Section 2.5.1. Comparisons between the four models throughout the water column are discussed in Section 2.5.2.

		min	max	mean [95%CI]
ϵ [m^2 s^{-3}]	obs	5.99e-9	1.21e-6	1.87e-7 [1.75e-7 2.02e-7]
	CH	1.20e-8	1.18e-6	2.41e-7 [2.30e-7 2.53e-7]
	SG	8.19e-9	1.10e-6	2.10e-7 [1.99e-7 2.21e-7]
TKE [m^2 s^{-2}]	obs	1.45e-6	1.12e-4	2.91e-5 [2.76e-5 3.06e-5]
	CH	1.43e-6	7.35e-5	1.63e-5 [1.57e-5 1.71e-5]
	SG	1.34e-6	7.87e-5	1.81e-5 [1.74e-5 1.90e-5]
τ [kg m^{-1} s^{-2}]	obs	1.96e-3	5.04e-2	1.51e-2 [1.44e-2 1.59e-2]
	CH	3.05e-4	3.13e-2	6.09e-3 [5.77e-3 6.38e-3]
	SG	3.86e-4	2.65e-2	6.10e-3 [5.84e-3 6.40e-3]
R_i	obs	4.62e-2	61.05	3.00 [2.73 3.36]
	CH	1.51e-1	2.79	0.53 [0.52 0.55]
	SG	1.23e-1	6.71	1.03 [1.00 1.06]

Table 2.2: Minima, maxima, mean values, and 95% confidence intervals for ϵ, TKE, τ, and R_i for the observations, and the CH and SG models. Simulated TKE values less than 1.5 times vertical noise energies were discarded according to equation (2.5), and the corresponding points were removed for other modeled quantities as well.

2.5.1 Observation-model comparisons in the BBL

Turbulence quantities (ϵ, TKE, and τ) and R_i from the observations and the CH and SG models are shown in Figure 2.15. Simulation results of the CH and SG models were nearly identical such that the lines of the models were primarily superimposed. The trends of modeled ϵ and TKE followed those observed, however, there were occasions when model values were much low. In most of these cases, the power spectrum was consistently lacking a clear inertial subrange, so that the Kolmogorov's hypothesis could not be applied and ϵ was not estimated. In particular, the simulated τ was substantially lower than the measured τ.

For their statistics (Table 2.2), values of vertical noise energy (9.53×10^{-7} m^2 s^{-2} on average) in all bursts were interpolated to time points of simulations, and any simulated TKE value, according to equation (2.5), less than 1.5$\times$ the corresponding vertical noise energy in each burst was discarded. Values of simulated ϵ, τ, and R_i at

	corr(obs, CH) [95%CI]	corr(obs, SG) [95%CI]	corr(CH, SG) [95%CI]
ϵ	0.31 [0.24 0.38]	0.33 [0.25 0.40]	0.99 [0.99 0.99]
TKE	0.48 [0.41 0.53]	0.48 [0.43 0.53]	0.99 [0.99 1.00]
τ	0.36 [0.31 0.42]	0.32 [0.25 0.37]	0.99 [0.99 0.99]

Table 2.3: Cross-correlations and 95% confidence intervals between the observations and the CH and SG models for ϵ, TKE, and τ.

the same time point were filtered out accordingly as well. Minimal, maximal, mean values, and their 95% confidence intervals for ϵ, TKE, and τ from the two models were similar to those from observations.

Mean R_i values computed from the observations were similar to those from the CH and SG models. A flow is commonly considered stable if R_i is greater than a critical gradient Richardson number (R_i^c). Although there is no unique value for R_i^c, in laboratory and field work, estimates of R_i^c are on the order of 1 (*Gerz et al.*, 1989; *Jacobitz et al.*, 1997; *Kundu and Cohen*, 2008). Here, 42% of the observed R_i values were found to be less than $R_i^c = 1$, compared to 43% for those computed from the CH model, and 84% for those computed from the SG model. Turbulence in the BBL was active most of the time. During stable conditions in the BBL, e.g., when values of observed R_i >5, model predicted R_i values deviated from the observations, indicating that the models may inaccurately predict the evolution of turbulence under such stable conditions (*Baker and Gibson*, 1987; *Burchard et al.*, 2002).

Model simulated values of ϵ, TKE, and τ were linearly interpolated to time of the observed estimations, and scatter plots of observed and modeled values are presented in Figure 2.16 together with linear fits (calculated using the RR). All slopes of the linear fits were <1 due to the general lower values from model simulations. Differences between the CH and SG model simulations were within a factor of 2.

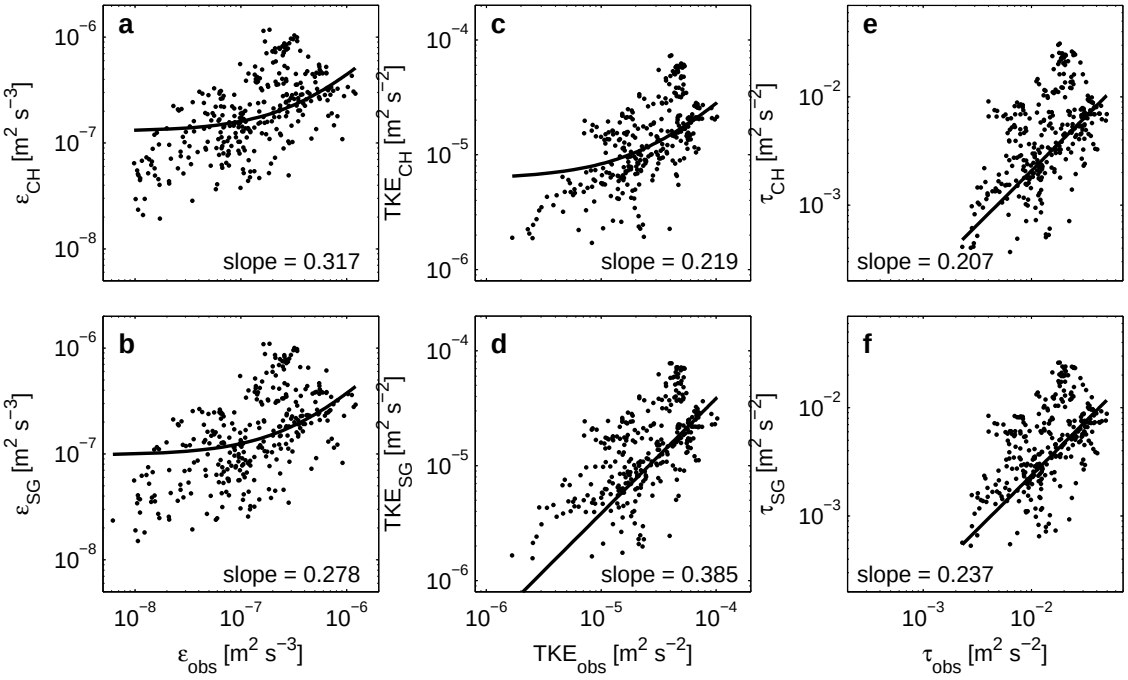

Figure 2.16: Scatter plots (log scales) for the observations (abscissas) and the CH and SG models (ordinates) for ϵ (a, b), TKE (c, d), and τ (e, f). Linear fits were calculated using the RR and are represented by the solid lines.

		min	max	mean [95%CI]
ϵ [m^2 s^{-3}]	CHx	1.44e-8	1.95e-6	4.10e-7 [3.90e-7 4.29e-7]
	SGx	9.71e-9	1.19e-6	2.36e-7 [2.24e-7 2.48e-7]
TKE [m^2 s^{-2}]	CHx	1.48e-6	1.86e-4	3.47e-5 [3.30e-5 3.66e-5]
	SGx	1.27e-6	1.02e-4	2.19e-5 [2.09e-5 2.29e-5]
τ [kg m^{-1} s^{-2}]	CHx	1.46e-4	8.49e-2	1.39e-2 [1.32e-2 1.47e-2]
	SGx	3.70e-4	3.48e-2	7.30e-3 [6.95e-3 7.66e-3]
R_i	CHx	1.68e-1	11.44	0.66 [0.64 0.69]
	SGx	1.42e-1	6.70	1.14 [1.10 1.18]

Table 2.4: Minima, maxima, and mean values with 95% confidence intervals for ϵ, TKE, τ, and R_i for the cross-combined models CHx and SGx. Simulated TKE values less than 1.5 times vertical noise energies were discarded according to equation (2.5). Corresponding points were removed for other modeled quantities as well.

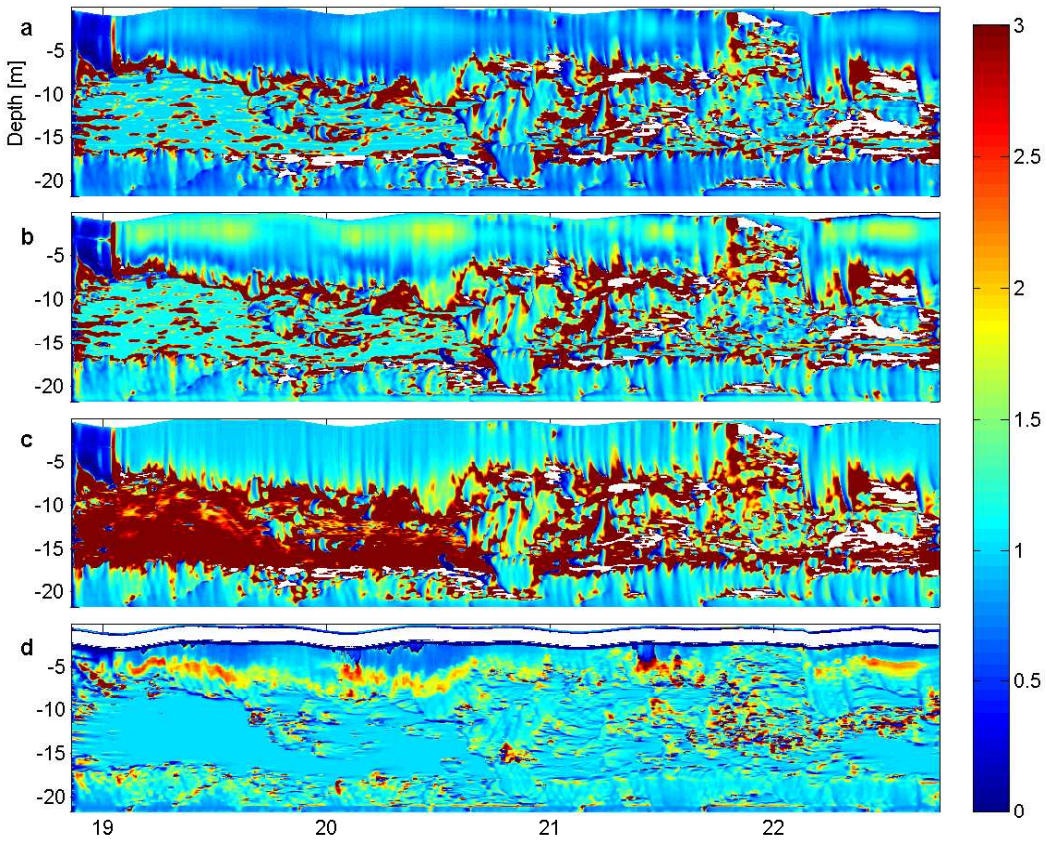

Figure 2.17: Ratios of SG model values to CH model values for (a) TKE obtained from transport equations (2.14) and (2.16), (b) ϵ, (c) τ, and (d) R_i.

Cross-correlations between the observed and modeled values were all above 46% (Table 2.3). Not surprisingly, the CH and SG models correlated highly for any quantity ($\sim 98\%$), given that the models consistently predicted similar trends. Statistics of the cross-combined models (CHx and SGx) were similar to those of the CH and SG models (Table 2.4).

2.5.2 Inter-model comparisons throughout the water column

Comparisons between the CH, SG, CHx, and SGx models were made throughout the water column. Here, calculations of TKE were not restricted to the vertical

velocity component in equation (2.5). Instead, they were simulated from transport equations (2.14) and (2.16) for the $k-kL$ and $k-\epsilon$ turbulence closures, respectively. Values are equivalent to those given by equation (2.4) in which $\overline{u'^2}$, $\overline{v'^2}$, and $\overline{w'^2}$ were taken into account. Ratios of TKE, ϵ, τ, and R_i from the SG to CH models are shown in Figure 2.17. The two models agreed well in the SBL and BBL, but the SG model estimated turbulence quantities greater values than the CH model in the pycnocline, particularly for τ that exhibited ratios >3 (Figure 2.17c).

Parameters on the right hand sides of TKE transport equations (2.14) and (2.16) are compared in Figure 2.18. The sum of shear and buoyancy production rates $(P+B)$ is close to TKE dissipation rate (ϵ), such that:

$$\frac{\Gamma}{P+B-\epsilon} \gg 1. \tag{2.20}$$

where Γ represents Γ_q in equation (2.14) and Γ represents Γ_k in equation (2.16). Thus, Γ is the main factor determining the rate of change in TKE transport equations (2.14) and (2.16) denoted as Γ_q and Γ_k, respectively. Ratios (Γ_q/Γ_k) in Figure 2.18a showed similar patterns to those for TKE in Figure 2.17a. P and B are given by

$$P = \nu_t M^2 \tag{2.21}$$

and

$$B = -\nu_t' N^2, \tag{2.22}$$

where ν_t' is the eddy diffusivity. Both P (Figure 2.18b) and B (Figure 2.18c) values in the pycnocline were estimated to be greater in the SG model, because ν_t (Figure 2.18d) and ν_t' (Figure 2.18e) were overestimated, showing ratios higher than 1, while ratios of M^2 (Figure 2.18f) and N^2 (Figure 2.18g) were ∼1.

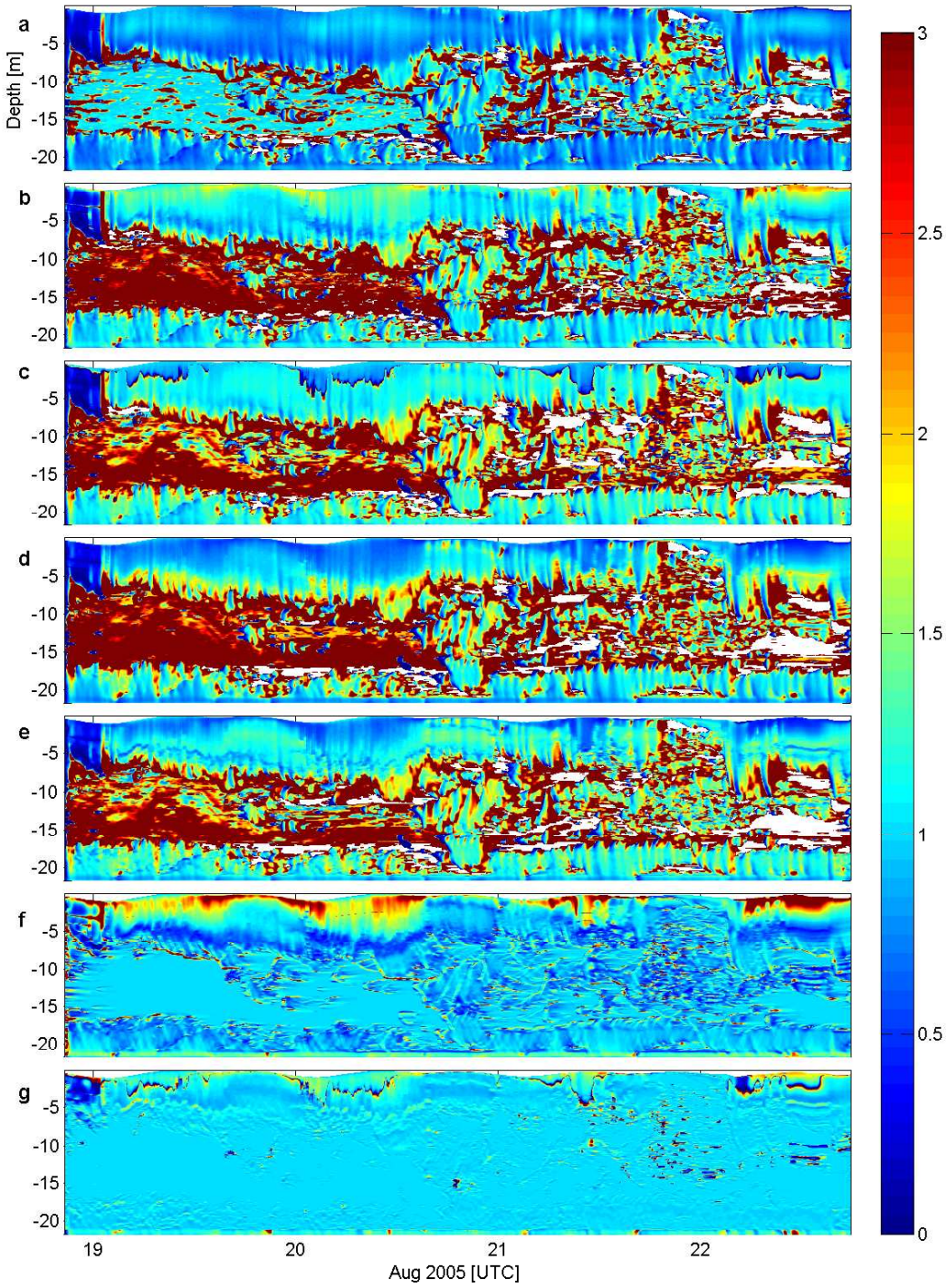

Figure 2.18: Ratios of SG model values to CH model values for (a) Γ_q/Γ_k, (b) P, (c) B, (d) ν_t, (e) ν_t', (f) M^2, and (g) N^2.

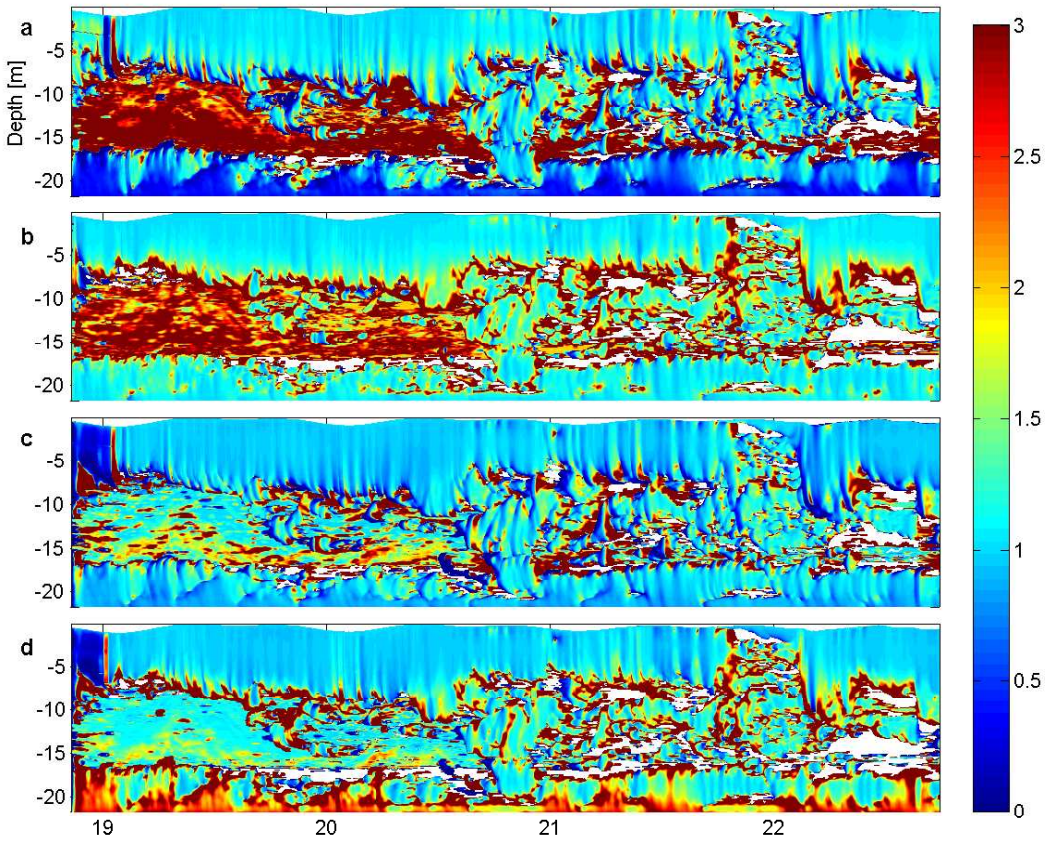

Figure 2.19: Ratios of τ values between the models: (a) SG/CHx; (b) SGx/CH; (c) SG/SGx; (d) CHx/CH.

It is not clear whether the turbulence closures or the stability functions were responsible for the differences in the pycnocline between the models results. To investigate this further, the turbulence closures and the stability functions were cross-combined for the CHx and SGx models. Figures 2.19a and 2.19b indicate that for the same turbulence closures, the stability functions of *Schumann and Gerz* (1995) resulted in higher τ values ($\tau_{\mathrm{SG}} > \tau_{\mathrm{CHx}}$ and $\tau_{\mathrm{SGx}} > \tau_{\mathrm{CH}}$); Figures 2.19c and 2.19d indicated that for same stability functions, either the $k-\epsilon$ or $k-kL$ turbulence closure resulted in similar τ values ($\tau_{\mathrm{SG}} \approx \tau_{\mathrm{SGx}}$ and $\tau_{\mathrm{CHx}} \approx \tau_{\mathrm{CH}}$). Thus differences between the four models appear to be mainly caused by the stability function. This is suggested from equations (2.17), (2.18), and (2.19) that c_μ is the main factor for τ.

2.5.3 Influence of surface fluxes on turbulence in the BBL

Stratification was prevalent during the experiment, it suppressed vertical mixing. The strong wind event at site D deepened the mixed layer (Figure 2.9a, b, c), e.g. the depth of $\sigma_\theta = 18$ kg m^{-3} was deepened 1.88 m in 87 minutes after 02:00, and was forceful enough to affect BBL currents, resulting in the maximum of observed current magnitude (Figure 2.7b) and a consequent increase in ϵ values. To investigate the influence of surface meteorological forcing on the dynamics in the BBL, the four models were run without the input of surface heat and momentum fluxes. These simulations revealed that mixing was effectively damped in the SBL, however, turbulence dynamics did not change in the BBL most likely due to the strong stratification in the pycnocline except that the BBL current velocity increases induced by the strong wind vanished.

2.6 Discussion

The simplified stability functions of *Schumann and Gerz* (1995) were found to be as capable as those of *Cheng et al.* (2002) for modeling turbulence in the BBL in our study, but deviated for c_μ related quantities, e.g. τ, P, B, ν_t, and ν_t', in the pycnocline. We found no other comparisons of the stability functions of *Schumann and Gerz* (1995) to those of *Cheng et al.* (2002) in the literature. However, there are studies between the stability functions of *Schumann and Gerz* (1995) and other stability functions, e.g. those of *Canuto et al.* (2001), which can be found in e.g. *Burchard et al.* (2002) and *Simpson et al.* (2002). *Canuto et al.* (2001) improved the Mellor-Yamada model with a down-gradient approximation for third-moments. We tested models with the stability functions of *Canuto et al.* (2001), and the results (not shown) presented minor differences from the models applying the stability functions of *Cheng et al.* (2002). Applications of the stability functions of *Canuto et al.* (2001) are described as follows, from which we try to explain the discrepancy between the stability functions of *Cheng et al.* (2002) and *Schumann and Gerz* (1995).

Burchard et al. (2002) tested the $k-\epsilon$ turbulence closure with the stability functions of *Canuto et al.* (2001) and *Schumann and Gerz* (1995) throughout a water column with a depth of 110 m. Results of their two models were found to be similar, and both agreed with observations when the water was stably stratified. In an area strongly influenced by horizontal temperature and salinity gradients, tidal straining, and vertical mixing, *Simpson et al.* (2002) applied two models by combining the $k-\epsilon$ turbulence closure with the stability functions of *Canuto et al.* (2001) and *Schumann and Gerz* (1995), respectively, throughout a water column with a depth of 35 m. Results from the former model agreed well with those from observations, while the latter model predicted a lower ϵ maximum. From the two studies above,

it appears that the comparison results are not consistent under different scenarios, however, the stability functions of *Schumann and Gerz* (1995) have less dependence on buoyancy through a constant and the turbulent Prandtl number (*Simpson et al.*, 2002), which might yield inconsistency to complex stability functions e.g. of *Cheng et al.* (2002), especially in the pycnocline. The simulations in *Peters and Baumert* (2007) also indicated that the stability functions of *Schumann and Gerz* (1995) were not able to simulate observed turbulence in stably stratified flows.

Several studies have shown that all length scale related equations perform equivalently for stress-dominated boundary layer flows when properly calibrated (e.g., *Burchard et al.*, 1998; *Baumert and Peters*, 2000; *Burchard*, 2001a). Applying steady-state Richardson numbers to B by *Burchard* (2001a) for the $k-kL$ turbulence closure and by *Burchard and Baumert* (1995) for the $k-\epsilon$ turbulence closure gave equivalent results. In full-equilibrium flows ($\frac{D}{Dt} = 0$), the $k - kL$ and $k - \epsilon$ turbulence closures were found to be interchangeable by setting $c_{\epsilon 3} = 1$ in equation (2.9) without any loss of generality (*Baumert and Peters*, 2000). However, the study of *Burchard et al.* (1998) showed that two-equation models are more sensitive to the choice of stability functions than turbulence closures. This is consistent with the present study's findings.

2.7 Conclusions

The water column on the Texas-Louisiana continental shelf was strongly stratified and wind speeds were moderate most of the time. Surface heat and momentum fluxes were found to have little effect on turbulence in the BBL, with the pycnocline effectively suppressing vertical mixing, and inhibiting transport of waterborne constituents such as nutrients, oxygen, etc. A single, short, strong wind event deepened the mixed layer and affected currents in the BBL. This resulted in the u in the

BBL reaching a maximum during the wind event. Turbulence was not active near the bottom over the experiment, with only 32.6% burst measurements presented a clear inertial subrange in energy spectra of vertical velocity fluctuations. Turbulence quantities (ϵ, TKE, and τ) in the BBL were studied using observational and modeling methods, and meteorological data from various sources near and at the study site were obtained for model simulations.

Vertical velocities measured from the ADV were applied to estimate ϵ, TKE, and τ due to the lower noise level of the vertical component compared to the horizontal components, as well as the less impact of surface wave induced motions in the vertical direction than in the horizontal directions. Observed ϵ values were estimated in inertial subranges of energy spectra following Kolmogorov's -5/3 law with the removal of surface wave effect introduced by *Trowbridge and Elgar* (2001). ϵ values from this method were lower than those from the original energy spectrum equation (2.1) with a factor 0.44. Magnitudes of observed ϵ were strongly affected by v, following the trend of velocity magnitudes in the BBL. Observed TKE values were calculated by integrating spectra under the logarithmic fits in inertial subranges, and observed τ values were calculated from the ϵ estimates according to the law of the wall.

Four numerical models (CH, SG, CHx, and SGx) were applied for turbulence simulations in the BBL, using combinations of turbulence closures ($k-\epsilon$ and $k-kL$) and stability functions (*Cheng et al.*, 2002 and *Schumann and Gerz*, 1995). The models were relaxed to θ, S, u, and v measurements, correcting advection to these quantities. The trends of ϵ, TKE, and τ for the four models were consistent with observations, and their mean values were similar to those observed. After comparing the measurements at another mooring site with a similar water depth, as well as the verification by the observation-model comparisons, it was suggested that the assumption of homogeneous salinity in the BBL was appropriate. Modeled TKE

values were computed using two methods: 1) equation (2.5) and modeled vertical velocity variances for observation-model comparisons; 2) transport equations (2.14) and (2.16) for inter-model comparisons. Results from both methods showed similar TKE values between the SG and CH models in the BBL. Analyses of each parameter on the right hand side of the transport equations revealed that Γ was the major factor to the temporal variability of TKE. The CH, SG, CHx, and SGx models performed analogously in the BBL, while differences between the models in the pycnocline were found to be primarily caused by the stability functions rather than the turbulence closures.

Although second-moment two-equation statistical turbulence closure models have been widely used for comparisons in the entire water column, a relatively small number of studies have been carried out at specific depth intervals (*Burchard et al.*, 2002; *Wang et al.*, 2011). The present study provides new insight on the turbulence dynamics in the BBL and the applicability of turbulence models to simulate the dynamics in these layers on the continental shelf.

3. OBSERVATIONS AND MODEL SIMULATIONS OF TURBULENCE IN A HYPOXIC ZONE WITH THE ADVECTION OF NON-LOCAL WATER

3.1 Introduction

A field campaign was conducted on the continental shelf of the Gulf of Mexico in the summer of 2005 when hypoxia prevailed. One of the major objectives for this campaign was to study vertical mixing processes in the hypoxic zone. Vertical mixing is a key factor in controlling biogeochemical fluxes in the ocean, and it is driven by two major processes: divergent Ekman transport and turbulent mixing (*Cuypers et al.*, 2011). The latter is perhaps the most important and responsible for the downward supply of oxygen through the pycnocline and upward supply of nutrient from the bottom boundary layer (BBL), thus it needs to be accurately quantified in order to adequately represent biogeochemical processes (*Klein and Lapeyre*, 2009). Wind stress is the main source for mixing in the surface boundary layer (SBL) in the summer, while shear due to friction is responsible for the mixing in the BBL (*Palmer et al.*, 2013). Internal waves and shear advection may furthermore account for the dynamics in stratified layers between the SBL and BBL (*Thorpe*, 2004).

The present study, through a combined observational and modeling effort, aims to improve the understanding of turbulence dynamics and the influence of turbulence on hypoxia. Turbulence can be studied from direct measurements of the vertical turbulent fluxes, e.g. momentum fluxes ($\overline{u'w'}$ and $\overline{v'w'}$), heat flux ($\overline{\theta'w'}$), and salinity flux ($\overline{S'w'}$), but more often, turbulence quantities are examined as indirect measurements of turbulence. Turbulence quantities include, e.g. dissipation rate of temperature variance (χ), dissipation rate of turbulence kinetic energy (ϵ), eddy diffusivity of temperature (ν_t'), and eddy diffusivity of density (ν_ρ'). Turbulent processes have been

investigated in terms of these quantities in many studies (e.g. *Anis*, 2006; *Anis and Singhal*, 2006; *Cousins et al.*, 2010; *Cuypers et al.*, 2011). In the present study, turbulence dynamics throughout the water column were investigated using measurements of temperature and salinity microstructure, as well as the current profiles in the lower part of the water column. χ, ϵ, ν_t', and ν_ρ' were estimated from observational methods as follows. χ was calculated from the integral of the energy spectra of vertical temperature gradient ($\partial_z\theta$), and ϵ was then derived from a Batchelor fit to the energy spectra (*Batchelor*, 1959; *Oakey*, 1982; *Ruddick et al.*, 2000). ν_t' was calculated from the product of χ and $(\partial_z\theta)^2$ (*Oakey*, 1982; *Anis and Singhal*, 2006), and ν_ρ' was estimated as a function of ϵ and buoyancy frequency squared ($N^2 = -\frac{g}{\rho_0}\frac{\partial\rho}{\partial z}$, where ρ_0 is the mean density; *Ivey et al.*, 2008). Further details of observational methods for the four turbulence quantities are given in Section 3.3. Turbulent oxygen flux was estimated throughout the water, and the time required to remove bottom hypoxic layer by turbulence was calculated.

Two-equation second-moment turbulence models have been widely applied in turbulent mixing studies (*Umlauf and Burchard*, 2005). They consist of two transport equations: one for turbulence kinetic energy (k) and the other for a length scale (L) related quantity (e.g. ϵ or kL). This type of models has been applied for studies for an individual model with different parameterizations (*Burchard*, 2001b; *Bolding et al.*, 2002), comparisons between models (*Burchard*, 2001a; *Burchard et al.*, 2006, 2008), and comparisons between observations and models (*Anis and Singhal*, 2006; *Zhang and Drennan*, 2012). In the present study, the $k-\epsilon$ and $k-kL$ turbulence closures models were applied to simulate χ, ϵ, ν_t', and ν_ρ' for comparisons to observations. Turbulence theories and numerical models are commonly based on the assumption of locality (*Mellor and Yamada*, 1982; *Rodi*, 1987), but very often turbulence is influenced by non-local processes, such as advection (*Burchard*, 1999;

Anis and Singhal, 2006; *Burchard et al.*, 2006; *Cabrillo et al.*, 2011). Here, advection was accounted for by relaxing the simulations to the measured potential temperature (θ) and salinity (S).

The paper is structured as follows: after describing the study site (Section 3.2.1), the surface forcing (Section 3.2.2) and hydrography (Section 3.2.3) used for model simulations are presented. Advection of non-local water over the hypoxic layer is described in the context of the relatively high turbulence levels observed (Section 3.2.4). An introduction to observational methods is given in Section 3.3, followed by estimation of turbulent oxygen flux according to observed ν'_ρ (Section 3.4). A short description of the numerical models is given in Section 3.5. Observational and model results are compared for χ and ϵ in Section 3.6.1 and for ν'_t and ν'_ρ in Section 3.6.2. Discussion and conclusions are presented in Sections 3.7 and 3.8, respectively.

3.2 Experimental details

3.2.1 Study site

The study site C (Figure 3.1) is on the continental shelf of the Gulf of Mexico, 60 km south of the coast at 28°56′55″N 91°57′5″W, and has a water depth of 21.5 m. The campaign at site C was part of the NOAA Mechanisms Controlling Hypoxia (MCH) project (http://hypoxia.tamu.edu), and was conducted for 24 h from Aug. 22 20:00 to Aug. 23 20:00 (UTC = CDT + 5 h) during hypoxic conditions (*Rabalais et al.*, 2007).

3.2.2 Surface forcing

Momentum flux, τ_{wind}, was calculated from wind speeds measured at the nearest available source the National Data Buoy Center station LUML1 (29°15′12″N 90°39′48″W, Figure 3.1). During the field study, the weather was clear, and observed wave heights were less than 0.3 m. Meteorological conditions were characterized by

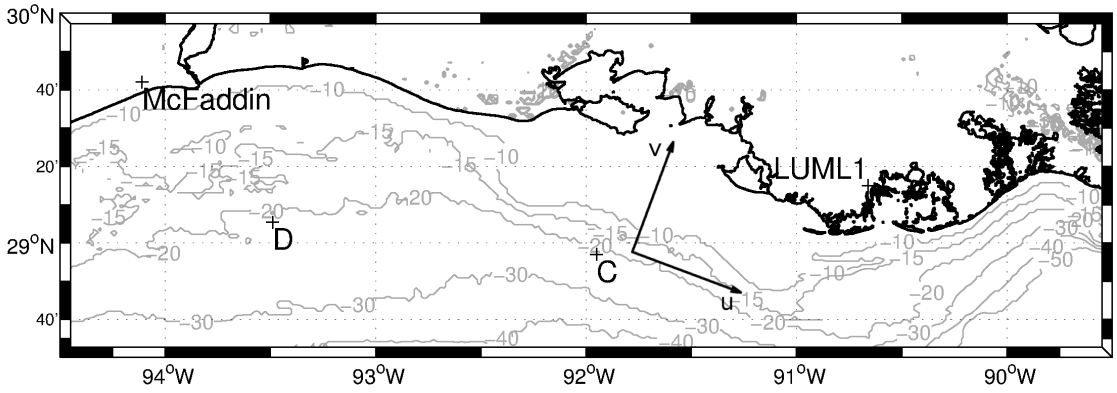

Figure 3.1: The measurements were conducted at site C on the Texas - Louisiana continental shelf. Net longwave radiation from NCEP was interpolated to site C; downward shortwave radiation was observed at fire station McFaddin; LUML1 buoy station that provided the rest of meteorological data required for calculations of surface heat and momentum fluxes. Velocity measurements were rotated to along-shelf (u) and cross-shelf (v) directions as presented by the axis system on the figure. Site D, about 150 km west of site C, included a bottom-mounted upward looking acoustic Doppler current profiler (ADCP).

low to moderate wind speeds with the average 2.8 m s^{-1} and the maximum 6.2 m s^{-1} (Figure 3.2a), resulting in $\tau_{wind} < 0.06$ N m^{-2} (Figure 3.2b).

Net surface heat flux, J_q^0, was computed as the sum of four components:

$$J_q^0 = J_q^{sw} + J_q^{lw} + J_q^l + J_q^s \tag{3.1}$$

where J_q^{sw} is the net shortwave radiation, J_q^{lw} is the net longwave radiation, J_q^l is the latent heat flux due to evaporation/condensation, and J_q^s is the sensible heat flux. J_q^{sw} was calculated from the measurement of incoming solar radiation at the US Forest Service weather station McFaddin (29°42′0″N 94°7′0″W, Figure 3.1), applying an albedo correction using the formula in *Payne* (1972). J_q^{lw} was computed from the sea surface temperature (SST) and downward longwave radiation following *Dickey et al.* (1994). The SST (Figure 3.2b) was obtained from profiles taken by a

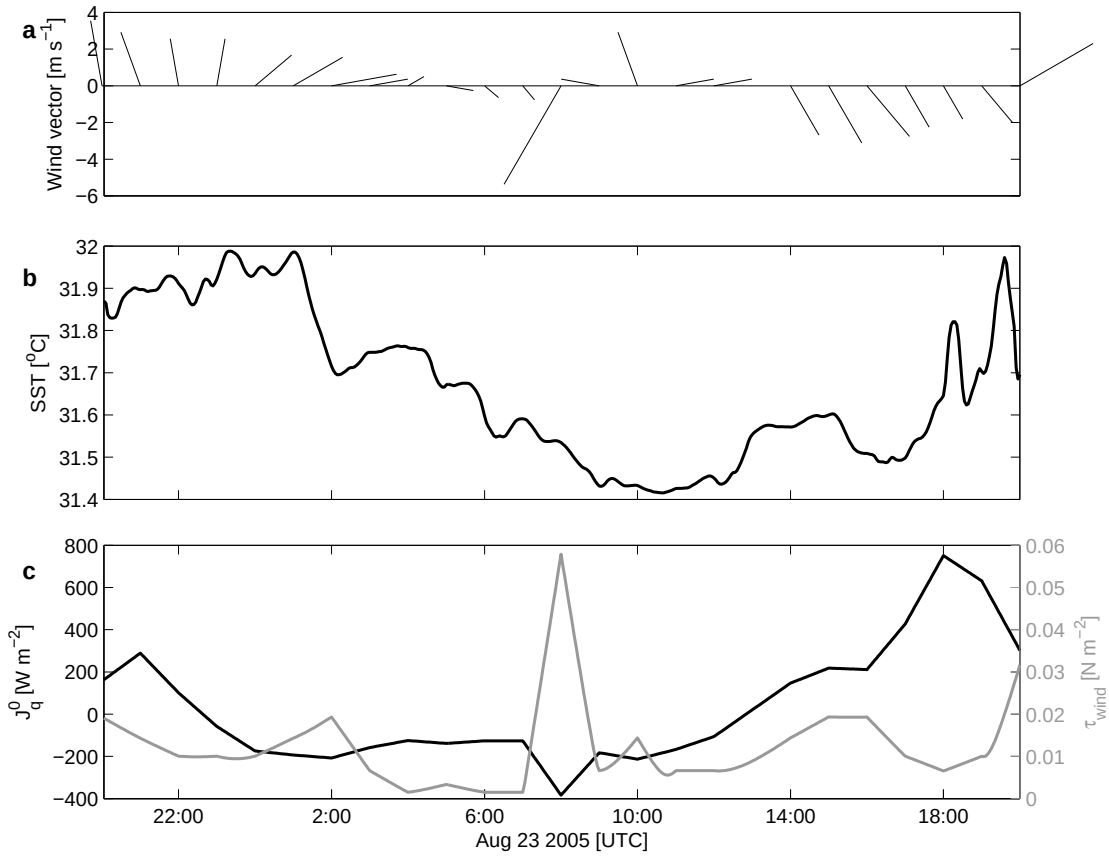

Figure 3.2: Meteorological measurements: (a) hourly wind vector; (b) sea surface temperature; (c) heat flux, J_q^o (black), and momentum flux, τ_{wind} (gray).

Self Contained Autonomous MicroProfiler (SCAMP, Precision Measurement Engineering). The downward longwave radiation was retrieved from the National Centers for Environmental Prediction/Department of Energy Reanalysis 2 (NCEP) database (*Sun et al.*, 2003; *Kubota et al.*, 2008), and interpolated to site C. J_q^l and J_q^s were calculated using wind speed, air temperature, relative humidity and air pressure from LUML1, and SST (*Fairall et al.*, 1996). During the period of the experiment, J_q^0 varied between -400 and 800 W m^{-2} (Figure 3.2c).

3.2.3 Hydrography

Vertical structures of temperature, salinity, and density were revealed from the SCAMP measurements. The SCAMP sensors include an accurate conductivity sensor, a fast conductivity sensor, two fast thermistors, and a pressure sensor (*MacIntyre et al.*, 1999; *Jurado et al.*, 2012). Downward profiles of temperature, small-scale vertical temperature gradients ($\partial_z T$), conductivity, and pressure were taken every $\sim$7 min while this instrument fell freely at a speed $\sim$ 0.1 m s^{-1}. Measurements started at $\sim$ 1 m below the surface and reached down to the seafloor. Measurements of accurate conductivity were chosen for calculations because signals from the fast conductivity sensor were contaminated. Measurements from the two fast thermistors were in good agreement, thus one of the two measurements were chosen for the calculations.

Profiles of θ, S, and σ_θ, shifted by 0.3 units and aligned with time and sea surface elevations, are presented in Figure 3.3. The SBL (BBL) of θ was marked by black dots where the temperature is 0.1 ^{o}C lower (higher) than that at the surface (bottom) in each profile (Figure 3.3b). The SBLs and BBLs of S and σ_θ were defined analogously but with the vertical differences 0.1 PSU and 0.1 kg m^{-3}, respectively (Figure 3.3c, d). The mean depth of SBL of σ_θ (6.07 m) was same as that of S and 1.9 m shallower than that of θ, while the mean depth of BBL of σ_θ (18.11 m) was

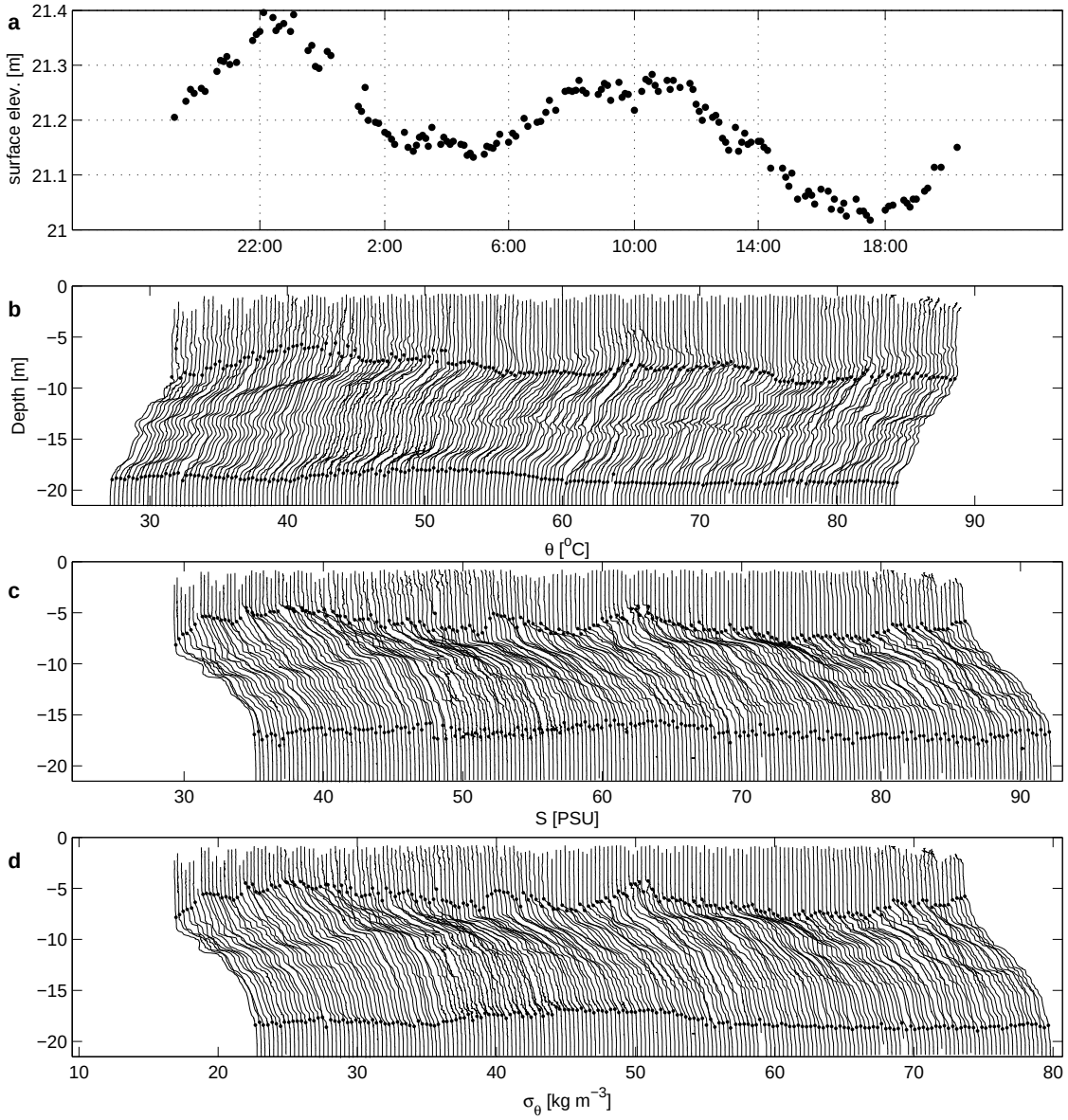

Figure 3.3: (a) surface elevation; SCAMP profiles of (b) θ, (c) S, and (d) σ_θ. The SBLs and BBLs defined in θ (b), S (c), and σ_θ (d) profiles are marked by black dots where the values are 0.1 units different than those at the surface and at the bottom, respectively. Profiles are offset by 0.3 units and aligned with the time in (a). Time intervals between profiles are ~ 7 min.

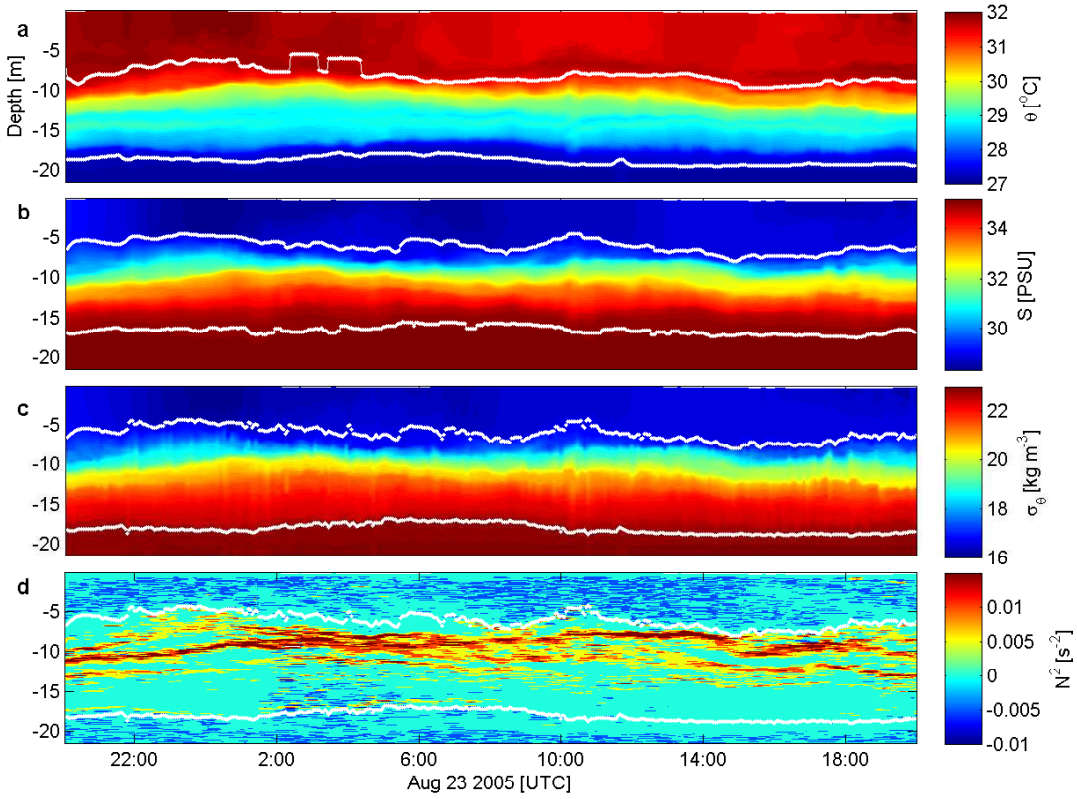

Figure 3.4: Contours from SCAMP profiles at site C: (a) potential temperature, θ; (b) salinity, S; (c) σ_θ; (d) buoyancy frequency squared, N^2. The SBLs and BBLs defined in θ (a), S (b), and σ_θ (c, d) are marked by white dots.

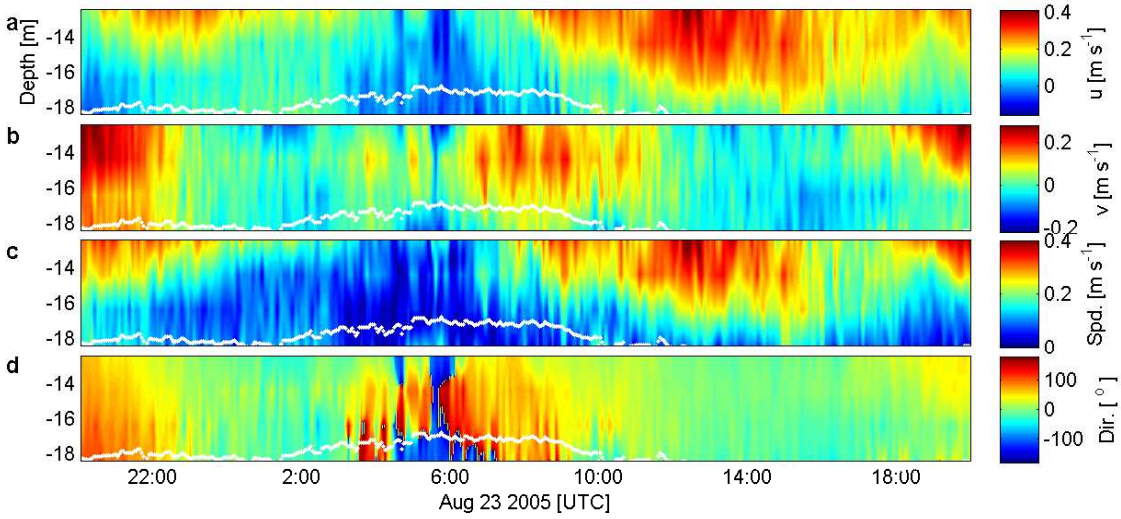

Figure 3.5: Ship hull-mounted ADCP velocity contours between depths 12.4 and 18.4 m at site C: (a) along-shelf velocity, u; (b) cross-shelf velocity, v; (c) current speed; (d) current direction (0 is the along-shelf direction and angles increase counter-clockwise). The BBL defined in σ_θ is marked by white dots.

1.53 m below that of S and 0.7 m above that of θ. An enhanced mixing section in density profiles is shown between 10 and 18 m from 2:00 to 5:00 (Figure 3.3d). The mixing was caused by rapid changes in both measured θ and S (Figure 3.3b, c), which elevated the depth of SBL of θ at the top of the mixing section (Figure 3.4a). Below the SBL of σ_θ, N^2 presented high values, indicating the pycnocline (Figure 3.4d). In the following study, we denote the SBL, mid layer, and BBL as defined in σ_θ profiles unless they are specified otherwise.

Velocity profiles were measured from a ship (R/V Gyre) hull mounted Teledyne RD Instruments 150 kHz acoustic Doppler current profiler (ADCP). Eastward and northward velocities were rotated 15^o clockwise to along-shelf (u) and cross-shelf (v) directions (Figure 3.1). Measurements started at a depth of 12.4 m, with a bin size of 2 m and an interval of 5 min (Figure 3.5a, b). Data deeper than 18.4 m were discarded due to side-lobe contamination from bottom echoes (*Nystrom et al.*, 2002).

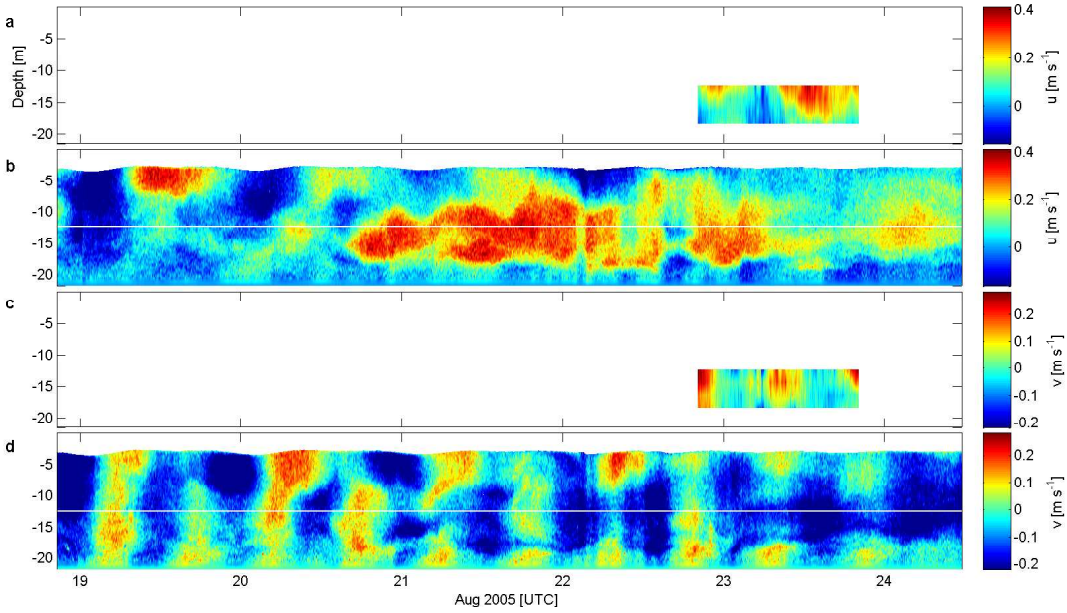

Figure 3.6: Current measurements: along-shelf velocities at site C (a) and D (b); cross-shelf velocities at site C (c) and D (d). A white line at 12.4 m was added on panels b and d to indicate the start depth of current measurements at site C. Currents at site D were measured from an upward looking ADCP (Nortek 1 MHz Aquadopp).

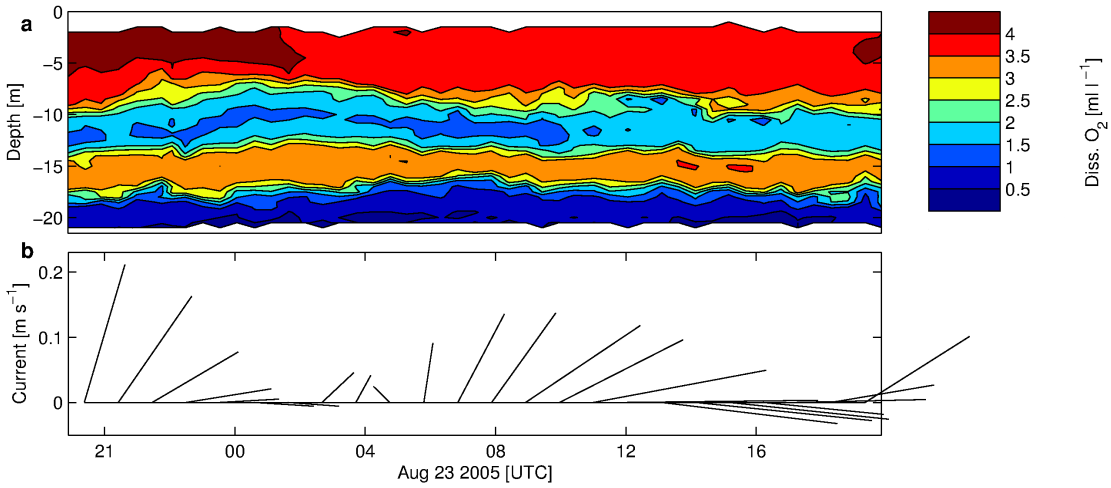

Figure 3.7: Measurements from the CTD on the research vessel: (a) dissolved oxygen; (b) hourly averaged current vectors at 15 m.

An increase in the current speed was observed after 8:00 (Figure 3.5c), it might be related to the increase of momentum flux (Figure 3.2c). Water through the column was nearly static around 6:00, showing intermittent changes of current directions (Figure 3.5d). Current velocities at site C were compared to those 150 km westward at site D (Figure 3.1) where measurements were taken for a period of more than 5 days that encompassed the period of the present experiment at site C (for details of site D see Section 2), and the comparison indicated that both sites were under similar tidal conditions, given that the semi-diurnal changes of v at sites C and D (Figure 3.6c, d) were in agreement.

3.2.4 Hypoxia and advection

Dissolved oxygen (DO) concentrations were obtained using a DO sensor equipped on a Sea-Bird Electronics 911 CTD every 30 min (Figure 3.7a). A surface layer with DO $>$ 3 ml l^{-1} was above the pycnocline. Strongly stratified water in the mid layer practically inhibited vertical transport of oxygen, causing a decrease in DO to

between 1.5 and 3 ml l^{-1} below the pycnocline. A layer of high-concentration DO ($\geq$ 3 ml l^{-1}) water occurred between 14 and 18 m. Hourly averaged current velocities at 15 m were primarily east or northeast (Figure 3.7b), indicating the advection of non-local water. Hypoxia is defined as DO $<$ DO_c = 1.4 ml l^{-1} (critical value) and was present near the bottom, it corresponded to the pycnocline near the BBL (Figure 3.4d) which kept DO from transporting downward.

3.3 Observational methods

ϵ was calculated based on the theoretical Batchelor spectrum (*Batchelor*, 1959; *Dillon and Caldwell*, 1980; *Oakey*, 1982; *Imberger and Ivey*, 1991) and given by

$$\epsilon = k_B^4 \nu \nu_T^2, \tag{3.2}$$

where $\nu = 8 \times 10^{-7}$ m^2 s^{-1} is the kinematic viscosity at 30°C, $\nu_T = 1.4 \times 10^{-7}$ m^2 s^{-1} is the thermal diffusivity, and k_B is the Batchelor cutoff wavenumber estimated from the Batchelor spectrum:

$$E(\hat{k}_{wn}) = \left(\frac{q}{2}\right)^{\frac{1}{2}} \frac{\chi}{k_B \nu_T} g(q, \hat{k}_{wn}/k_B), \tag{3.3}$$

where $q = 3.4$ was chosen in this study (*Grant et al.*, 1968; *Dillon and Caldwell*, 1980; *Ruddick et al.*, 2000), and $g(q, \hat{k}_{wn}/k_B)$ is given by

$$g(q, \hat{k}_{wn}/k_B) = 2\pi \left(e^{-\alpha^2/2} - \alpha \int_\alpha^\infty e^{-x^2/2} dx \right), \tag{3.4}$$

where $\hat{k}_{wn} = k_{wn}/2\pi$ is the cyclic wavenumber, and

$$\alpha = (2q)^{\frac{1}{2}} \frac{2\pi \hat{k}_{wn}}{k_B}. \tag{3.5}$$

χ is given by

$$\chi = 6\nu_T \overline{(\partial_z \theta')^2} = 6\nu_T \int_t^\infty \left(E_{obs}(\hat{k}_{wn}) - E_n(\hat{k}_{wn}) \right) d\hat{k}_{wn}, \tag{3.6}$$

where θ' is the potential temperature fluctuation, E_{obs} is the observed spectrum of $\overline{(\partial_z \theta')^2}$, and E_n is the instrument's noise spectrum. Spectra of $\overline{(\partial_z \theta')^2}$ were calculated for segments in which turbulence was determined to be statistically stationary (*Imberger and Ivey*, 1991; *Chen et al.*, 2002), and χ was estimated by integrating the spectra of each segment. The best fit of Batchelor spectrum of the observed spectrum was estimated using the Maximum likelihood algorithm introduced by *Ruddick et al.* (2000).

A profile in the enhanced mixing section (Figure 3.8a) was compared to another in a calm condition (Figure 3.8c). The variation of $\partial\theta/\partial z$ in the first profile was $\sim$ 4 times that in the second profile, while temperatures were in the same range. $\partial\theta/\partial z$ from the first profile indicated strong turbulence activity in the mid layer (7.6 $\sim$ 18.1 m). χ and ϵ (Figure 3.8b) estimated from the measurements in the segment between 7.9 and 8.4 m (marked by two horizontal dashed lines, Figure 3.8a) in the first profile were at least 2 orders of magnitude higher than those (Figure 3.8d) from the measurements in the segment between 18.8 and 19.4 m (marked by two horizontal dashed lines, Figure 3.8c) in the second profile.

ν_t' is given by

$$\nu_t' = \frac{\chi}{2} \left(\frac{\partial T}{\partial z} \right)^{-2}, \tag{3.7}$$

and ν_ρ' is given by

$$\nu_\rho' = \Gamma \frac{\epsilon}{N^2}, \tag{3.8}$$

where $\Gamma = 0.2$ is the mixing efficiency (*Osborn*, 1980; *Moum*, 1996; *Nash et al.*, 2007).

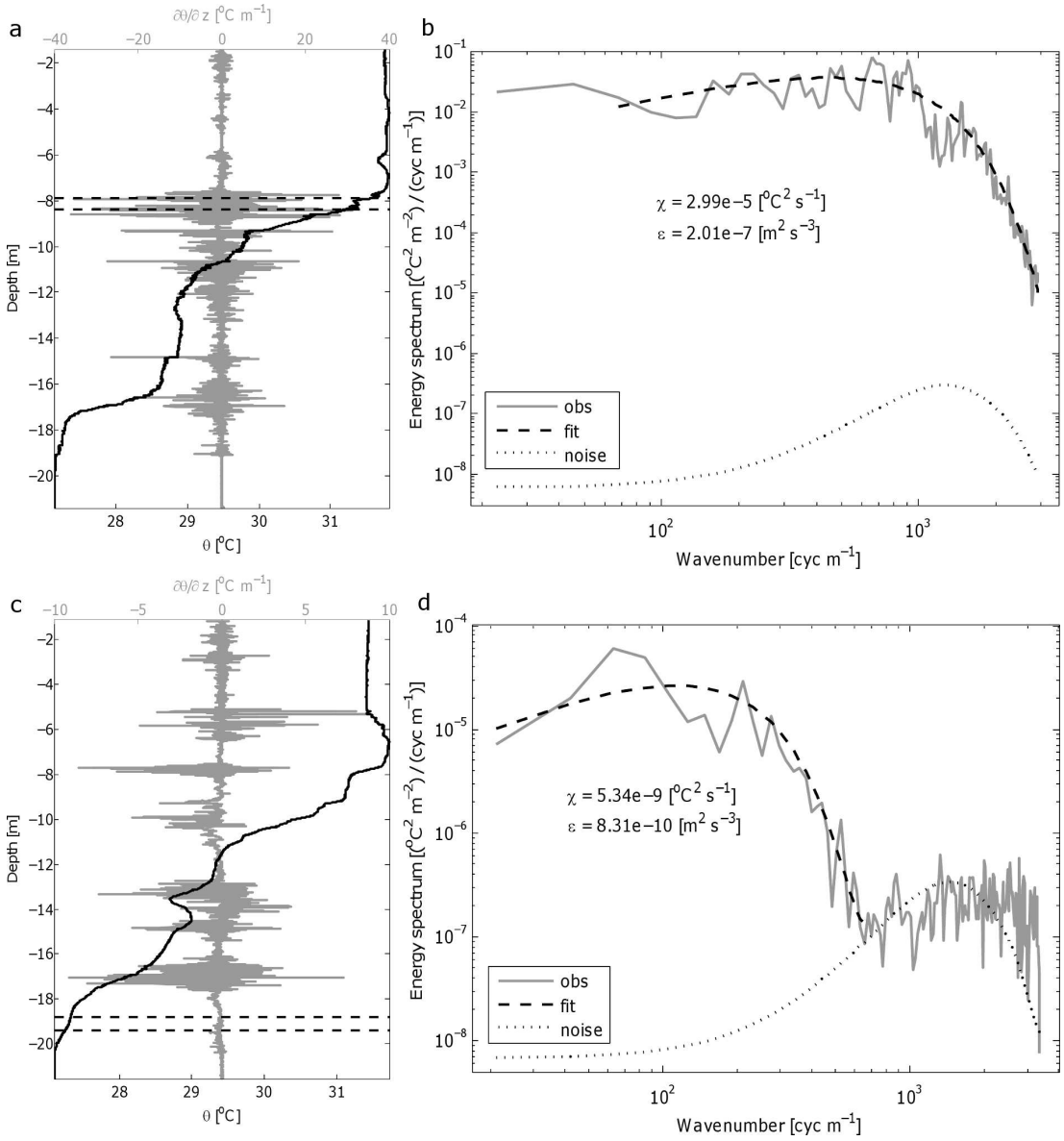

Figure 3.8: (a) an example of a high turbulence energy profile taken at 3:22:00, showing potential temperature, θ (black), and vertical gradient of potential temperature, $\partial_z\theta$ (gray); (b) observed spectra (solid line) and fit (dashed line) of a theoretical Batchelor spectrum for the profile segment (7.9 - 8.4 m) marked by two dashed horizontal lines in (a). SCAMP's noise level is shown by the dotted line; (c) similar to (a) but for a relatively low turbulence energy profile taken at 11:08:38. Note the scale for $\partial\theta/\partial z$ is smaller than that in (a) by a factor of 4; (d) observed spectra and fit for the profile segment between 18.8 and 19.4 m marked by two dashed horizontal lines in (c).

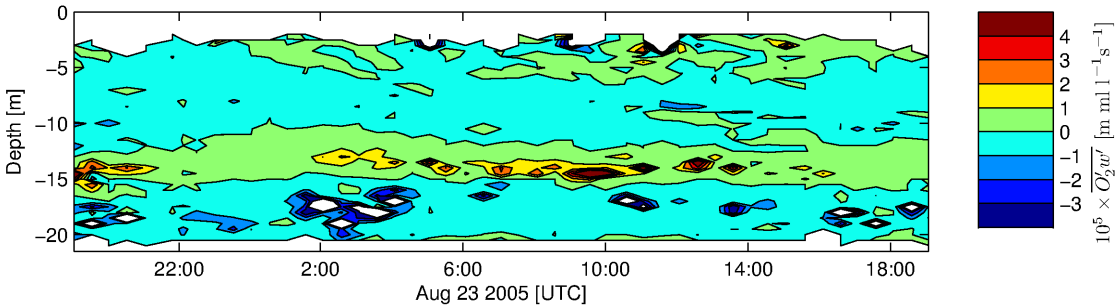

Figure 3.9: Turbulent oxygen flux, $\overline{O_2'w'}$, throughout the water column. Positive (negative) values indicate upward (downward) fluxes.

3.4 Turbulent oxygen flux

Turbulent oxygen flux is given by

$$\overline{O_2'w'} = -\nu_\rho' \frac{\partial O_2}{\partial z} \tag{3.9}$$

High DO in the SBL resulted in downward flux (Figure 3.9), and DO in the non-local water was transferred upward and downward to relative low DO water. To replenish oxygen to DO = $\mathrm{DO_c}$ in the bottom hypoxic layer, the time (t_{O_2}) required was estimated by

$$-\frac{\overline{O_2'w'}t_{O_2}}{h_{O_2}} = |\mathrm{DO_c} - \mathrm{DO}|, \tag{3.10}$$

where $\overline{O_2'w'} = 4.76 \times 10^{-6}$ m ml l^{-1} s^{-1} is the average turbulent oxygen flux in the bottom hypoxic layer, $h_{O_2} = 4.38$ m is the thickness of the layer, $\mathrm{DO_c} = 1.4$ ml l^{-1}, DO = 0.73 ml l^{-1} is the average DO in the layer. Thus $t_{O_2} \approx 7.11$ days.

In the relatively low-DO layer (DO $\leq$ 2 ml l^{-1}) between 6 and 15 m, vertically averaged DO (Figure 3.10a) was not consistent with the turbulent oxygen flux (Figure 3.10b), which indicate that DO was not primarily affected by the oxygen flux but by stratification and shear stress, although the increase of DO, from 1.6 to 2.5 ml l^{-1}

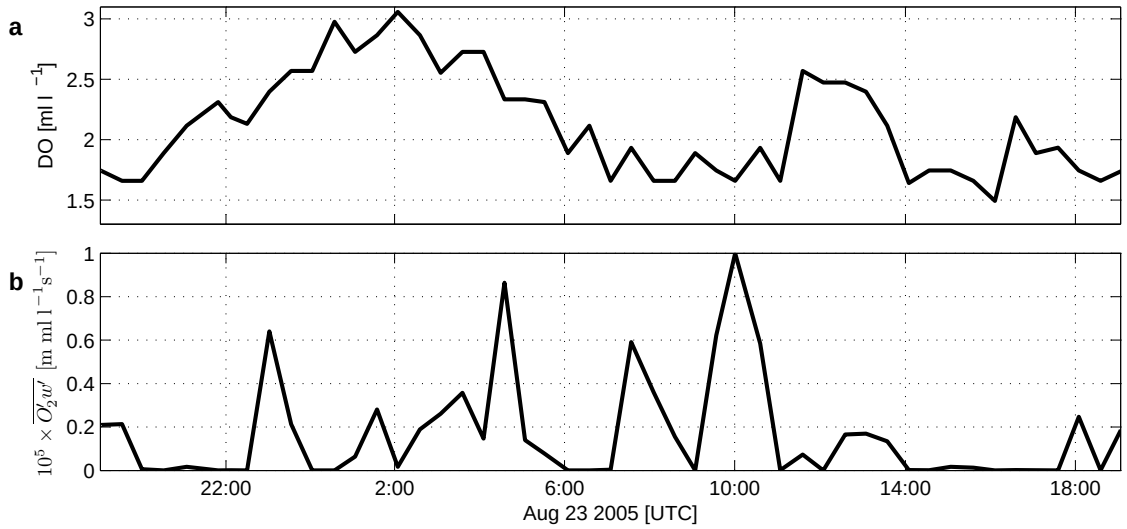

Figure 3.10: (a) vertically averaged dissolved oxygen in the water within the two layers of DO = 2 ml l^{-1} between depths of 6 and 15 m; (b) sum of the turbulent oxygen fluxes at the layers.

after 11:00, might be related to the turbulent oxygen flux.

3.5 Model methods

The one-dimensional water column General Ocean Turbulence Model (GOTM; *Burchard et al.* 1999) was used in the present study. The GOTM provides choices for different types of turbulence closures and stability functions (c_μ and c'_μ), and has been successfully applied to reproduce turbulence in different physical scenarios, e.g. tidal straining (*Simpson et al.*, 2002), stratification (*Burchard*, 2002), near-bottom dense inflow (*Arneborg et al.*, 2007), convection in a lake (*Stips et al.*, 2002), and near surface turbulence (*Stips et al.*, 2005). As a physical model, the modular structure of GOTM makes it possible to couple with biogeochemical models (e.g. ecosystem, *Burchard et al.* 2006; *Molen et al.* 2012).

Two model combinations in the GOTM were applied for the following part of this study:

- CH: the $k-\epsilon$ turbulence closure with the stability functions of *Cheng et al.* (2002);

- SG: the $k-kL$ turbulence closure with the stability functions of *Schumann and Gerz* (1995).

The CH and SG models estimate turbulent fluxes as functions of a turbulent diffusivity and a gradient of mean water property:

$$\overline{u'w'} = -\nu_t \frac{\partial \overline{u}}{\partial z}, \tag{3.11}$$

$$\overline{v'w'} = -\nu_t \frac{\partial \overline{v}}{\partial z}, \tag{3.12}$$

$$\overline{T'w'} = -\nu'_t \frac{\partial \overline{T}}{\partial z}, \tag{3.13}$$

$$\overline{S'w'} = -\nu'_t \frac{\partial \overline{S}}{\partial z}, \tag{3.14}$$

where ν_t is the eddy diffusivity of momentum. For further details of the two models and the equations for ϵ, see Section 2. In both models, χ is given by equation (3.7) in which ν'_t is derived from

$$\nu'_t = c'_\mu k^{\frac{1}{2}} L, \tag{3.15}$$

while ν'_ρ is calculated from equation (3.8) in both models.

The CH and SG models were forced by the observed meteorological surface forcing, i.e. heat and momentum fluxes. In addition, they were relaxed to observed θ and S profiles every 300 s so that simulations did not deviate much from measurements due to advection (*Anis and Singhal*, 2006; *Cabrillo et al.*, 2011). No relaxation to observed velocities was used due to the low vertical resolution of velocity measurements.

	$10^9\chi$ [^{o}C s^{-1}]			$10^9\epsilon$ [m^2 s^{-3}]		
Layer	obs	CH	SG	obs	CH	SG
SBL	45.0	4.18	6.92	37.7	8.19	9.34
	[41.9 47.8]	[3.80 4.62]	[6.33 7.55]	[35.4 40.4]	[7.48 9.03]	[8.57 10.2]
mid layer	16.4	0.060	0.214	10.7	0.008	0.012
	[15.5 17.6]	[0.056 0.064]	[0.200 0.228]	[10.2 11.2]	[0.007 0.008]	[0.011 0.013]
BBL	10.2	9.07	31.5	3.66	5.24	14.2
	[9.15 11.3]	[8.03 10.2]	[28.5 34.2]	[3.41 3.94]	[4.62 5.95]	[13.0 15.5]

Table 3.1: Mean values and 95% confidence intervals (in square brackets) for χ and ϵ computed over the period of the experiment using the bootstrap method with 1000 samples (*Emery and Thomson*, 2001).

3.6 Comparison between observational and model results

3.6.1 χ and ϵ

Observed and modeled turbulence quantities, χ and ϵ, are shown with the SBL and BBL defined in σ_θ in Figure 3.11. Observed χ and ϵ presented large values consistent with the SBL defined in θ, exceeding the SBL defined in σ_θ, while modeled quantities showed clear confinement in the SBL defined in θ. The CH and SG models were forced without velocity measurements shallower than 12.4 m where χ and ϵ were, thus, simulated with temperature and salinity measurements only. The expanded high-value region from the SBL resulted in the mean values of observed χ and ϵ 2 orders of magnitude greater than those of modeled χ and ϵ in the mid layer (Table 3.1).

Values of observed χ and ϵ from 2:00 to 5:00 (Figure 3.11a, d) were higher compared to those in any other time between 10 and 18 m, which was induced by the enhanced mixing shown in θ, S, and σ_θ profiles (Figure 3.3). The "stripe" for high values of observed χ and ϵ between 13 and 16 m may be a result of the advection of non-local water. The CH and SG models reproduced only a fraction of the "stripe", and almost failed to simulate after 6:00 (Figure 3.11b, c, e, f). A boost in ϵ values for the CH and SG models in the SBL between 7:00 and 9:00 was not present in

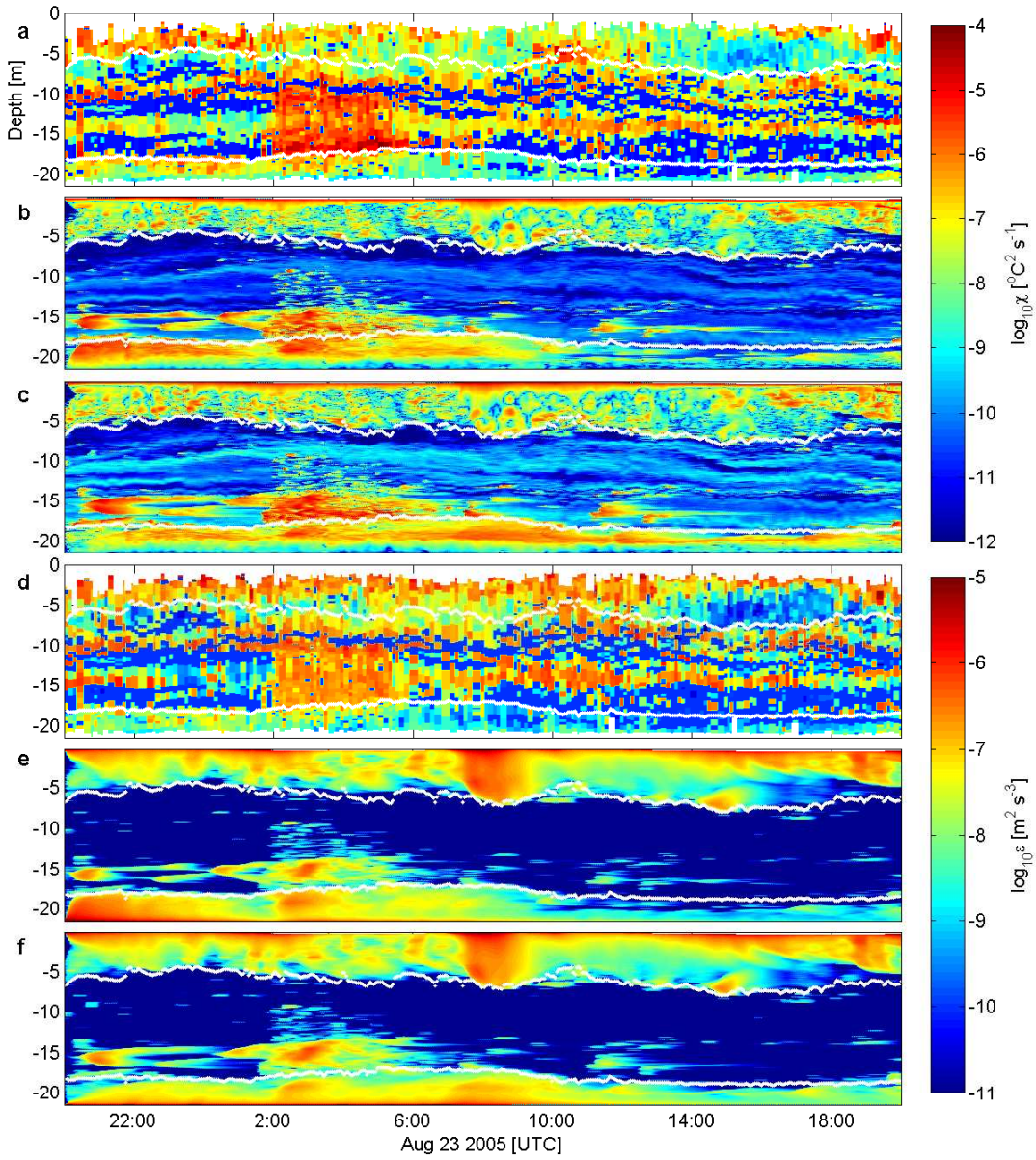

Figure 3.11: (a) observed χ; (b) CH modeled χ; (c) SG modeled χ; (d) observed ϵ; (e) CH modeled ϵ; (f) SG modeled ϵ. The SBL and BBL defined in σ_θ are marked by white dots.

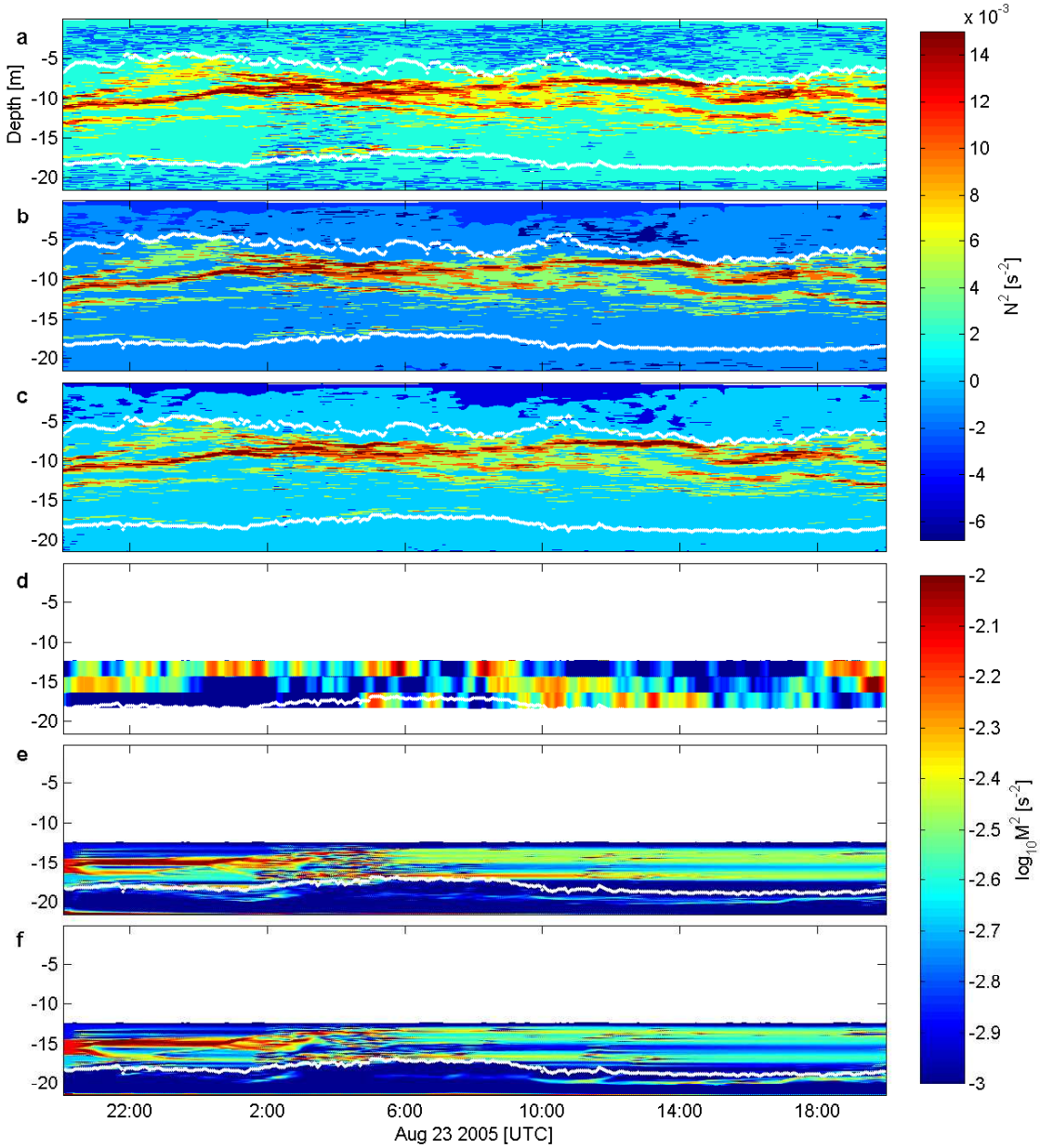

Figure 3.12: (a) observed N^2; (b) CH modeled N^2; (c) SG modeled N^2; (d) observed M^2; (e) CH modeled M^2; (f) SG modeled M^2. The SBL and BBL defined in σ_θ are marked by white dots.

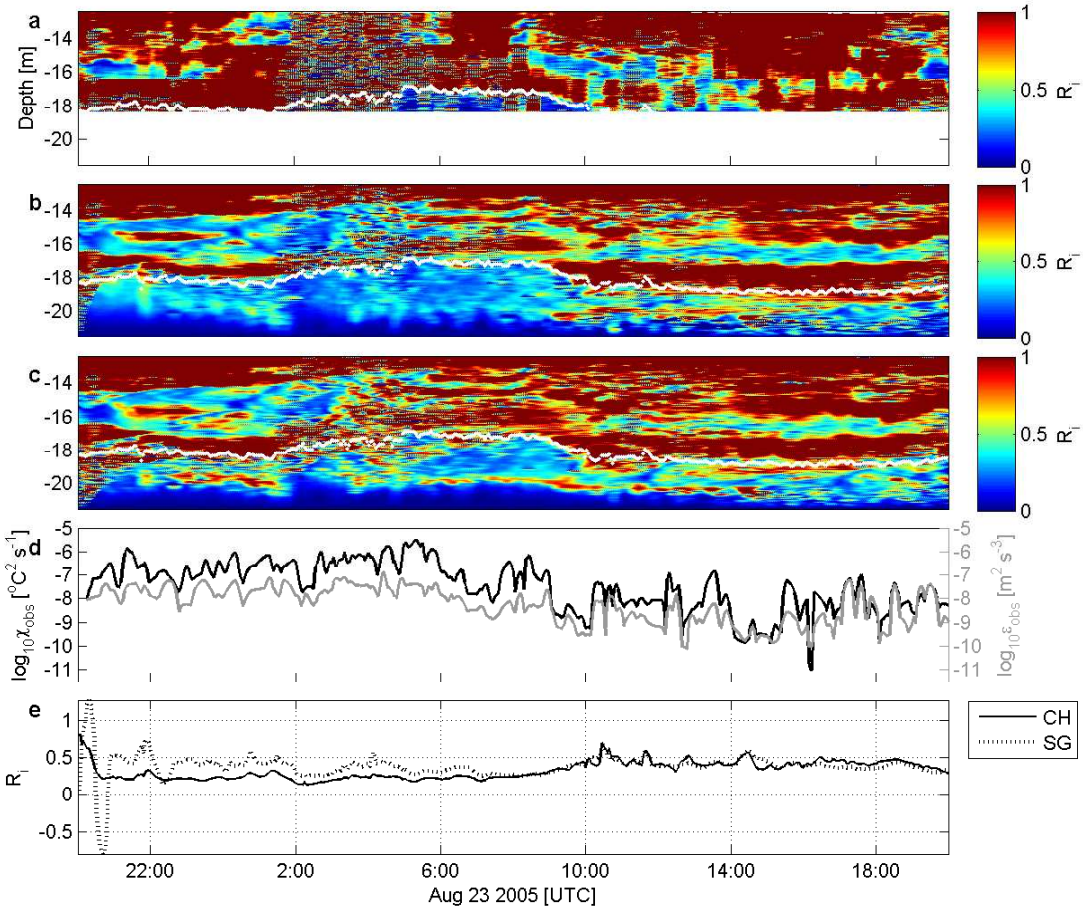

Figure 3.13: (a) observed R_i; (b) CH modeled R_i; (c) SG modeled R_i; (d) vertically averaged observed χ and ϵ in the BBL; (e) vertically averaged R_i of observations and CH and SG model simulations in the BBL. The BBL defined in σ_θ is marked by white dots.

observed ϵ. This may be due to that the models were forced by the wind measured from LUML1. However, the in situ wind seemed not to have speeds as high as 6.2 m s^{-1} over that duration. With the relaxation to θ and S, both models showed similar N^2 values to those observed (Figure 3.12a, b, c), while observed shear frequency squared ($M^2 = (\partial_z \overline{u})^2 + (\partial_z \overline{v})^2$, where overbar denotes an ensemble average) were not consistently reproduced by the models which were not relaxed to measured velocities (Figure 3.12d, e, f). Values of modeled gradient Richardson number ($R_i = N^2/M^2$) deviated from those observed because model simulations were not relaxed to velocity measurements (Figure 3.13a, b, c), however, vertically averaged observed χ and ϵ in the BBL (Figure 3.13d) were well represented by simulated R_i from both models at the corresponding depths (Figure 3.13e), showing high R_i values correspondent with low χ and ϵ values.

Three one-hour periods were chosen for comparison of χ and ϵ profiles between observations and the CH and SG model simulations: 22:00 - 23:00, before the enhanced mixing event (Figure 3.14a, e); 2:00 - 3:00, during the mixing event (Figure 3.14b, f); 14:00 - 15:00, after the mixing event when turbulence activity in the BBL was relatively weak (Figure 3.14c, g). The simulations appear to agree with the observations in the SBL and BBL better than in the mid layer. For ϵ, model results decreased to the numerical limit (10^{-12} m^2 s^{-3}) in the mid layer during most of the time (e.g. Figure 3.14e, g). Averages over the entire time (24 hours) revealed similar relations between observations and model simulations (Figure 3.14d, h). Statistics of one-hour averaged χ and ϵ in the SBL, mid layer, and BBL are presented in Table 3.1. The CH model values were more consistent with observed values than those of the SG model in the BBL with respect to mean value with 95% confidence interval. Mid-layer turbulence activities were underestimated by the CH model by $2-3$ orders of magnitude, whereas the SG model results showed higher values than those of the

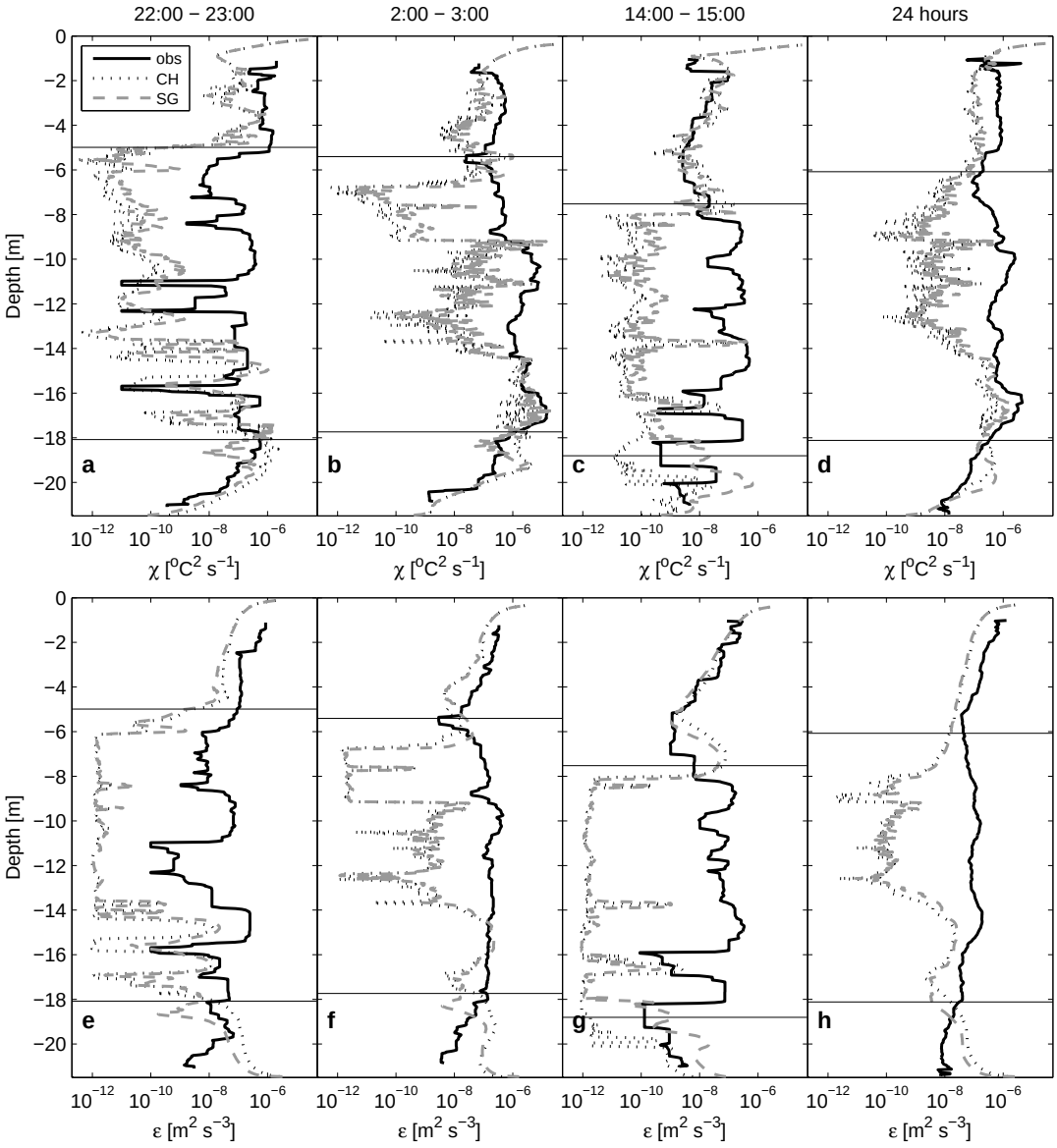

Figure 3.14: Observed and CH and SG modeled χ and ϵ profiles temporally averaged in (a,e) 22:00 - 23:00, (b,f) 2:00 - 3:00, (c,g) 14:00-15:00, and the entire time (d,h), respectively. Ensemble averaged SBLs and BBLs are marked by horizontal solid lines.

Layer	$corr_\chi$ (obs,CH)	(obs,SG)	(CH,SG)	$corr_\epsilon$ (obs,CH)	(obs,SG)	(CH,SG)
SBL	0.26	0.28	0.95	0.51	0.50	0.95
	[0.24 0.28]	[0.25 0.30]	[0.94 0.95]	[0.49 0.53]	[0.48 0.53]	[0.95 0.96]
mid layer	0.12	0.13	0.93	0.18	0.17	0.92
	[0.10 0.14]	[0.11 0.15]	[0.93 0.94]	[0.16 0.20]	[0.15 0.19]	[0.91 0.92]
BBL	0.70	0.32	0.63	0.67	0.27	0.63
	[0.67 0.72]	[0.27 0.36]	[0.60 0.66]	[0.65 0.70]	[0.23 0.32]	[0.60 0.66]

Table 3.2: Cross-correlation values and 95% confidence intervals (in square brackets) for χ and ϵ computed over the period of the experiment using the bootstrap method with 1000 samples.

CH model but still much lower than those observed.

Correlations for χ and ϵ (Table 3.2) between observations and model simulations were consistent with the statistics of mean values in Table 3.1, presenting the highest correlation in the BBL and the lowest correlation in the mid layer. The CH model showed higher correlations to observations than the SG model in the BBL, which will be explained in the inter-model comparisons in the next paragraph. The two models showed similar results in the SBL, with only a small difference of 2% between $corr_\chi$(obs,CH) and $corr_\chi$(obs,SG) and 1% between $corr_\epsilon$(obs,CH) and $corr_\epsilon$(obs,SG).

Differences between the two models were also examined by comparing ratios of the SG model to the CH model for χ and ϵ (Figure 3.15). In the SBL, the CH and SG modeled χ and ϵ values were highly correlated, resulting in ratios ~ 1 on average (Figure 3.15). In the mid layer, ratios were ~ 3 on average for χ (Table 3.1), and were ~ 1 on average for ϵ. Overestimation of ratios for χ is consistent to the model results in Section 2, which was found to be due to the simple stability functions of *Schumann and Gerz* (1995). In the BBL, the SG modeled values were lower before 23:00 and higher after 8:00 than the CH model values, thus the two models were not highly correlated for either χ or ϵ ($corr_\chi$(CH,SG) = $corr_\epsilon$(CH,SG) = 0.63, Table 3.2). The SG model overestimated both turbulence quantities on average (Table 3.1).

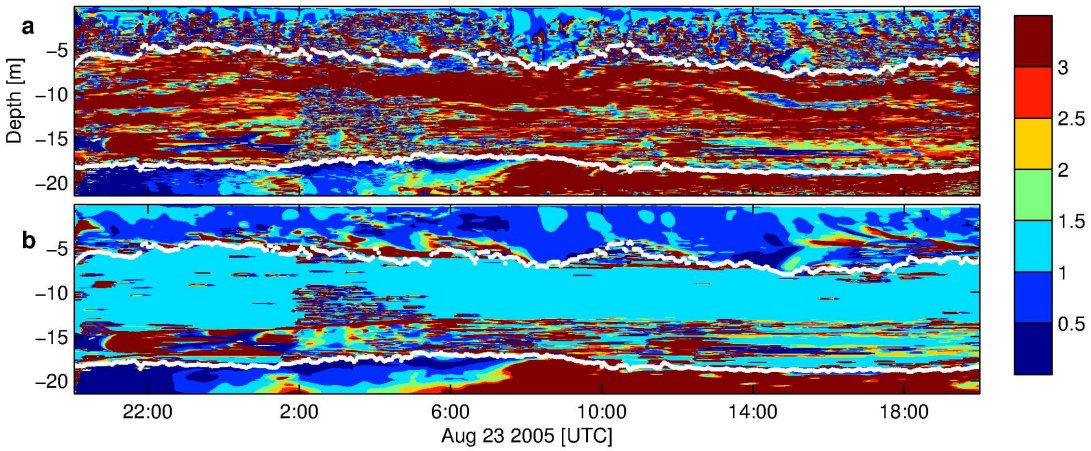

Figure 3.15: Ratios of SG model values to CH model values for (a) χ and (b) ϵ. The SBL and BBL defined in σ_θ are marked by white dots.

	$10^7\nu_t'$ [m^2 s^{-1}]			$10^7\nu_\rho'$ [m^2 s^{-1}]		
Layer	obs	CH	SG	obs	CH	SG
SBL	184	382	617	202	608	605
	[172 197]	[342 426]	[564 679]	[187 216]	[539 683]	[545 677]
mid layer	0.464	0.010	0.034	6.67	0.010	0.016
	[0.426 0.505]	[0.009 0.011]	[0.032 0.036]	[6.36 6.98]	[0.009 0.011]	[0.014 0.017]
BBL	3.31	207	227	22.4	450	409
	[2.86 3.73]	[190 227]	[206 248]	[20.8 24.3]	[401 502]	[361 457]

Table 3.3: Mean values and 95% confidence intervals (in square brackets) for ν_t' and ν_ρ' computed over the period of the experiment using the bootstrap method with 1000 samples.

3.6.2 ν_t' and ν_ρ'

In the BBL, the differences between observations and CH model results for χ for ν_t' or ν_ρ' were more than an order of magnitude, while in the SBL, both models presented the smaller differences within a factor of 4. These might be explained as that observed ν_t' and ν_ρ' in the BBL were patchy, and none of the models were able to predict the intermittency of the turbulence quantities. Differences between observations and models in the SBL were not as significant as those in the BBL (Figure 3.16, Table 3.3) because models took surface fluxes induced turbulence, other

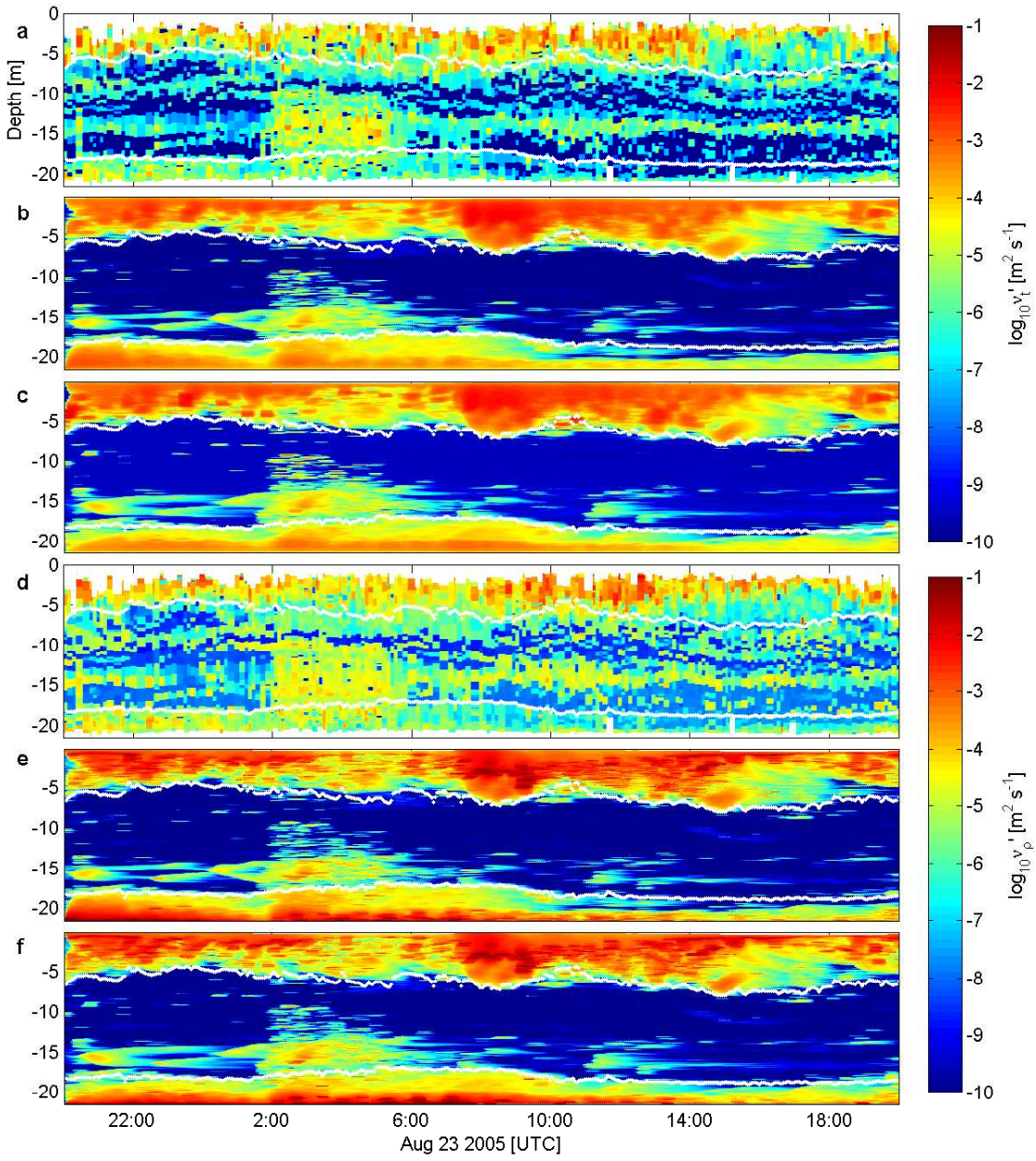

Figure 3.16: Eddy diffusivity of temperature (ν_t') from (a) the observations, (b) the CH model, and (c) the SG model; eddy diffusivity of density (ν_ρ') of (d) the observations, (e) the CH model, and (f) the SG model. The SBL and BBL defined in σ_θ are marked by white dots.

Depth [m]	$corr_{\nu'_t}$ (obs,CH)	(obs,SG)	(CH,SG)	$corr_{\nu'_\rho}$ (obs,CH)	(obs,SG)	(CH,SG)
SBL	0.52	0.52	0.97	0.62	0.62	0.97
	[0.49 0.54]	[0.50 0.55]	[0.96 0.97]	[0.60 0.64]	[0.60 0.64]	[0.97 0.97]
mid layer	0.31	0.33	0.95	0.35	0.35	0.95
	[0.29 0.33]	[0.31 0.34]	[0.94 0.95]	[0.33 0.37]	[0.33 0.36]	[0.95 0.96]
BBL	0.69	0.60	0.75	0.65	0.50	0.82
	[0.67 0.72]	[0.57 0.63]	[0.73 0.77]	[0.62 0.67]	[0.46 0.53]	[0.81 0.83]

Table 3.4: Cross-correlations and 95% confidence intervals (in square brackets) for ν'_t and ν'_ρ were computed over the period of the experiment using the bootstrap method with 1000 samples.

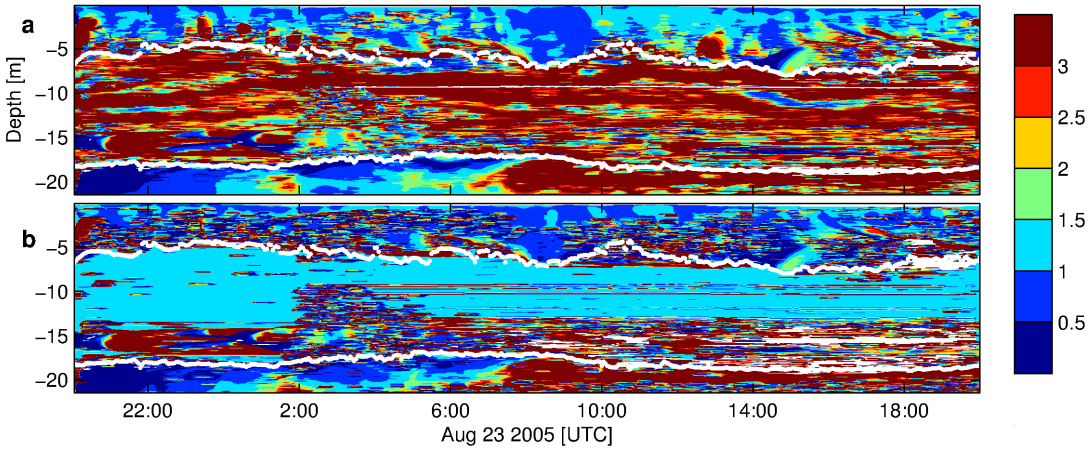

Figure 3.17: Ratios of SG model values to CH model values for (a) ν'_t and (b) ν'_ρ. The SBL and BBL for σ_θ are marked by white dots.

than current induced turbulence, into account. Correlations between observations and models for ν_t' and ν_ρ' (Table 3.4) were primarily higher than those for χ and ϵ (Table 3.2), which was due to that 1) ν_t' was regulated by c_μ' as shown in equation (3.15), 2) ν_ρ' was regulated by N^2 in equation (3.8) which was relaxed to observed θ and S. Ratios of the SG model to the CH model for ν_t' and ν_ρ' (Figure 3.17) were similar to those for χ and ϵ (Figure 3.15), and high ratios (≥ 3) in the mid layer were due to the simplified stability functions of *Schumann and Gerz* (1995) since ν_t' is a function of c_μ' in equation (3.15).

3.7 Discussion

Second-moment turbulence closure models are primarily descriptions of vertical mixing. They usually reproduce turbulent dynamics well in boundary layers, but fail to predict in stratified layers, especially in pycnocline (*Simpson et al.*, 1996; *Burchard et al.*, 2008). The vertical mixing due to advection shear in the mid layer was not successfully predicted by the two models. This might be improved if quality velocity measurements were available for relaxation.

Anis and Singhal (2006) applied several models in a freshwater reservoir where current velocities were small. The CH model in their study well reproduced turbulence dynamics in the SBL, even though the current was not measured. Our simulations caught the trend of turbulence quantities in the SBL, albeit lower in magnitude due to the missing of current measurements. Models in *Anis and Singhal* (2006) were not able to reproduce χ and ϵ below the SBL, which might be due to the intermittency of turbulence and long relaxation time for temperature (1 hour). The failure of our simulations in the mid layer was more related to the lack of measured current velocities above 12.4 m and the low vertical resolution of measured currents below 12.4 m. Considering current speeds were as large as 0.4 m s^{-1}, the effect of

velocity was significant and can not be neglected. The CH model presented a better agreement between observations and simulations for χ and ϵ in the BBL than the SG model. The reasons might be that 1) for χ, the stability function ν_t' of *Cheng et al.* (2002) is more complete to represent turbulence processes than that of *Schumann and Gerz* (1995); 2) for ϵ, quality velocity measurements seem to be more required for the SG model than the CH model, thus the good agreement between the CH and SG models in Section 2 did not show here. The good agreement between observations and model simulations for ν_t' and ν_ρ' in the SBL in *Anis and Singhal* (2006) did not emerge in the present study either, indicating that current observations are required.

3.8 Conclusions

The experiment was characterized by low winds and calm surface waves. The SBL and BBL were well mixed during the 24 hours, while the pycnocline constrained vertical mixing in the mid layer. An enhanced mixing event was present in tracers' profiles in the mid layer between 2:00 and 5:00 (Figure 3.3), resulting in high turbulent activities (e.g. Figure 3.11). Currents were measured only below 12.4 m in a low vertical resolution (bin size 2 m) and measurements lower than 18.4 m were discarded due to side-lobe contamination. A bottom hypoxic layer was indicated by DO measurements, above which advection was found in the mid layer, causing enhanced turbulence activities in a shape of "stripe" in e.g. Figures 3.11 and 3.16. The estimate of time to remove the bottom hypoxia by turbulence would help to understand formation/deformation of hypoxia against shear, stratification, respiration, etc.

Two second-moment turbulence closure models, CH and SG, were applied for simulating turbulence quantities (χ, ϵ, ν_t', and ν_ρ'). At the surface, the models were forced with heat and momentum fluxes measured from different locations. Wind

speeds from the NDBC station LUML1 were likely higher than those in situ at site C around 8:00, which was proven from observed ϵ compared to modeled ϵ. In the water column, the models were relaxed to θ and S measurements, but not to velocities due to the low vertical resolution. The patterns of observed χ, ϵ, ν_t', and ν_ρ' followed the SBL defined for temperature, while those of modeled χ, ϵ, ν_t', and ν_ρ' followed the SBL defined for density. This was due to the incomplete measurements for velocity such that the models only rely on measured densities. Observed M^2 was not available in the BBL, however, both models presented agreements between modeled R_i and observed χ and ϵ.

Both models resulted in χ and ϵ values lower than those observed in the SBL, and failed to reproduce the turbulence quantities in the mid layer. Agreements between observations and models were shown in the BBL for CH modeled χ and ϵ, while the SG model predicted high values for both turbulence quantities.

Simulated ν_t' and ν_ρ' were regulated by c_μ' and N, respectively, and primarily showed higher model-observation correlations than those for χ and ϵ in all three layers. Both models presented similar results for mean value in the two boundary layers, but were all higher than those observed due to their incapability of modeling intermittent turbulence. The two models failed, similar to the results for χ and ϵ, to predict ν_t' and ν_ρ' in the mid layer.

The SG model simulated high χ and ν_t' values in the mid layer because the simplified stability functions of *Schumann and Gerz* (1995) can not account for stratifications in the pycnocline, thus the stability functions of *Cheng et al.* (2002) are more appropriate for model simulations in stable layers. The two models were not highly correlated in the BBL, although the difference between their mean values for any turbulence quantity was not as significant as what the ratio indicated. Fine-resolution measurements of current velocity are crucial for turbulence model simulations at a

location, e.g our study site, where the current is not negligible.

4. CONCLUSIONS

Seasonal bottom hypoxia is prevalent on the Texas-Louisiana continental shelf in Summer. It is the result of strong stratification that restricts downward transport of dissolved oxygen from the SBL. Turbulence is the mechanism for stratification destruction, enhancing vertical mixing through the pycnocline, thus studies of turbulence would help us to understand the physical dynamics in such an environment. A field campaign was conducted at two sites (C and D) of similar depth ($\sim$ 21 m) on the continental shelf in August 2005, and turbulent dynamics were investigated from turbulence quantities i.e. TKE, ϵ, τ, χ, ν_t', ν_ρ'.

ϵ, TKE, and τ were calculated from measurements in the BBL at site D. ϵ was estimated from vertical velocity measurements according to Kolmogorov's -5/3 law after removal of surface wave effects. TKE was calculated from the velocity variance estimated from the inertial subrange of energy spectrum of the vertical velocity component, and τ was estimated according to the law of the wall. Turbulence was not active in the BBL over the experiment, given that only 32.6% burst measurements showed clear inertial subranges in energy spectra of vertical velocity fluctuations.

χ, ϵ, ν_t', and ν_ρ' were calculated from measurements throughout the water column at site C. χ was estimated from integration of the temperature microstructure gradient spectra, ϵ was derived by fitting the Batchelor theoretical spectrum to the same spectrum, and ν_t' and ν_ρ' were calculated as functions of χ and ϵ, respectively. The four turbulence quantities indicate active turbulence processes in the SBL and BBL, as well as in the mid layer where shear stress was induced by advected non-local water.

One-dimensional one-point two-equation second-moment turbulence closure mod-

els were implemented for turbulence quantities simulations and were compared to observations. Four models were set as follows. CH: the turbulence closures $k-\epsilon$ with the stability functions of *Cheng et al.* (2002); SG: the turbulence closures $k-kL$ with the stability functions of *Schumann and Gerz* (1995); CHx: the turbulence closures $k-kL$ with the stability functions of *Cheng et al.* (2002); SGx: the turbulence closures $k-\epsilon$ with the stability functions of *Schumann and Gerz* (1995). The four models were forced by surface meteorological and hydrological data obtained from several sources including two NDBC stations, a US Forest Service weather station, and in situ measurements.

At site D, water was strongly stratified in the mid layer, suppressing vertical mixing, and surface fluxes had negligible effect on turbulence in the BBL, albeit a strong wind event increased current velocities and turbulence energy near the bottom. Relaxation to measured current, temperature, and salinity data were applied to the four models to improve turbulence simulations. In the BBL, all models reproduced ϵ, TKE, and τ determined from energy spectra of vertical velocity fluctuations. Comparisons between the four models showed that the models with the stability functions of *Schumann and Gerz* (1995) predicted higher values for ν related turbulence quantities compared to those with the stability functions of *Cheng et al.* (2002) in the mid layer, which might be due to that the former stability functions are not sensitive to buoyancy.

At site C, a non-local water layer with high-concentration DO was observed above the bottom hypoxic layer, inducing shear stress in the mid layer. The CH and SG models were applied for χ, ϵ, ν_t', and ν_ρ' estimations with the relaxation to temperature and salinity measurements. Elevated turbulence energy resulting from the advected non-local water layer was not well reproduced by the two models because high-resolution velocity measurements were not available as forcing for the simula-

tions. Modeled turbulence quantities only agreed with those observed in the BBL for χ and ϵ from the CH model, which might be due to that the stability functions of the CH model contain more complete physical processing terms than those of the SG model. Observed ν_t' and ν_ρ' emerged patchy patterns, and the two models were not capable of predicting intermittent turbulent activities. The SG model resulted in higher values of χ and ν_t' than the CH model in the mid layer due to the simplified stability functions of *Schumann and Gerz* (1995). This is consistent with the results from the study at site D. Complete high-resolution measurements of velocity throughout the water column would be required in order to improve the model simulations.

The physical conditions at the two sites were similar, except that the pycnocline at site C was more stratified than at site D, and BBL ϵ at site C was 2 orders of magnitude lower than that at site D on average. Bottom hypoxia was less likely to happen at site D, although we are unable to confirm this since measurements of DO were not carried out there. The present studies investigated turbulence dynamics affected by surface fluxes, wind waves, stratification, non-local water advection, and shear stress near the bottom. Second-moment turbulence closure models were applied, and simulated turbulence quantities were compared with those observed to test the capability of reproducing the turbulence activities. The non-local water with relatively high DO resulted in upward and downward turbulent oxygen fluxes at site C, and time to deform the bottom hypoxia by turbulence was estimated as 7.11 days. These works give us a better understanding for turbulence observation and turbulence modeling in a hypoxic zone.

REFERENCES

Adrian, R. (1991), Particle-imaging techniques for experimental fluid mechanics, *Annual Review of Fluid Mechanics*, *23*, 261–304.

Anis, A. (2006), Similarity relationships in the unstable aquatic surface layer, *Geophysical Research Letters*, *33*(19), doi:10.1029/2006gl027268.

Anis, A., and G. Singhal (2006), Mixing in the surface boundary layer of a tropical freshwater reservoir, *Journal of Marine Systems*, *63*(3-4), 225–243.

Appell, G. F., P. D. Bass, and M. A. Metcalf (1991), Acoustic doppler current profiler performance in near surface and bottom boundaries, *IEEE Journal of Oceanic Engineering*, *16*(4), 390–396, doi:10.1109/48.90903.

Arneborg, L., V. Fiekas, L. Umlauf, and H. Burchard (2007), Gravity current dynamics and entrainmenta process study based on observations in the arkona basin, *Journal of Physical Oceanography*, *37*(8), 2094–2113, doi:10.1175/JPO3110.1.

Baker, M. A., and C. H. Gibson (1987), Sampling turbulence in the stratified ocean: statistical consequences of strong intermittency, *Journal of Physical Oceanography*, *17*, 1817–1836, doi:10.1175/1520-0485(1987)017<1817:STITSO>2.0.CO;2.

Batchelor, G. K. (1959), Small-scale variation of convected quantities like temperature in turbulent fluid part 1. general discussion and the case of small conductivity, *Journal of Fluid Mechanics*, *5*(01), 113–133, doi:10.1017/S002211205900009X.

Baumert, H., and H. Peters (2000), Second-moment closures and length scales for weakly stratified turbulent shear flows, *Journal of Geophysical Research*, *105*(C3), 6453–6468, doi:10.1029/1999JC900329.

Baumert, H. Z., J. Simpson, and J. Sündermann (Eds.) (2005), *Marine Turbulence Theories Observations and Models*, 213 pp., Cambridge University Press, Cambridge, U.K.

Beaird, N., I. Fer, P. Rhines, and C. Eriksen (2012), Dissipation of turbulent kinetic energy inferred from seagliders: an application to the eastern nordic seas overflows, *Journal of Physical Oceanography*, *42*(12), 2268–2282, doi:10.1175/JPO-D-12-094.1.

Berg, P., H. Røy, F. Janssen, V. Meyer, B. Jørgensen, M. Huettel, and D. de Beer (2003), Oxygen uptake by aquatic sediments measured with a novel non-invasive eddy-correlation technique, *Marine Ecology Progress Series*, *261*, 75–83, doi: 10.3354/meps261075.

Bertuccioli, L., G. I. Roth, J. Katz, and T. R. Osborn (1999), A submersible particle image velocimetry system for turbulence measurements in the bottom boundary layer, *Journal of Atmospheric and Oceanic Technology*, *16*, 1635–1646, doi: 10.1175/1520-0426(1999)016<1635:ASPIVS>2.0.CO;2.

Bianchi, T. S., S. F. DiMarco, J. H. C. Jr., R. D. Hetland, P. Chapman, J. W. Day, and M. A. Allison (2010), The science of hypoxia in the northern gulf of mexico: a review, *Science of the Total Environment*, *408*(7), 1471–1484, doi: 10.1016/j.scitotenv.2009.11.047.

Bluteau, C. E., N. L. Jones, and G. N. Ivey (2011), Estimating turbulent kinetic energy dissipation using the inertial subrange method in environmental flows, *Limnology and Oceanography: Methods*, *9*, 302–321, doi:10.4319/lom.2011.9.302.

Bolding, K., H. Burchard, T. Pohlmann, and A. Stips (2002), Turbulent mixing

in the northern north sea: a numerical model study, *Continental Shelf Research*, *22*(18-19), 2707–2724, doi:DOI: 10.1016/S0278-4343(02)00122-X.

Bourgault, D., D. E. Kelley, and P. S. Galbraith (2008), Turbulence and boluses on an internal beach, *Journal of Marine Research*, *66*(5), 563–588, doi:10.1357/002224008787536835.

Boussinesq, J. (1903), Sur un mode simple d'écoulement des nappes d'eau d'infiltration à lit horizontal, avec rebord vertical tout autour lorsqu'une partie de ce rebord est enlevée depuis la surface jusqu'au fond, *Comptes Rendus de l'Acad'émie des Sciences*, *137*, 5–11.

Burchard, H. (1999), Recalculation of surface slopes as forcing for numerical water column models of tidal flow, *Applied Mathematical Modelling*, *23*(10), 737–755, doi:10.1016/S0307-904X(99)00008-6.

Burchard, H. (2001a), On the q^2l equation by Mellor and Yamada (1982), *Journal of Physical Oceanography*, *31*(5), 1377–1387, doi:10.1175/1520-0485(2001)031<1377:OTQLEB>2.0.CO;2.

Burchard, H. (2001b), Simulating the wave-enhanced layer under breaking surface waves with two-equation turbulence models, *Journal of Physical Oceanography*, *31*, 3133–3145, doi:10.1175/1520-0485(2001)031<3133:STWELU>2.0.CO;2.

Burchard, H. (2002), *Applied Turbulence Modelling in Marine Waters*, 215 pp., Springer, New York, U.S.A.

Burchard, H., and H. Baumert (1995), On the performance of a mixed-layer model based on the $k-\epsilon$ turbulence closure, *Journal of Geophysical Research*, *100*(C5), 8523–8540, doi:10.1029/94jc03229.

Burchard, H., and K. Bolding (2001), Comparative analysis of four second-moment turbulence closure models for the oceanic mixed layer, *Journal of Physical Oceanography*, *31*(8), 1943–1968, doi:10.1175/1520-0485(2001)031<1943:CAOFSM>2.0.CO;2.

Burchard, H., O. Petersen, and T. P. Rippeth (1998), Comparing the performance of the Mellor-Yamada and the $k - \epsilon$ two-equation turbulence models, *Journal of Geophysical Research*, *103*(C5), 10,543–10,554, doi:10.1029/98JC00261.

Burchard, H., K. Bolding, and M. R. Villarreal (1999), GOTM - a general ocean turbulence model. theory, applications and test cases, *European Commission*, *EUR 18745 EN*.

Burchard, H., K. Bolding, T. P. Rippeth, A. Stips, J. H. Simpson, and J. Sundermann (2002), Microstructure of turbulence in the northern north sea: a comparative study of observations and model simulations, *Journal of Sea Research*, *47*(3-4), 223–238, doi:10.1016/S1385-1101(02)00126-0.

Burchard, H., K. Bolding, W. Kühn, A. Meister, T. Neumann, and L. Umlauf (2006), Description of a flexible and extendable physicalbiogeochemical model system for the water column, *Journal of Marine Systems*, *61*(3-4), 180–211, doi: 10.1016/j.jmarsys.2005.04.011.

Burchard, H., P. D. Craig, J. R. Gemmrich, H. Van Haren, P. P. Mathieu, H. E. M. Meier, W. A. M. N. Smith, H. Prandke, T. P. Rippeth, E. D. Skyllingstad, W. D. Smyth, D. J. S. Welsh, and H. W. Wijesekera (2008), Observational and numerical modeling methods for quantifying coastal ocean turbulence and mixing, *Progress in Oceanography*, *76*(4), 399–442, doi:10.1016/j.pocean.2007.09.005.

Burchard, H., F. Janssen, K. Bolding, L. Umlauf, and H. Rennau (2009), Model simulations of dense bottom currents in the western baltic sea, *Continental Shelf Research*, *29*(1), 205–220, doi:10.1016/j.csr.2007.09.010.

Cabrillo, R. S., C. González-Pola, M. Ruiz-Villarreal, and A. L. Montero (2011), Mixed layer depth (MLD) variability in the southern bay of biscay. deepening of winter mlds concurrent with generalized upper water warming trends?, *Ocean Dynamics*, *61*(9), 1215–1235, doi:10.1007/s10236-011-0407-6.

Canuto, V. M., A. Howard, Y. Cheng, and M. S. Dubovikov (2001), Ocean turbulence. part i: One-point closure model-momentum and heat vertical diffusivities, *Journal of Physical Oceanography*, *31*, 1413–1426, doi:10.1175/1520-0485(2001)031<1413:OTPIOP>2.0.CO;2.

Chatterjee, S., and A. S. Hadi (1986), Influential observations, high leverage points, and outliers in linear regression, *Statistical Science*, *1*, 379–393.

Chen, H.-L., M. Hondzo, and A. R. Rao (2002), Segmentation of temperature microstructure, *Journal of Geophysical Research*, *107*(C12), 3211, doi:10.1029/2001JC001009.

Cheng, Y., V. M. Canuto, and A. M. Howard (2002), An improved model for the turbulent PBL, *Journal of the Atmospheric Sciences*, *59*(9), 1550–1565, doi:10.1175/1520-0469(2002)059<1550:AIMFTT>2.0.CO;2.

Clayson, C. A., and L. H. Kantha (1999), Turbulent kinetic energy and its dissipation rate in the equatorial mixed layer, *Journal of Physical Oceanography*, *29*(9), 2146–2166, doi:10.1175/1520-0485(1999)029<2146:TKEAID>2.0.CO;2.

Cousins, M., M. Stacey, and J. Drake (2010), Effects of seasonal stratification on

turbulent mixing in a hypereutrophic coastal lagoon, *Limnology and Oceanography*, *55*(1), 172–186.

Cuypers, Y., P. Bouruet-Aubertot, C. Marec, and J.-L. Fuda (2011), Characterization of turbulence and validation of fine-scale parametrization in the mediterranean sea during boum experiment, *Biogeosciences Discussions*, *8*(5), 8961–8998, doi:10.5194/bgd-8-8961-2011.

Dagg, M., J. Ammerman, R. Amon, W. Gardner, R. Green, and S. Lohrenz (2007), A review of water column processes influencing hypoxia in the northern gulf of mexico, *Estuaries and Coasts*, *30*(5), 735–752, doi:10.1007/BF02841331.

Dale, V. H., C. L. Kling, J. L. Meyer, J. Sanders, H. Stallworth, T. Armitage, D. Wangsness, T. Bianchi, A. Blumberg, W. Boynton, D. J. Conley, W. Crumpton, M. David, D. Gilbert, R. W. Howarth, R. Lowrance, K. Mankin, J. Opaluch, H. Paerl, K. Reckhow, A. N. Sharpley, T. W. Simpson, C. S. Snyder, and D. Wright (2010), *Hypoxia in the Northern Gulf of Mexico*, 284 pp., Springer, New York, U.S.A., doi:10.1007/978-0-387-89686-1.

Davis, K. A., and S. G. Monismith (2011), The modication of bottom boundary layer turbulence and mixing by internal waves shoaling on a barrier reef, *Journal of Physical Oceanography*, *41*, 2223–2241, doi:10.1175/2011JPO4344.1.

Dewey, R. K., W. R. Crawford, A. E. Gargett, and N. S. Oakey (1987), A microstructure instrument for profiling oceanic turbulence in coastal bottom boundary layers, *Journal of Atmospheric and Oceanic Technology*, *4*(2), 288–297.

Dickey, T. D., D. V. Manov, R. A. Weller, and D. A. Siegel (1994), Determination of longwave heat flux at the air-sea interface using measurements from buoy

platforms, *Journal of Atmospheric and Oceanic Technology*, *11*(4), 1057–1078, doi:10.1175/1520-0426(1994)011<1057:DOLHFA>2.0.CO;2.

Dillon, T. M., and D. R. Caldwell (1980), The Batchelor spectrum and dissipation in the upper ocean, *Journal of Geophysical Research*, *85*(9), 1910–1916, doi:10.1029/JC085iC04p01910.

Doron, P., L. Bertuccioli, J. Katz, and T. R. Osborn (2001), Turbulence characteristics and dissipation estimates in the coastal ocean bottom boundary layer from PIV data, *Journal of Physical Oceanography*, *31*, 2108–2134, doi:10.1175/1520-0485(2001)031<2108:TCADEI>2.0.CO;2.

DuMouchel, W., and F. O'Brien (1991), Computing and graphics in statistics, pp. 41–48, Springer-Verlag, New York, U.S.A.

Emery, W. J., and R. E. Thomson (2001), *Data analysis methods in physical oceanography*, second ed., 654 pp., Elsevier, Amsterdam, Netherlands.

Fairall, C., E. Bradley, and J. Hare (2003), Bulk parameterization of air-sea fluxes: updates and verification for the COARE algorithm, *Journal of Climate*, pp. 571–591.

Fairall, C. W., E. F. Bradley, D. P. Rogers, J. B. Edson, and G. S. Young (1996), Bulk parameterization of air-sea fluxes for tropical ocean-global atmosphere coupled-ocean atmosphere response experiment, *Journal of Geophysical Research*, *101*(C2), 3747–3764, doi:10.1029/95JC03205.

Gerz, T., U. Schumann, and S. E. Elghobashi (1989), Direct numerical simulation of stratified homogeneous turbulent shear flows, *Journal of Fluid Mechanics*, *200*, 563–594, doi:10.1017/S0022112089000765.

Grant, H. L., R. W. Stewart, and A. Moilliet (1962), Turbulence spectra from a tidal channel, *Journal of Fluid Mechanics*, *12*(02), 241–268, doi: 10.1017/S002211206200018X.

Grant, H. L., B. A. Hughes, W. M. Vogel, and A. Moilliet (1968), The spectrum of temperature fluctuations in turbulent flow, *Journal of Fluid Mechanics*, *34*(03), 423–442, doi:10.1017/S0022112068001990.

Grant, W. D., and O. S. Madsen (1986), The continental-shelf bottom boundary layer, *Annual Review of Fluid Mechanics*, *18*(1), 265–305.

Gross, T. F., and A. R. M. Nowell (1985), Spectral scaling in a tidal boundary layer, *Journal of Physical Oceanography*, *15*, 496–508, doi:10.1175/1520-0485(1985)015<0496:SSIATB>2.0.CO;2.

Hackett, E. E., L. Luznik, A. R. Nayak, J. Katz, and T. R. Osborn (2011), Field measurements of turbulence at an unstable interface between current and wave bottom boundary layers, *Journal of Geophysical Research*, *116*(C2), C02,022, doi: 10.1029/2010JC006138.

Haltiner, G. J., and R. T. Williams (Eds.) (1980), *Numerical prediction and dynamic meteorology*, second ed., xvii, 477 pp., Wiley, New Jersey, U.S.A.

He, H., and D. Chen (2011), Effects of surface wave breaking on the oceanic boundary layer, *Geophysical Research Letters*, *38*(7), doi:10.1029/2011gl046665.

Hofmeister, R., H. Burchard, and K. Bolding (2009), A three-dimensional model study on processes of stratification and de-stratification in the limfjord, *Continental Shelf Research*, *29*(11-12), 1515–1524, doi:10.1016/j.csr.2009.04.004.

Imberger, J., and G. N. Ivey (1991), On the nature of turbulence in a stratified fluid. part ii: application to lakes, *Journal of Physical Oceanography*, *21*, 659–680, doi:10.1175/1520-0485(1991)021<0659:OTNOTI>2.0.CO;2.

Inoue, T., Y. Nakamura, and M. Sayama (2008), A new method for measuring flow structure in the benthic boundary layer using an acoustic doppler velocimeter, *Journal of Atmospheric and Oceanic Technology.*, *25*, 822–830, doi: 10.1175/2007JTECHO531.1.

Ivey, G., K. Winters, and J. Koseff (2008), Density stratification, turbulence, but how much mixing?, *Annual Review of Fluid Mechanics*, *40*(1), 169–184, doi: 10.1146/annurev.fluid.39.050905.110314.

Jacobitz, F. G., S. Sarkar, and C. W. van Atta (1997), Direct numerical simulations of the turbulence evolution in a uniformly sheared and stably stratified flow, *Journal of Fluid Mechanics*, *342*, 231–261.

Jonas, T., A. Stips, W. Eugster, and A. Wüest (2003), Observations of a quasi shear-free lacustrine convective boundary layer: stratification and its implications on turbulence, *Journal of Geophysical Research*, *108*, 3328–3342, doi: 10.1029/2002JC001440.

Jurado, E., H. J. van der Woerd, and H. A. Dijkstra (2012), Microstructure measurements along a quasi-meridional transect in the northeastern atlantic ocean, *Journal of Geophysical Research*, *117*(C4), C04,016, doi:10.1029/2011JC007137.

Kantha, L. H., and C. A. Clayson (1994), An improved mixed layer model for geophysical applications, *Journal of Geophysical Research*, *99*, 25,235–25,266.

Klein, P., and G. Lapeyre (2009), The oceanic vertical pump induced by mesoscale

and submesoscale turbulence, *Annual Review of Marine Science*, *1*(1), 351–375, doi:10.1146/annurev.marine.010908.163704.

Kocsis, O., H. Prandke, A. Stips, A. Simon, and A. Wüest (1999), Comparison of dissipation of turbulent kinetic energy determined from shear and temperature microstructure, *Journal of Marine Systems*, *21*(1-4), 67–84, doi:10.1016/S0924-7963(99)00006-8.

Kolmogorov, A. N. (1941), Dissipation of energy in the locally isotropic turbulence, *Doklady Akademii Nauk*, *31*, 538–540.

Kraus, N. C., A. Lohrmann, and R. Cabrera (1994), New acoustic meter for measuring 3d laboratory flows, *Journal of Hydraulic Engineering*, *120*(3), 406–412, doi:10.1061/(ASCE)0733-9429(1994)120:3(406).

Kubota, M., N. Iwabe, M. F. Cronin, and H. Tomita (2008), Surface heat fluxes from the ncep/ncar and ncep/doe reanalyses at the kuroshio extension observatory buoy site, *Journal of Geophysical Research*, *113*, C02,009, doi:10.1029/2007JC004338.

Kundu, P. K., and I. M. Cohen (Eds.) (2008), *Fluid mechanics*, fourth ed., xxviii, 872 pp., Academic Press.

Lane, S. N., P. M. Biron, K. F. Bradbrook, J. B. Butler, J. H. Chandler, M. D. Crowell, S. J. McLelland, K. S. Richards, and A. G. Roy (1998), Three-dimensional measurement of river channel flow processes using acoustic doppler velocimetry, *Earth Surface Processes and Landforms*, *23*(13), 1247–1267, doi:10.1002/(SICI)1096-9837(199812)23:13<1247::AID-ESP930>3.0.CO;2-D.

Large, W. G., and S. Pond (1981), Open ocean momentum flux measurements in

moderate to strong winds, *Journal of Physical Oceanography*, *11*(3), 324–336, doi:10.1175/1520-0485(1981)011<0324:OOMFMI>2.0.CO;2.

Launder, B. E., and D. B. Spalding (Eds.) (1972), *Mathematical Models of Turbulence*, 169 pp., Academic Press, Massachusetts, U.S.A.

Lee, G.-H. (2003), Spectral estimates of bed shear stress using suspended-sediment concentrations in a wave-current boundary layer, *Journal of Geophysical Research*, *108*(C7), 3208, doi:10.1029/2001JC001279.

Lesieur, M. (2008), *Turbulence in Fluids*, Springer, New York, U.S.A.

Liu, S., C. Meneveau, and J. Katz (1994), On the properties of similarity subgrid-scale models as deduced from measurements in a turbulent jet, *Journal of Fluid Mechanics*, *275*, 83–119, doi:10.1017/S0022112094002296.

Liu, Y., M. A. Evans, and D. Scavia (2010), Gulf of mexico hypoxia: exploring increasing sensitivity to nitrogen loads, *Environmental Science & Technology*, *44*(15), 5836–5841, doi:10.1021/es903521n.

Lopez, F., and M. H. Garcia (2001), Mean flow and turbulence structure of open-channel flow through non-emergent vegetation, *Journal of Hydraulic Engineering*, *127*(5), 392–402, doi:10.1061/(ASCE)0733-9429(2001)127:5(392).

Lorke, A., and A. Wüest (2005), Application of coherent ADCP for turbulence measurements in the bottom boundary layer, *Journal of Atmospheric and Oceanic Technology*, *22*(11), 1821–1828, doi:10.1175/JTECH1813.1.

Lu, Y., R. G. Lueck, and D. Huang (2000), Turbulence characteristics in a tidal channel, *Journal of Physical Oceanography*, *30*, 855–867, doi:10.1175/1520-0485(2000)030<0855:TCIATC>2.0.CO;2.

Lueck, R., and D. Huang (1999), Dissipation measurement with a moored instrument in a swift tidal channel, *Journal of Atmospheric and Oceanic Technology*, *16*, 1499–1505, doi:10.1175/1520-0426(1999)016<1499:DMWAMI>2.0.CO;2.

Lueck, R., F. Wolk, and H. Yamazaki (2002), Oceanic velocity microstructure measurements in the 20th century, *Journal of Oceanography*, *58*(1), 153–174, doi:10.1023/A:1015837020019.

Lumley, J. L., and E. A. Terray (1983), Kinematics of turbulence convected by a random wave field, *Journal of Physical Oceanography*, *13*(11), 2000–2007, doi:10.1175/1520-0485(1983)013<2000:KOTCBA>2.0.CO;2.

MacIntyre, S., K. M. Flynn, R. Jellison, and J. R. J. Romero (1999), Boundary mixing and nutrient fluxes in Mono Lake, California, *Limnology and Oceanography*, *44*(3), 512–529, doi:10.4319/lo.1999.44.3.0512.

Mason, P. J. (1994), Large-eddy simulation: a critical review of the technique, *Quarterly Journal of the Royal Meteorological Society*, *120*(515), 1–26, doi:10.1002/qj.49712051503.

McPhee, M. G. (1998), An inertial-dissipation method for estimating turbulent flux in buoyancy-driven, convective boundary layers, *Journal of Geophysical Research*, *103*, 3249–3255, doi:10.1029/97JC02263.

Mellor, G. L., and T. Yamada (1974), A hierarchy of turbulence closure models for planetary boundary layers, *Journal of the Atmospheric Sciences*, *31*(7), 1791–1806, doi:10.1175/1520-0469(1974)031<1791:AHOTCM>2.0.CO;2.

Mellor, G. L., and T. Yamada (1982), Development of a turbulence closure model

for geophysical fluid problems, *Reviews of Geophysics*, *20*(4), 851–875, doi: 10.1029/RG020i004p00851.

Meneveau, C., and J. Katz (2000), Scale-invariance and turbulence models for large-eddy simulation, *Annual Review of Fluid Mechanics*, *32*(1), 1–32, doi: 10.1146/annurev.fluid.32.1.1.

Moin, P., and K. Mahesh (1998), Direct numerical simulation: a tool in turbulence research, *Annual Review of Fluid Mechanics*, *30*(1), 539–578, doi: 10.1146/annurev.fluid.30.1.539.

Molen, J., J. N. Aldridge, C. Coughlan, E. R. Parker, D. Stephens, and P. Ruardij (2012), Modelling marine ecosystem response to climate change and trawling in the north sea, *Biogeochemistry*, doi:10.1007/s10533-012-9763-7.

Moum, J. N. (1996), Energy-containing scales of turbulence in the ocean thermocline, *Journal of Geophysical Research: Oceans*, *101*(C6), 14,095–14,109, doi: 10.1029/96JC00507.

Muste, M., K. Yu, T. Pratt, and D. Abraham (2004), Practical aspects of ADCP data use for quantification of mean river flow characteristics; part II: fixed-vessel measurements, *Flow Measurement and Instrumentation*, *15*(1), 17–28, doi: 10.1016/j.flowmeasinst.2003.09.002.

Nash, J. D., M. H. Alford, E. Kunze, K. Martini, and S. Kelly (2007), Hotspots of deep ocean mixing on the Oregon continental slope, *Geophysical Research Letters*, *34*(1), L01,605, doi:10.1029/2006GL028170.

Nystrom, E. A., K. A. Oberg, and C. R. Rehmann (2002), Measurement of turbulence with acoustic doppler current profilers - sources of error and laboratory

results, *Hydraulic Measurements and Experimental Methods 2002*, pp. 1–10, doi: 10.1061/40655(2002)55.

Nystrom, E. A., C. R. Rehmann, and K. A. Oberg (2007), Evaluation of mean velocity and turbulence measurements with adcps, *Journal of Hydraulic Engineering*, *133*(12), 1310–1318, doi:10.1061/(ASCE)0733-9429(2007)133:12(1310).

Oakey, N. S. (1982), Determination of the rate of dissipation of turbulent energy from simultaneous temperature and velocity shear microstructure measurements, *Journal of Physical Oceanography*, *12*, 256–271, doi:10.1175/1520-0485(1982)012<0256:DOTROD>2.0.CO;2.

Osborn, T. R. (1980), Estimates of the local rate of vertical dissipation from dissipation measurements, *Journal of Physical Oceanography*, *10*, 83–89.

Palmer, M. R., J. a. Polton, M. E. Inall, T. P. Rippeth, J. A. M. Green, J. Sharples, J. H. Simpson, and M. Green (2013), Variable behavior in pycnocline mixing over shelf seas, *Geophysical Research Letters*, *40*(1), 161–166, doi: 10.1029/2012GL054638.

Payne, R. E. (1972), Albedo of the sea surface, *Journal of the Atmospheric Sciences*, *29*, 959–970, doi:10.1175/1520-0469(1972)029<0959:AOTSS>2.0.CO;2.

Perlin, A. (2005), Response of the bottom boundary layer over a sloping shelf to variations in alongshore wind, *Journal of Geophysical Research*, *110*(C10), C10S09, doi:10.1029/2004JC002500.

Perlin, A., J. N. Moum, J. M. Klymak, M. D. Levine, T. Boyd, and P. M. Kosro (2005), A modified law-of-the-wall applied to oceanic bottom boundary layers, *Journal of Geophysical Research*, *110*(C10), C10S10, doi:10.1029/2004JC002310.

Peters, H., and H. Z. Baumert (2007), Validating a turbulence closure against estuarine microstructure measurements, *Ocean Modelling*, *19*(3-4), 183–203, doi: 10.1016/j.ocemod.2007.07.002.

Peters, H., M. C. Gregg, and S. T. B. (1995), Detail and scaling of turbulent overturning in the pacific equatorial undercurrent, *Journal of Geophysical Research*, *100*, 18,333–18,348.

Pope, S. B. (Ed.) (2000), *Turbulent Flows*, 771 pp., Cambridge University Press, Cambridge, U.K.

Prandke, H., K. Holtsch, and A. Stips (2000), Mitec technology development: the microstructure/turbulence measuring system MSS, *European Commission*, *EUR 19733 EN*, 75.

Rabalais, N., R. Turner, B. Sen Gupta, D. Boesch, P. Chapman, and M. Murrell (2007), Hypoxia in the northern Gulf of Mexico: does the science support the plan to reduce, mitigate, and control hypoxia?, *Estuaries and Coasts*, *30*(5), 753–772.

Rabalais, N. N., R. E. Turner, and W. J. Wiseman (2002), Gulf of Mexico hypoxia, A.K.A. "the dead zone", *Annual Review of Ecology and Systematics*, *33*(1), 235–263, doi:10.1146/annurev.ecolsys.33.010802.150513.

Rainville, L., and R. Pinkel (2001), Wirewalker: An autonomous wave-powered vertical profiler, *Journal of Atmospheric and Oceanic Technology*, *18*(6), 1048–1051, doi:10.1175/1520-0426(2001)018<1048:WAAWPV>2.0.CO;2.

Reynolds, O. (1895), On the dynamical theory of incompressible viscous fluids and the determination of the criterion, *Philosophical Transactions of the Royal Society of London*, *186*(1895).

Richards, C., D. Bourgault, P. S. Galbraith, A. Hay, and D. E. Kelley (2013), Measurements of shoaling internal waves and turbulence in an estuary, *Journal of Geophysical Research: Oceans*, *118*(October 2012), 1–14, doi:10.1029/2012JC008154.

Rippeth, T. P., E. Williams, and J. H. Simpson (2002), Reynolds stress and turbulent energy production in a tidal channel, *Journal of Physical Oceanography*, *32*, 1242–1251, doi:10.1175/1520-0485(2002)032<1242:RSATEP>2.0.CO;2.

Rippeth, T. P., J. H. Simpson, and E. Williams (2003), Measurement of the rates of production and dissipation of turbulent kinetic energy in an energetic tidal flow: Red Wharf Bay revisited, *Journal of Physical Oceanography*, *33*, 1889–1901, doi:10.1175/1520-0485(2003)033<1889:MOTROP>2.0.CO;2.

Rodi, W. (1987), Examples of calculation methods for flow and mixing in stratified fluids, *Journal of Geophysical Research*, *92*, 5305–5328, doi:10.1029/JC092iC05p05305.

Ruddick, B., A. Anis, and K. Thompson (2000), Maximum likelihood spectral fitting: the batchelor spectrum, *Journal of Atmospheric and Oceanic Technology*, *17*(11), 1541–1555, doi:10.1175/1520-0426(2000)017<1541:MLSFTB>2.0.CO;2.

Schumann, U., and T. Gerz (1995), Turbulent mixing in stably stratified shear flows, *Journal of Applied Meteorology*, *34*, 33–48, doi:10.1175/1520-0450-34.1.33.

Sharples, J., C. M. Moore, and E. R. Abraham (2001), Internal tide dissipation, mixing, and vertical nitrate flux at the shelf edge of ne new zealand, *Journal of Geophysical Research: Oceans*, *106*(C7), 14,069–14,081, doi:10.1029/2000JC000604.

Simpson, J. H., W. R. Crawford, T. P. Rippeth, A. R. Campbell, and J. V. S. Cheok (1996), The vertical structure of turbulent dissipation in

shelf seas, *Journal of Physical Oceanography*, *26*, 1579–1590, doi:10.1175/1520-0485(1996)026<1579:TVSOTD>2.0.CO;2.

Simpson, J. H., H. Burchard, N. R. Fisher, and T. P. Rippeth (2002), The semi-diurnal cycle of dissipation in a ROFI: model-measurement comparisons, *Continental Shelf Research*, *22*(11-13), 1615–1628, doi:10.1016/S0278-4343(02)00025-0.

Skyllingstad, E. D., W. D. Smyth, J. N. Moum, and H. Wijesekera (1999), Upper-ocean turbulence during a westerly wind burst: a comparison of large-eddy simulation results and microstructure measurements, *Journal of Physical Oceanography*, *29*(1), 5–28, doi:10.1175/1520-0485(1999)029<0005:UOTDAW>2.0.CO;2.

Smith, W., J. Katz, and T. Osborn (2005), On the structure of turbulence in the bottom boundary layer of the coastal ocean, *Journal of Physical Oceanography*, *35*(1), 72–93.

Smith, W. N., P. Atsavapranee, J. Katz, and T. Osborn (2002), PIV measurements in the bottom boundary layer of the coastal ocean, *Experiments in Fluids*, *33*(6), 962–971, doi:10.1007/s00348-002-0490-z.

Smyth, W. D., J. N. Moum, and D. R. Caldwell (2001), The efficiency of mixing in turbulent patches: inferences from direct simulations and microstructure observations, *Journal of Physical Oceanography*, *31*(8), 1969–1992, doi:10.1175/1520-0485(2001)031<1969:TEOMIT>2.0.CO;2.

Spiegel, E. A., and G. Veronis (1960), On the Boussinesq approximation for a compressible fluid, *Astrophysical Journal*, *11*, 442–447.

Sreenivasan, K. R. (1995), On the universality of the Kolmogorov constant, *Physical Review E*, *7*(11), 2778.

Stacey, M. T., S. G. Monismith, and J. R. Burau (1999a), Measurements of Reynolds stress profiles in unstratified tidal flow, *Journal of Geophysical Research*, *104*, 10,933–10,949, doi:10.1029/1998JC900095.

Stacey, M. T., S. G. Monismith, and J. R. Burau (1999b), Observations of turbulence in a partially stratified estuary, *Journal of Physical Oceanography*, *29*, 1950–1970.

Stips, A., H. Burchard, K. Bolding, and W. Eifler (2002), Modelling of convective turbulence with a two-equation $k-\epsilon$ turbulence closure scheme, *Ocean Dynamics*, *52*, 153–168, doi:doi:10.1007/s10236-002-0019-2.

Stips, A., H. Burchard, K. Bolding, H. Prandke, A. Simon, and A. Wüest (2005), Measurement and simulation of viscous dissipation in the wave affected surface layer, *Deep Sea Research Part II: Topical Studies in Oceanography*, *52*(9-10), 1133–1155, doi:10.1016/j.dsr2.2005.01.012.

Sun, B., L. Yu, and R. A. Weller (2003), Comparisons of surface meteorology and turbulent heat fluxes over the atlantic: NWP model analyses versus moored buoy observations, *Journal of Climate*, *16*, 679–695, doi:10.1175/1520-0442(2003)016<0679:COSMAT>2.0.CO;2.

Taylor, G. I. (1938), The spectrum of turbulence, *Proceedings of the Royal Society A: Mathematical, Physical and Engineering Sciences*, *164*(919), 476–490, doi:10.1098/rspa.1938.0032.

Tennekes, H., and J. L. Lumley (1972), *A First Course in Turbulence*, 300 pp., MIT Press, Massachusetts, U.S.A.

Thorpe, S. (2004), Recent developments in the study of ocean turbu-

lence, *Annual Review of Earth and Planetary Sciences*, *32*(1), 91–109, doi: 10.1146/annurev.earth.32.071603.152635.

Thorpe, S. A. (2005), *The Turbulent Ocean*, 439 pp., Cambridge University Press, Cambridge, U. K.

Trowbridge, J., and S. Elgar (2001), Turbulence measurements in the surf zone, *Journal of Physical Oceanography*, pp. 2403–2417.

Trowbridge, J. H., W. R. Geyer, C. A. Butman, and R. J. Chapman (1989), The 17-meter flume at the coastal research laboratory. part II: flow characteristics, *Technology Report*, *WHOI-89-11 (CRC-89-3)*, 37.

Umlauf, L., and H. Burchard (2003), A generic length-scale equation for geophysical turbulence models, *Journal of Marine Research*, *61*, 235–265, doi: 10.1357/002224003322005087.

Umlauf, L., and H. Burchard (2005), Second-order turbulence closure models for geophysical boundary layers. a review of recent work, *Continental Shelf Research*, *25*(7-8), 795–827, doi:10.1016/j.csr.2004.08.004.

Vallis, G. K. (Ed.) (2006), *Atmospheric and oceanic fluid dynamics : fundamentals and large-scale circulation*, xxv, 745 pp., Cambridge University Press, Cambridge, U.K.

Verspecht, F., T. P. Rippeth, M. J. Howarth, a. J. Souza, J. H. Simpson, and H. Burchard (2009), Processes impacting on stratification in a region of freshwater influence: application to Liverpool Bay, *Journal of Geophysical Research*, *114*(C11), C11,022, doi:10.1029/2009JC005475.

Voulgaris, G., and J. H. Trowbridge (1998), Evaluation of the acoustic doppler velocimeter (ADV) for turbulence measurements, *Journal of Atmospheric and Oceanic Technology.*, *15*, 272–289, doi:10.1175/1520-0426(1998)015<0272:EOTADV>2.0.CO;2.

Wager, T. D., M. C. Keller, S. C. Lacey, and J. Jonides (2005), Increased sensitivity in neuroimaging analyses using robust regression, *NeuroImage*, *26*(1), 99–113, doi:10.1016/j.neuroimage.2005.01.011.

Walker, N. D., W. J. Wiseman, L. J. Rouse, and A. Babin (2005), Effects of river discharge, wind stress, and slope eddies on circulation and the satellite-observed structure of the Mississippi River plume, *Journal of Coastal Research*, *21*(6), 1228–1244, doi:10.2112/04-0347.1.

Wang, B., S. N. Giddings, O. B. Fringer, E. S. Gross, D. A. Fong, and S. G. Monismith (2011), Modeling and understanding turbulent mixing in a macrotidal salt wedge estuary, *Journal of Geophysical Research*, *116*, C02,036, doi:10.1029/2010JC006135.

Warner, J. C., C. R. Sherwood, H. G. Arango, and R. P. Signell (2005), Performance of four turbulence closure models implemented using a generic length scale method, *Ocean Modelling*, *8*(1-2), 81–113, doi:10.1016/j.ocemod.2003.12.003.

Wolk, F., H. Yamazaki, L. Seuront, and R. G. Lueck (2002), A new free-fall profiler for measuring biophysical microstructure, *Journal of Atmospheric and Oceanic Technology.*, *19*, 780–793, doi:10.1175/1520-0426(2002)019<0780:ANFFPF>2.0.CO;2.

Zhang, J. A., and W. M. Drennan (2012), An observational study of vertical eddy

diffusivity in the hurricane boundary layer, *Journal of the Atmospheric Sciences*, *69*(11), 3223–3236, doi:10.1175/JAS-D-11-0348.1.

APPENDIX A

VERIFICATION OF THE STRONG WIND EVENT AT SITE D

Since NDBC 42035 is far from site D (90 km), the applicability of NDBC measurements for model simulations at site D was verified. The strong wind event happened at NDBC 42035 around 4:00 on Aug. 22, its pass over site D was indicated by the SST measured from the surface HOBO and the water pressure from the ADV (Figure A.1): the SST declined faster after 2:26, and the pressure presented a reverse temporal gradient after 2:00.

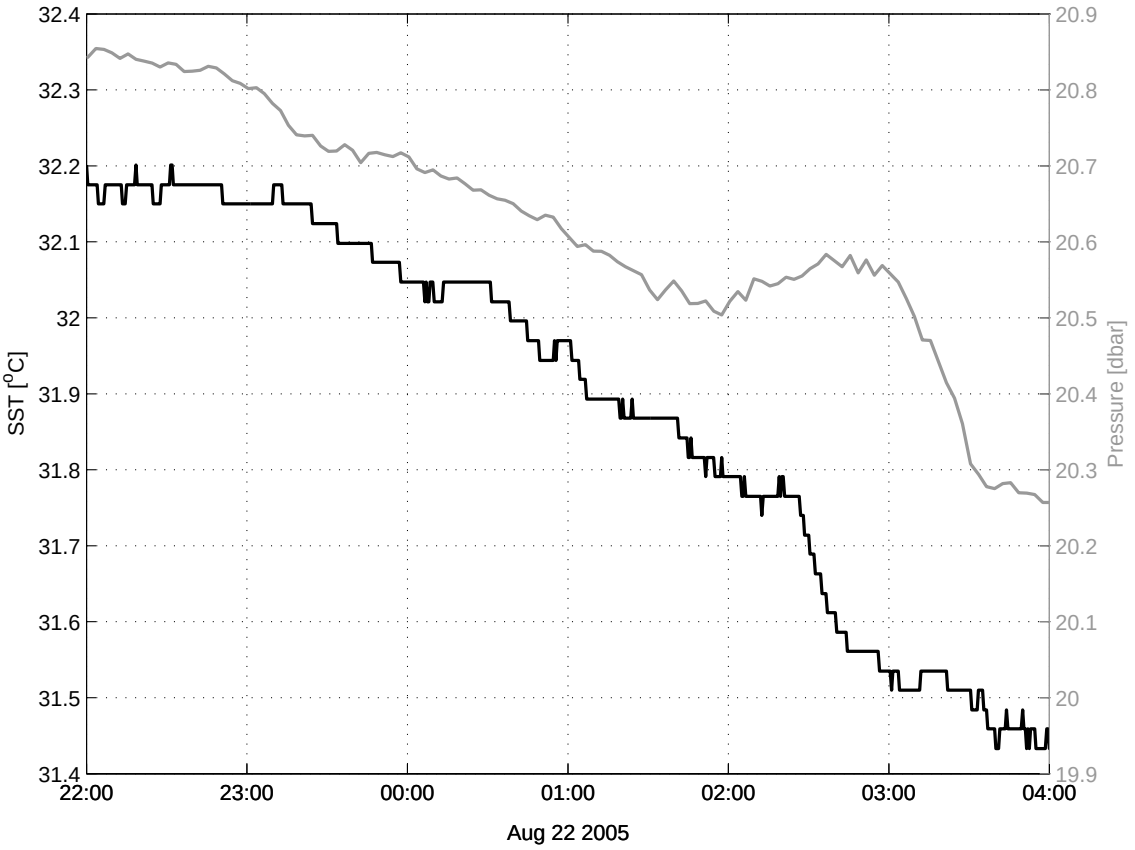

Figure A.1: The storm was revealed by the faster SST decrease from the HOBO after Aug 22 2:26 (black) and the reverse temporal pressure gradient from the ADV after Aug 22 2:00 (gray).

APPENDIX B

STABILITY FUNCTIONS

The stability functions, c_μ and c'_μ, of *Cheng et al.* (2002) are given by

$$c_\mu = \frac{0.107 + 0.019\alpha_N - 0.00018\alpha_M}{A}, \tag{B.1}$$

$$c'_\mu = \frac{0.1208 + 0.004376\alpha_N + 0.000548\alpha_M}{A}, \tag{B.2}$$

where

$$\begin{aligned} A =& 1 + 0.2826\alpha_N + 0.02816\alpha_M + 0.008927\alpha_N^2 + \\ & 0.0055\alpha_N\alpha_M - 0.00005\alpha_M^2, \end{aligned} \tag{B.3}$$

and

$$\alpha_M = \frac{k^2}{\epsilon^2}M^2, \alpha_N = \frac{k^2}{\epsilon^2}N^2. \tag{B.4}$$

The c_μ and c'_μ of *Schumann and Gerz* (1995) are given by

$$c_\mu = c_\mu^0, \tag{B.5}$$

$$c'_\mu = \frac{c_\mu^0}{Pr_t}, \tag{B.6}$$

where $c_\mu^0 = 0.5477$, and the empirical relation for the turbulent Prandtl number is

$$Pr_t = Pr_t^0 exp\left(-\frac{R_i}{Pr_t^0 R_i^\infty}\right) - \frac{R_i}{R_i^\infty}, \tag{B.7}$$

where $Pr_t^0 = 0.74$ and $R_i^\infty = 0.25$.

APPENDIX C

RELAXATION TIME

Relaxation is introduced in the transport equation of momentum, e.g. the x-direction

$$\frac{D\overline{u}}{Dt} = \Gamma_{\overline{u}} - g\frac{\partial \zeta}{\partial x} + \int_z^{\zeta} \frac{\partial B}{\partial x} dz' - \frac{1}{\tau_R^{\overline{u}}}(\overline{u} - \overline{u}_{obs}), \tag{C.1}$$

the transport equation of potential temperature

$$\frac{D\overline{\theta}}{Dt} = \Gamma_{\overline{\theta}} - \frac{1}{\tau_R^{\overline{\theta}}}(\overline{\theta} - \overline{\theta}_{obs}) + \frac{1}{c_p \rho_0}\frac{\partial I}{\partial z}, \tag{C.2}$$

and the transport equation of salinity

$$\frac{D\overline{S}}{Dt} = \Gamma_{\overline{S}} - \frac{1}{\tau_R^{\overline{S}}}(\overline{S} - \overline{S}_{obs}), \tag{C.3}$$

where $\Gamma_{\overline{u}}$, $\Gamma_{\overline{\theta}}$, and $\Gamma_{\overline{S}}$ are sums of turbulent and viscous transport terms, ζ is the free surface elevation, and $\tau_R^{\overline{u}}$, $\tau_R^{\overline{\theta}}$, and $\tau_R^{\overline{S}}$ are relaxation times (*Burchard*, 2002). Figure C.1 depicts mean values of simulated ϵ from the CH model in the BBL as a function of relaxation times to observations of u, v, θ, and S. Changes in relaxation times to θ and S observations were found to be less significant than those to u and v observations, which is mainly due to that density gradients ($N^2 = 5.64\times10^{-4}$ s^{-2} on average in the BBL) were less than velocity gradients ($M^2 = 8.50\times10^{-3}$ s^{-2} on average in the BBL). We note that since S was not measured in the BBL, the GOTM used salinity values at the lower end of the observed profiles and extrapolated these as constant values to the bottom. The assumption of homogeneous S is believed to be appropriate after comparing temperature profiles in the BBL to those at site D

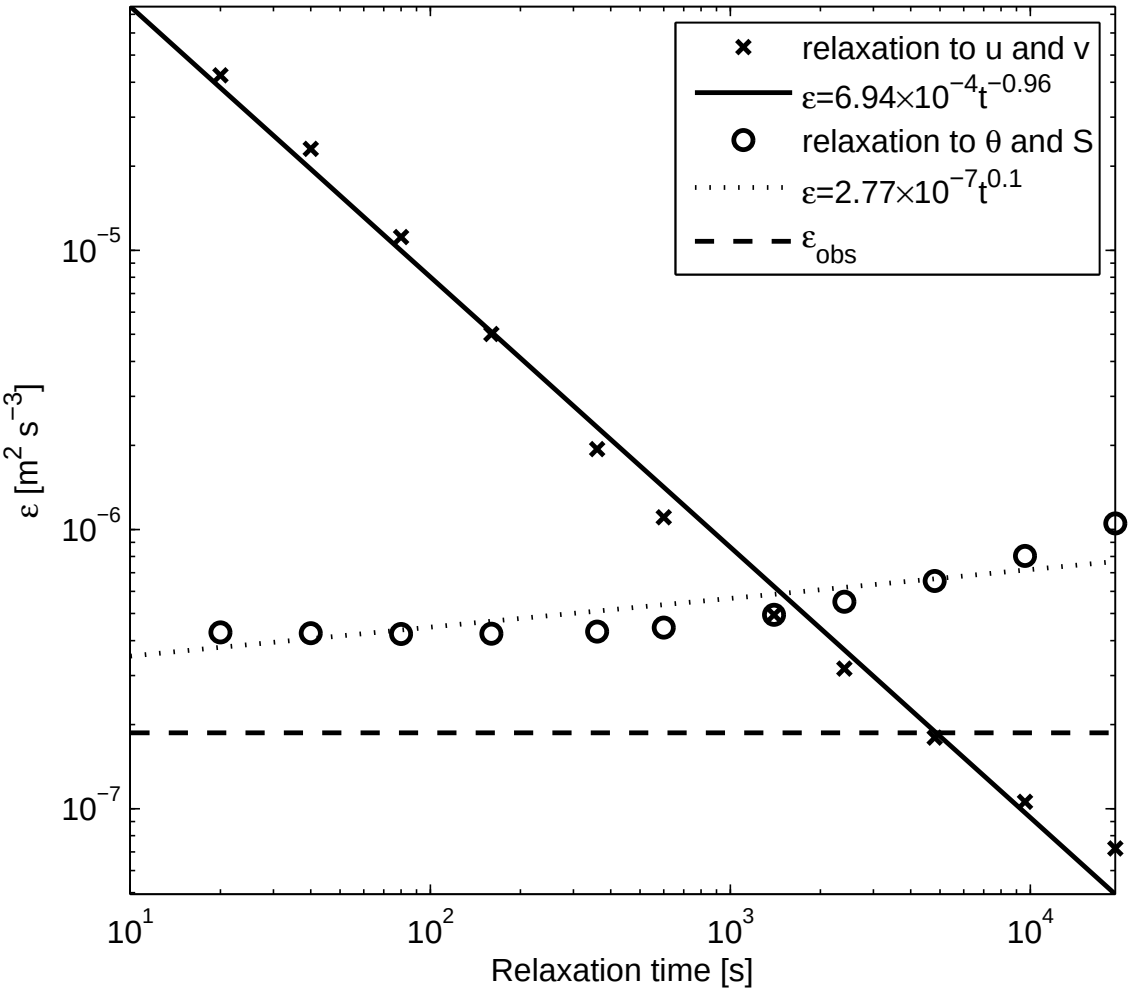

Figure C.1: Mean values of ϵ for the CH model in the BBL as a function of relaxation time in the range from 10 s to 320 minutes. Exponential fits were calculated for velocities, and θ and S, respectively. The mean value of observed ϵ is represented by the dashed line.

with similar depth (Figure 2.1). For the relaxation times tested, i.e., 10 s to 320 minutes, the relaxation to θ and S changed ϵ by less than an order of magnitude, while measured u and v in the BBL had a much more pronounced effect on turbulence quantities, thus modeled ϵ values spanned more than three orders of magnitude with the relaxation to u and v in Figure C.1. Relaxation times of 4000 s to observed u and v, and 360 s to observed θ and S resulted in CH simulated ϵ values similar to those observed.